

BEHAVIOR OF REINFORCED CONCRETE SLABS SUBJECTED TO IMPACT LOADS

**A Thesis Submitted to
the Graduate School of Engineering and Sciences of
İzmir Institute of Technology
in Partial Fulfillment of the Requirements for the Degree of**

MASTER OF SCIENCE

in Civil Engineering

**by
Baturay BATARLAR**

July 2013

İZMİR

We approve the thesis of **Baturay BATARLAR**

Examining Committee Members:

Assist. Prof. Dr. Selçuk SAATCI

Department of Civil Engineering, İzmir Institute of Technology

Assist. Prof. Dr. Cemalettin DÖNMEZ

Department of Civil Engineering, İzmir Institute of Technology

Assoc. Prof. Dr. Alper TAŞDEMİRCİ

Department of Mechanical Engineering, İzmir Institute of Technology

10 July 2013

Assist. Prof. Dr. Selçuk SAATCI

Supervisor, Department of Civil Engineering
İzmir Institute of Technology

Prof. Dr. Gökmen TAYFUR

Head of the Department of Civil Engineering

Prof. Dr. R. Tuğrul SENGER

Dean of the Graduate School of
Engineering and Sciences

ACKNOWLEDGEMENTS

This study is the initiative work of research series which is financially supported from the European Community's Seventh Framework Programme [FP7/2007-2013] under grant agreement n^o 211092 and accomplished in Izmir Institute of Technology Structural Mechanics Laboratory. During accomplishment of the study, many people took part in this struggle that deserve more than thanks.

First, I am grateful to my supervisor Selçuk Saatcı, who gave me a chance to involve in this valuable project and always kept his patience and constant supports to me. Without his guidance and experiences, it would be impossible challenge.

Despite manufacturing the specimens and carrying out the tests were the uphill battle, they became manageable owing to my colleagues and laboratory technician.

Lastly, special thanks go to my parents for standing behind me with their full supports, and my beloved sister and brother in-law for inspiring me to go on academic studies and never letting me down.

ABSTRACT

BEHAVIOR OF REINFORCED CONCRETE SLABS SUBJECTED TO IMPACT LOADS

This study presents the findings of an experimental program designed for investigating the behavior of RC slabs under low-velocity impact loads. Six RC slabs with dimensions 2015x2015x150 mm were tested at the Structural Laboratory of the Izmir Institute of Technology. To facilitate a comparison between the static and impact behavior of identical specimens, the slabs were cast in three identical pairs, such that one of the specimens was tested under impact loads whereas its identical twin was tested under static loads. To test the slabs under simply supported conditions, an innovative impact test setup was designed and manufactured, supporting the specimens at 20 locations along the perimeter and holding the specimens in place during the impact induced rebound. This setup was also used for the testing of the specimens under monotonically increasing static loads at the midpoint. Impact loads were induced on the specimens by a free falling drop-weight, impacting the specimens at the midpoint. The specimens were intensely instrumented with 20 load cells at each support location, 24 displacement transducers, 6 accelerometers and 12 strain gauges fixed to the reinforcing bars. Dynamic data was captured with the help of a high speed data acquisition system, capturing and recording the data at a rate of 250 kHz per channel. The results obtained from these tests revealed that the impact behavior of slabs differs significantly compared to their static behavior. Displacement profiles and force distributions are highly affected due to the high inertia forces during the impact.

ÖZET

DARBE YÜKLERİNE MARUZ KALAN BETONARME DÖŞEMELERİN DAVRANIŞI

Bu çalışma betonarme elemanların düşük hızlı darbeye maruz kaldıkları durumlarda davranışının incelenmesi için dizayn edilen deneysel program bulgularını ortaya koymaktadır. Altı adet 2015x2015x150 mm ebatlarında betonarme döşemeler İzmir Yüksek Teknoloji Enstitüsü Yapı Mekaniği Laboratuvarlarında test edilmiştir. Statik ve darbe davranışının karşılaştırılmasını ortaya koyabilmek için döşemeler üç tip şekilde imal edilmiş olup her tip döşemeden biri statik diğeri darbe yükü altında test edilmiştir. Deneyleri gerçekleştirmek için, ideal basit mesnet koşullarını döşemelerin çevresi boyunca 20 noktada sağlayan ve darbe anında sıçramasını engelleyen bir deney düzeneği tasarlanıp imal edilmiştir. Bu düzenek orta noktasından monotonik şekilde yüklenen statik deneyler için de kullanılmıştır. Darbe deneyleri belirli kütlelerin döşemelerin orta noktalarına düşürülmesiyle gerçekleştirilmiştir. Numunelerden her mesnet noktasında 20 adet yük hücresi, statik deneyler için 16 adet, darbe deneyleri için 24 adet deplasman ölçer, 6 adet ivme ölçer ve donatıların üzerine yerleştirilen 12 adet gerinim pulu sayesinde ölçüm alınmıştır. Dinamik veriler, 250000 örnek/saniye/kanal hızla yüksek hızlı veri toplama sistemi sayesinde alınıp kaydedilmiştir. Bu testlerden alınan sonuçlar döşemelerin darbe davranışının statik davranışa göre önemli farklılıklar gösterdiğini ortaya koymuştur. Darbe sırasında oluşan yüksek atalet kuvvetleri, şekil değiştirmeler ve kuvvet dağılımlarını büyük ölçüde etkilemiştir.

TABLE OF CONTENTS

LIST OF FIGURES	viii
LIST OF TABLES.....	xii
CHAPTER 1. INTRODUCTION	1
CHAPTER 2. LITERATURE REVIEW	3
CHAPTER 3. EXPERIMENTAL PROGRAM.....	21
3.1. Test Specimens	21
3.2. Test Setup	24
3.3. Material Properties.....	27
3.4. Instrumentation	28
3.4.1. Resistive Linear Position Transducers (RLPT's).....	28
3.4.2. Strain Gauges	31
3.4.3. Load Cells	34
3.4.4. Accelerometers.....	34
3.4.5. Data Acquisition System.....	35
3.4.6. Drop Weights	36
3.4.7. High-Speed Camera	37
3.5. Loading Protocol	37
3.5.1. Static Tests	38
3.5.2. Impact Tests	40
3.5.3. Punching Cone Observations	43
CHAPTER 4. DISCUSSION OF TEST RESULTS.....	45
4.1. Static Test Observations	45
4.1.1. BB100a (Test Date: February 13, 2012)	45
4.1.2. BB150a (Test Date: March 01, 2012)	46
4.1.3. BB200a (Test Date: March 14, 2012)	47
4.2. Discussion of Static Tests.....	48

4.2.1. Flexural Strength	49
4.2.2. Punching Strength	52
4.3. Impact Tests Observations.....	58
4.3.1. BB100b Tests	58
4.3.2. BB150b Test.....	59
4.3.3. BB200b Tests	60
4.4. Discussion of Impact Tests	61
4.4.1. Digital Data Analysis	62
4.4.2. Displacements and Deformations.....	66
4.4.3. Reactions and Loads.....	73
4.4.4. Dynamic Equilibrium.....	82
 CHAPTER 5. CONCLUSIONS	 87
 REFERENCES	 88
 APPENDIX A.....	 91

LIST OF FIGURES

<u>Figure</u>	<u>Page</u>
Figure 2.1. Missile impact phenomena	4
Figure 2.2. Sensor locations and support conditions	5
Figure 2.3. Crack patterns along the top surfaces	6
Figure 2.4. Cross section of the specimens W1, W2 and W3, respectively	7
Figure 2.5. Total reaction forces (kN) vs. time (ms) at supports for three tests	8
Figure 2.6. Specimens after falling weight, actuator and blasting tests, respectively	8
Figure 2.7. Reinforcement layout of slabs (All dimensions in mm).....	9
Figure 2.8. Deflection of slab center by integrating accelerations twice for withsand (S1) and gravel (G1) cushion	9
Figure 2.9. Cross-section of reinforced concrete slab	10
Figure 2.10. Crack patterns after tests	10
Figure 2.11. Details of the slabs: a) 0.76 m square slabs; b) 2.3 m square slabs	11
Figure 2.12. Slab faces after impact	12
Figure 2.13. Slabs with standard steel reinforcement (B3, left) and additional stirrup reinforcement (B4, right)	14
Figure 2.14. Standard concrete slab with additional steel fabric (B7, left) and with carbon fabric (B9, right)	14
Figure 2.15. Measurements from slab D1	15
Figure 2.16. Dimensions, reinforcement layout and support conditions for each slab...	16
Figure 2.17. Time histories of impact force, reaction force and deflection.....	17
Figure 2.18. Crack patterns in each slab	17
Figure 2.19. Illustration of the tested slab showing the impacted areas and position of stoneware clay sensors	18
Figure 2.20. a) Localization of the impact points and stoneware clay devices on the slab.....	19
Figure 2.21. Local damage cracks on the slab surface in area 1	19
Figure 2.22. Details of setup	20
Figure 2.23. Time histories of impact and mid-point displacement	20
Figure 3.1. Test specimens	22

Figure 3.2. Reinforcing meshes for specimens.....	22
Figure 3.3. Naming conventions for the slabs	23
Figure 3.4 Manufacturing specimens.....	23
Figure 3.5. Test setup.....	25
Figure 3.6. Detail of a hinge on the setup.....	26
Figure 3.7. Hydraulic jack with the load cell.....	26
Figure 3.8. Test setup before impact test	27
Figure 3.9. Resistive Linear Position Transducer.....	28
Figure 3.10. Locations of RLPTs.....	29
Figure 3.11. (a) Connection between potentiometer and rod; (b) connection between specimen and hinge	30
Figure 3.12. A view of RLPTs for impact tests	31
Figure 3.13. Strain gauge on bars before covered	32
Figure 3.14. Strain gauge locations for BB100a&b.....	32
Figure 3.15. Strain gauge locations for BB150a&b.....	33
Figure 3.16. Strain gauge locations for BB200a&b.....	33
Figure 3.17. 5000 kg (on the left) and 10000 kg capacity (on the right) load cells on the hinge	34
Figure 3.18. Locations of accelerometers	35
Figure 3.19. Accelerometer and protection block.....	35
Figure 3.20. Data acquisition system.....	36
Figure 3.21. Details of drop weights.....	36
Figure 3.22. Drop weights (210 kg and 320 kg, respectively).....	37
Figure 3.23. View of the BB100a tension surface after test	38
Figure 3.24. View of the BB150a tension surface after test	39
Figure 3.25. View of the BB200a tension surface after test	39
Figure 3.26. Final state of the specimen BB100b after second impact	41
Figure 3.27. Final state of the specimen BB150b after impact test	42
Figure 3.28. Final state of the specimen BB200b after impact test	43
Figure 3.29. Punching cone diameter for BB100b	43
Figure 3.30. Typical punching cone illustration	44
Figure 4.1. Crack profiles of tension surface for BB100a specimen	46
Figure 4.2. Crack profiles of tension surface for BB150a specimen	47

Figure 4.3. Crack profiles of tension surface for BB200a specimen	48
Figure 4.4. Strip illustration of slab (cc is clear cover; d is effective depth)	48
Figure 4.5. Yield line mechanism (Case A).....	50
Figure 4.6. Yield line mechanism (Case B).....	50
Figure 4.7. Yield line mechanism (Case C).....	51
Figure 4.8. Moment- curvature diagrams obtained from Response2000	52
Figure 4.9. Control perimeter according to ACI 318-11 Clause 11.11.1.2	53
Figure 4.10. Control perimeter according to EC2 2004	55
Figure 4.11. Static load-displacement behavior of test specimens	58
Figure 4.12. Impact crack profiles of bottom surface for BB100b.....	60
Figure 4.13. Impact crack profile of bottom surface for BB150b	61
Figure 4.14. Impact crack profile of bottom surface for BB200b	61
Figure 4.15. Midpoint displacements for BB200b-1 (P16)	63
Figure 4.16. Midpoint displacement response for BB200b-1 (P16).....	63
Figure 4.17. Derived velocity response for BB200b-1 at P16 location.....	64
Figure 4.18. Derived acceleration response for BB200b-1 at P16 location	64
Figure 4.19. Drop-weight (210 kg) accelerations for BB200b.....	65
Figure 4.20. Acceleration and displacement response for BB150b at the P8 location..	65
Figure 4.21. Midpoint displacement-time histories (P16)	66
Figure 4.22. RLPT locations for displaced shapes	67
Figure 4.23. Maximum, minimum and residual deformations for BB100b-1, BB150b and BB200b-1, respectively	69
Figure 4.24. Displacement profiles of BB150a and BB150b for the same midpoint displacements	70
Figure 4.25. 3-D plots of displacement profiles for quadrants of BB150b	71
Figure 4.26. Crack profile and strain gauge locations for BB150b specimen	72
Figure 4.27. Strain gauge 3 measurements for BB150b.....	73
Figure 4.28. Load cell measurement profiles of BB150a and BB150b-1 for the same midpoint displacements.....	75
Figure 4.29. Load cell measurement profiles of impact test at different time steps.....	76
Figure 4.30. Load cell measurement profiles of static test for different midpoint displacements	77
Figure 4.31. Reaction-time histories along the one edge for impact tests	78

Figure 4.32. Total reaction force- time histories for impact tests.....	78
Figure 4.33. Total reaction force- time histories for specimen BB100b	79
Figure 4.34. Total reaction forces- time histories for specimen BB200b.....	79
Figure 4.35. Drop-weight accelerometers for BB100b-1, BB150b and BB200b-1, respectively	80
Figure 4.36. Impact force- time histories for BB100b-1 and BB200b-1	81
Figure 4.37. Impulse- time histories for BB100b-1 and BB200b-1	81
Figure 4.38. 3-D plots of derived acceleration profiles for quadrants of BB150b	84
Figure 4.39. Dynamic equilibrium for BB100b-1	85
Figure 4.40. Dynamic equilibrium for BB200b-1	85
Figure 4.41. Maximum moments and shears for impact and static cases.....	86

LIST OF TABLES

<u>Table</u>	<u>Page</u>
Table 2.1. Experimental configuration	13
Table 3.1. Test specimens	23
Table 3.2. Cylindrical test results	28
Table 3.3. Loading protocol for impact tests	40
Table 3.4. Punching cone angles for all specimens	44
Table 4.1. Comparison of results for static tests	58
Table 4.2. Peak support reactions	79

CHAPTER 1

INTRODUCTION

Throughout the history, civil engineering applications have been improving in accordance with demands and desires of the humanity. With the advent of reinforced concrete (RC) technology, reinforced concrete structures have become majority of existing structures. In the course of designing these structures, different types of load combinations can be taken into consideration such as earthquake, blast and impact loads in addition to gravitational loads. In this manner, impact loads have been an objective for many designers and researchers. Due to the various reasons, structures may be subjected to impact loads such as vehicle collisions, rock falls, accidental events in industry, military actions and terrorist attacks. With the aim of avoiding disasters, experimental and numerical studies on RC structures have important role in order to understand behavior of RC structures under impact loads. Military needs have initiated investigations of impact loading which have been mostly interested in designing and analyzing structures against high velocity impacts such as impact of ballistic missile. Local response of RC members has been a focus of attention which involved penetration and perforation of a missile through the RC structure with high velocity in range of 10-100 m/s and smaller diameter with respect to target thickness. However, more frequently encountered problems compared to military applications and terrorist attacks are the events which are encountered in civil applications such as rock falls, ice and vehicle collision to bridge piers. In these events, target responds the impact globally as a structure and suffers extensive damage beyond the point of impact.

This study investigates the behavior of RC slabs tested under varied impact loads and compares the results with behavior of identical specimens tested under static loads. To facilitate static and impact tests, an innovative test setup was designed and manufactured, supporting the specimens at 20 locations along the perimeter. Well-instrumented test data were collected from these tests with intent to comprehend the behavior of RC slabs under impact loads which can be utilized in further studies and can be a reference point in order to develop impact analysis and design methods.

The presented work is comprised of five chapters. Following this chapter, previous efforts in literature were researched and reviewed in Chapter 2 with the limitation of global behavior of RC slabs under impact loading conditions.

Chapter 3 explains the details of test setup and tested specimens including the manufacturing processes, instrumentation and data measurement devices used.

The results from the experiments were described and discussed in Chapter 4.

Chapter 5 is the final part of the represented work which contains conclusions of this study.

CHAPTER 2

LITERATURE REVIEW

Analysis and design of the reinforced concrete (RC) structures subjected to impact loads have long been an area of interests for the researchers. Initial studies on this subject were aimed towards predicting the depth of penetration of missile, exit velocity, and structural resistance. Studies by Robins-Euler in 1742, Poncelet in 1830, and Resel in 1895 are the earliest examples of such research (Corbett et al. 1996). With the development of reinforced concrete technology and increasing industrial demands, such approaches proved to be insufficient for the purpose of designing structures subjected to impact loads.

Majority of impact studies available in the literature are on the behavior of reinforced concrete structures subjected to ballistic weapons. Specifically after the Second World War, research in this area has escalated. At the same time, demands from the nuclear energy industry for the impact resistant design of nuclear reactors have also increased. These structures needed to be designed against impact loads such as the ones due to vehicle and equipment accidents, plane crashes, and missile attacks, since failure due to such incidents could result in catastrophes. In more recent decades, focus on the impact research has widened to include impact resistant design of rock sheds for highways and railways, protective barriers, bridge piers, industrial facilities against accidents, and sea structures against ice and ship collisions.

Impacts of missiles on structures are commonly classified into two categories: hard impacts and soft impacts. In hard impact incidents, missiles do not have substantial deformation compared to the impacted structure. On the other hand, in soft impact incidents, missiles deform substantially as well.

Structures subjected to impact loads can also be grouped according to their response: structures that suffer only local damage around the point of impact, structures that respond the impact through global member deformations, and combination of both this two responses. Local damages are categorized in three levels: a) penetration of the missile and spalling of the pieces from the penetrated face; b) significant scabbing from

both the front and back faces of the structure; and c) perforation of the element. Figure 2.1 summarizes the impact behavior of structures.

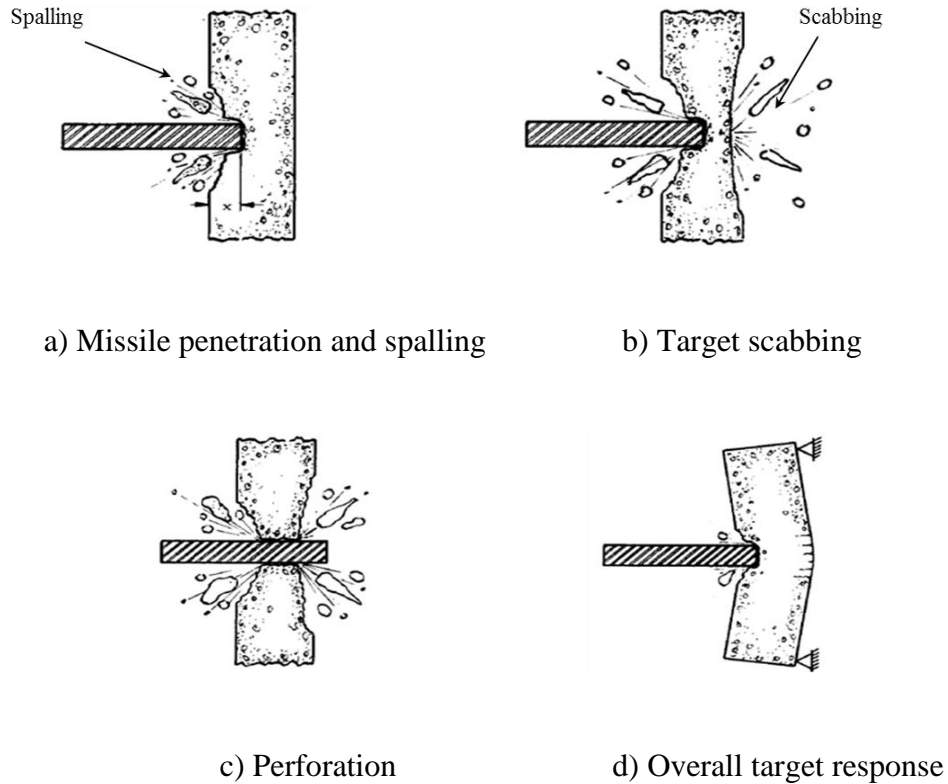


Figure 2.1. Missile impact phenomena
(Source: Kennedy, 1976)

The study presented herein focuses on the impacts that result in the response of structures through global member deformations. Therefore, the literature review provided in this section will be limited to the studies in this area.

An example to the experimental studies on the impact behavior of reinforced concrete slabs was carried out by Zinnedin et al. (2007). The tests consisted of three types of slabs with 90x1524x3353 mm in dimension. First type was reinforced with two 152x152 mm meshes of welded steel wires with a diameter of 5 mm under 25 mm clear cover; second, with one 152x152 mm mesh of No. 3 steel bars with a diameter of 9.5 mm located in the middle of the slab thickness, and third, with two 152x152 mm meshes of No.3 steel bars with a diameter of 9.5 mm located under 25 mm cover. Impact mass was approximately 2608 kg and it was dropped from 152, 305 and 610 mm

heights. The test setup restrained slabs with two rows of bolts on all sides. The support conditions were described as somewhere between simply supported and fixed. A load cell on the impact hammer was used to record load pulses, and accelerometers were mounted on the back surface of the slabs at different locations. For measuring the deformations of the slabs, two deflection gages were used at mid-point (gage 1) and quarter (gage 2) points of the major axes of the slab (Figure 2.2).



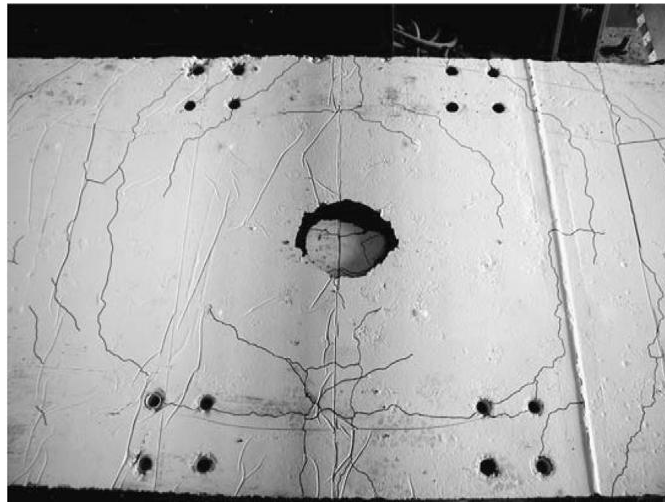
Figure 2.2. Sensor locations and support conditions
(Source: Zinnedin, 2007)

Nine specimens, three specimens for each three types, were impacted from varying heights of 305, 152 and 610 mm. During the tests, impact load-time histories, deformations of the slabs at two locations, the accelerations of the slabs, accelerations of the impact mass and strains of the reinforcements were collected.

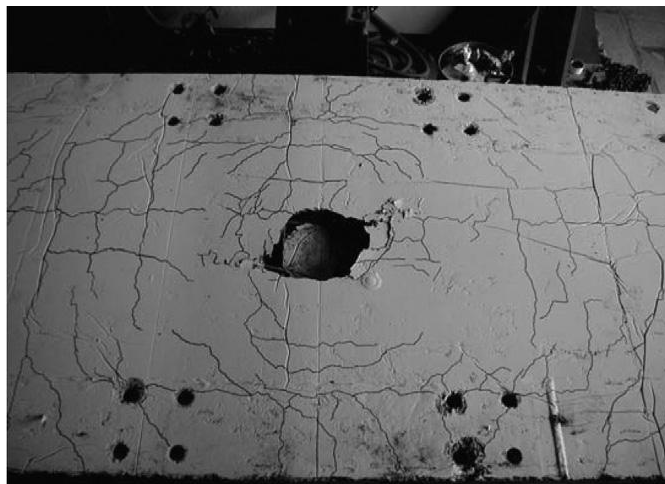
According to interpreted data and crack profiles of the slabs, failure modes of the slabs depend on the reinforcement details and drop height of the impact load. For the same reinforcement details of slabs, increase in drop height of the impact mass caused tendency to local damage. Flexural behavior can be barely seen at high rates of loading. Hence, when the drop height was increased, the local response dominated the behavior of the slab and punching shear occurred. Thus, shear cracks were more visible and wide for the same amount of reinforcement. However, diameters of the punching holes were inversely related to the drop height (Figure 2.3)

Spalling was affected by reinforcement type and amount. More concrete was severed from the back face of the slabs with the least amount of reinforcement. In the

tests, maximum load measured on the slabs did not vary between the specimens, since reinforcing steel failure determined the member failure.



a) From 305 mm drop on slab with mesh of No.3 rebar



b) From 610 mm drop on slab with mesh of No.3 rebar

Figure 2.3. Crack patterns along the top surfaces
(Source: Zinnedin, 2007)

The study of four test series – small scale, medium scale, large scale and punching tests- is another example to the studies on the impact behavior of reinforced concrete slabs. The focus of this study was on the structural behavior of rock fall galleries under impact loads. Small scale tests were conducted by Buzzini et al. 2006, whereas rests of the series were carried out by Schellenberg (2009).

In small-scale tests, three 900x900 mm square slabs are tested. As seen in Figure 2.4, thickness of the slabs was 100 mm, except the third slab for which it was reduced to 52 mm.

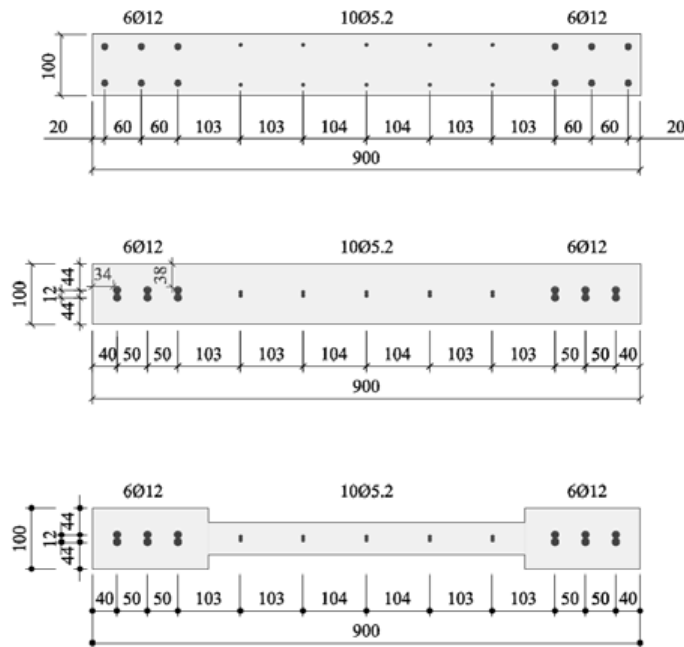


Figure 2.4. Cross section of the specimens W1, W2 and W3, respectively
(Source: Buzzini et al., 2006)

In the first test, a 825 kg concrete boulder with a dimension of 800 mm in diameter was dropped from a 2 m height on the specimen (W1). Simply supported conditions were provided at the four corners of slab. In addition, a sand cushion with a thickness of 190 mm covered the slab in order to dissipate energy. For the second test, a servo-controlled actuator with a maximum load capacity of 100 kN applied a sudden 20 mm displacement on the specimen (W3). In the third test, impact loading was provided by blasting called as water hammer. Support forces, strains, accelerations and displacements were measured during the tests (Figure 2.5).

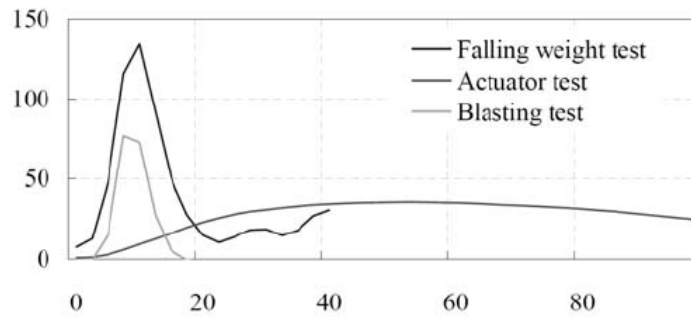


Figure 2.5. Total reaction forces (kN) vs. time (ms) at supports for three tests (Source: Buzzini et al., 2006)

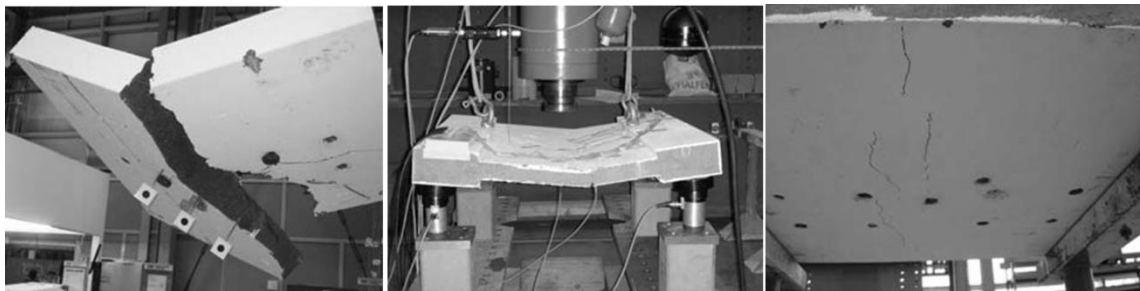


Figure 2.6. Specimens after falling weight, actuator and blasting tests, respectively (Source: Buzzini et al., 2006)

Falling weight tests proceeded in medium-scale tests. Three RC slabs with 1500x1500x230 mm dimensions were tested under simply supported conditions (Figure 2.7). Three different types of cushion were used in these tests. The falling weight was 825 kg and it was dropped from 2 m similar to the small-scale falling weight tests. Impact velocities, impact energies, penetration depths, maximum reaction forces and accelerations, and dissipated energies were calculated for the different types of cushions including sand, cellular glass and gravel (Figure 2.8).

For large-scale tests, six RC slabs covered by cushions were tested until they failed. Three types of slabs, named from one to six, were used. Slabs 1 and 2 with a thickness of 250 mm had no shear reinforcement. Slabs 3 and 4 also had no shear reinforcement but their thicknesses were increased to 350 mm. Last two slabs had shear reinforcement and their thicknesses were 350 mm as well. For all six slabs, dimensions were 3500x4500 mm.

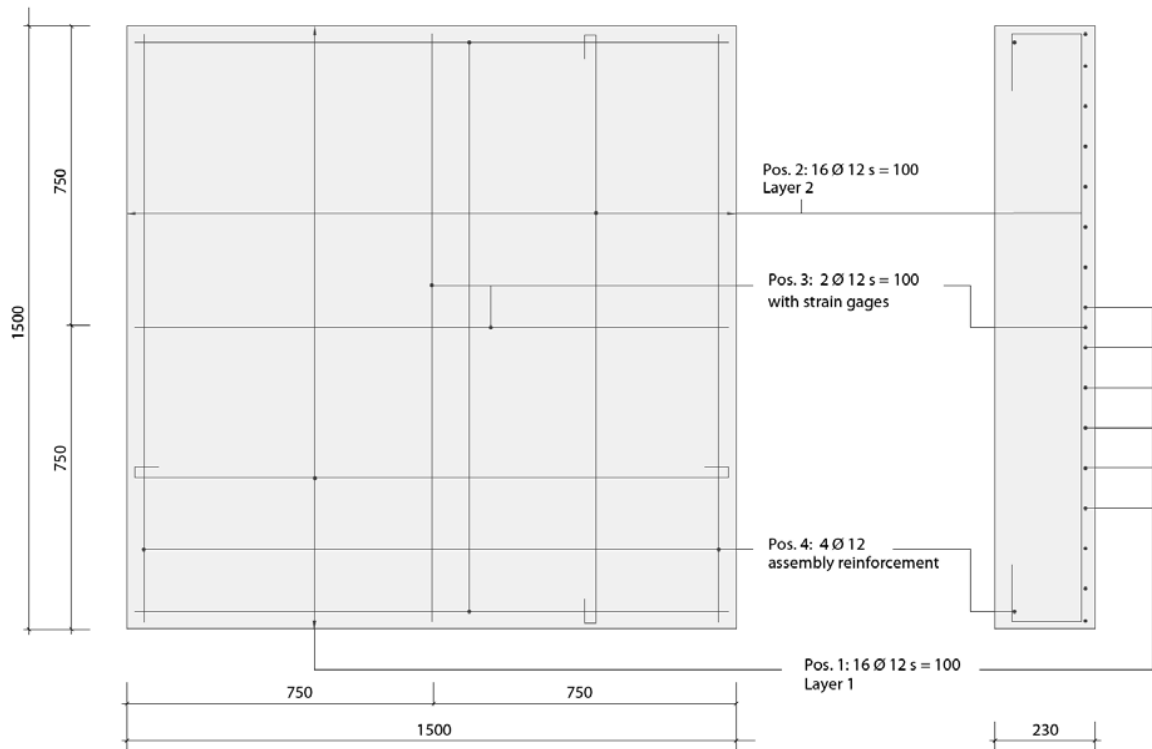


Figure 2.7. Reinforcement layout of slabs (All dimensions in mm)
(Source: Schellenberg, 2009)

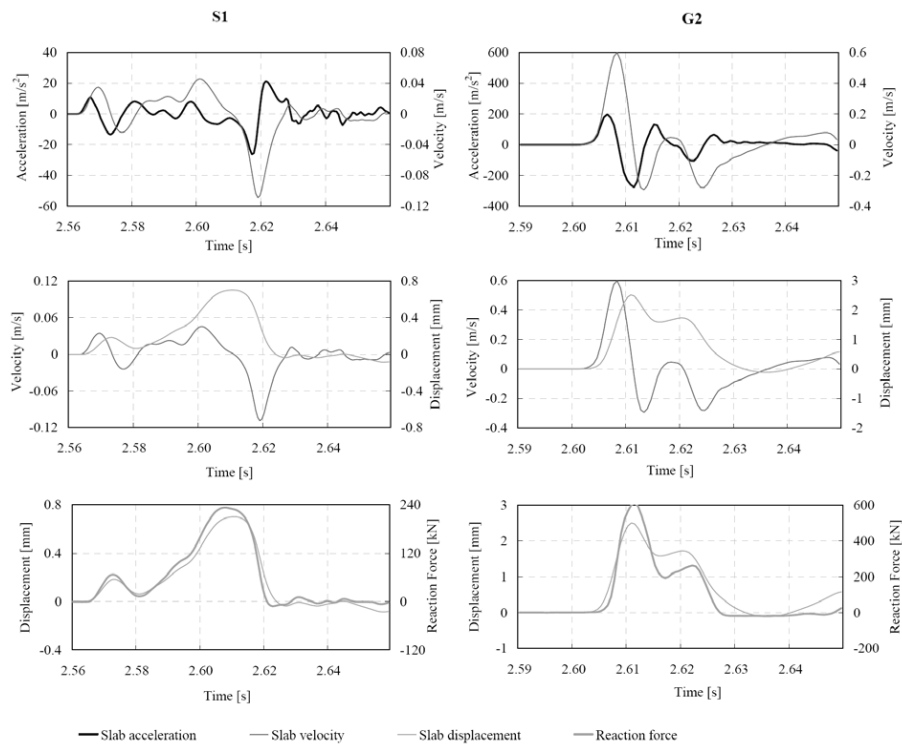


Figure 2.8. Deflection of slab center by integrating accelerations twice for with sand (S1) and gravel (G1) cushion (Source: Schellenberg, 2009)

Drop weight tests of the study were performed at Muroran Institute of Technology in Japan. Cushion material and falling weight remained same during the tests. A weight of 300 kg dropped at fixed velocities and different loading diameters. The impact velocities were varied between 6 and 10 m/s. Diameter of falling weight was 60 mm for the first slab and it was 150 mm for the rest of five. Slabs were 2000x2000x180 mm in dimension and 100 mm sand cushion were placed on top (Figure 2.9).

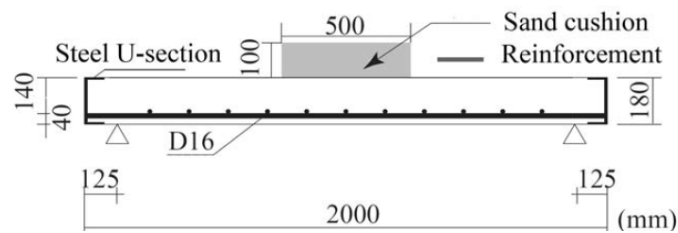


Figure 2.9. Cross-section of reinforced concrete slab
(Source: Schellenberg, 2009)

Punching failure occurred for all slabs. Less bending cracks and lower punching resistance were observed for the falling weight with smaller diameter. Figure 2.10 shows crack patterns of the slabs tested with 60 mm diameter of loading area (S6) and 150 mm diameter of loading area (S15).

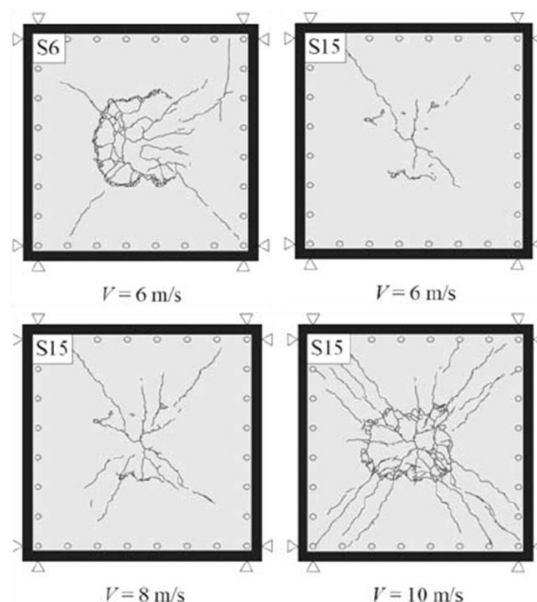


Figure 2.10. Crack patterns after tests
(Source: Kishi et al., 2008)

A series of experimental studies involving reinforced concrete members tested under drop weight impacts were carried out by Chen and May (2009). The aim of their study was to carry out the experiments and to validate their method of numerical modeling. The study involved 18 beams and six slabs. Two types of slabs, four of them with dimensions 760x760x76 mm and two of them with dimensions 2300x2300x150 mm, were tested (Figure 2.11). The slabs were numbered from 1 to 4 for 0.76 m square slabs and 5 and 6 for 2.3 m square slabs. All four 0.76 m square slabs were subjected to impact loads with 98.7 kg striker mass whereas for the two 2.3 m square slabs, 196.7 kg and 382 kg of masses were used. Impact velocities were 6.5 m/s for slabs 1 to 3. Slabs 4, 5 and 6 were subjected to impacts at 8, 8.7 and 8.3 m/s, respectively. Steel reinforcement ratio of the slabs were 0.6% for slabs 1, 2 and 3; 1.1% for slab 4; 0.5% for slab 5 and 6. Concrete cube strength was 60 MPa for the smaller slabs, whereas for slabs 5 and 6, it was 47.3 and 55.7 MPa, respectively.

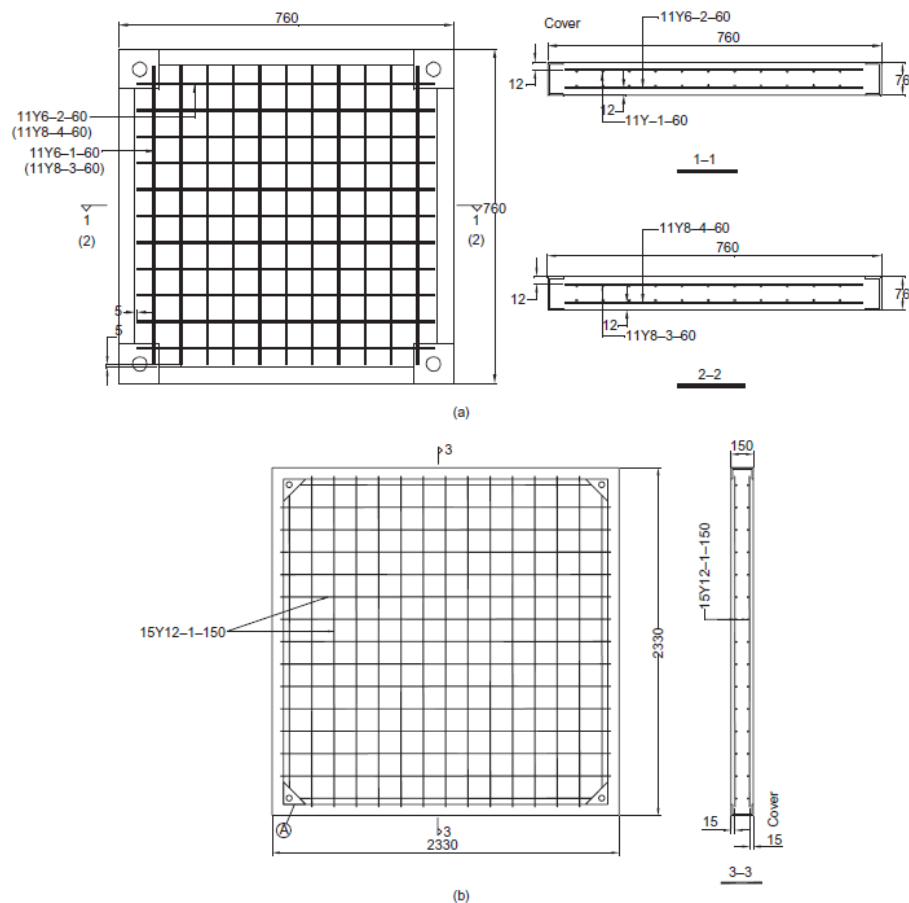


Figure 2.11. Details of the slabs: a) 0.76 m square slabs; b) 2.3 m square slabs (Source: Chen and May 2009)

The supports were described as restrained in horizontal and vertical directions at four corners. Two types of drop weights were used in the tests. One of them was steel with 90 mm diameter and had a tip with a hemispherical profile. Another type had a flat surface with a 100 mm diameter.

In the tests, all slabs were subjected to drop weight with hemispherical tip except one of the 0.76 m square slab, which was tested using the drop weight with a flat surface. Using different types of drop weights revealed that hemispherical tip of the striker creates more circular scabbing zone on the bottom face of the slab compared to flat one. Figure 2.12 shows the damages on both faces of six slabs.

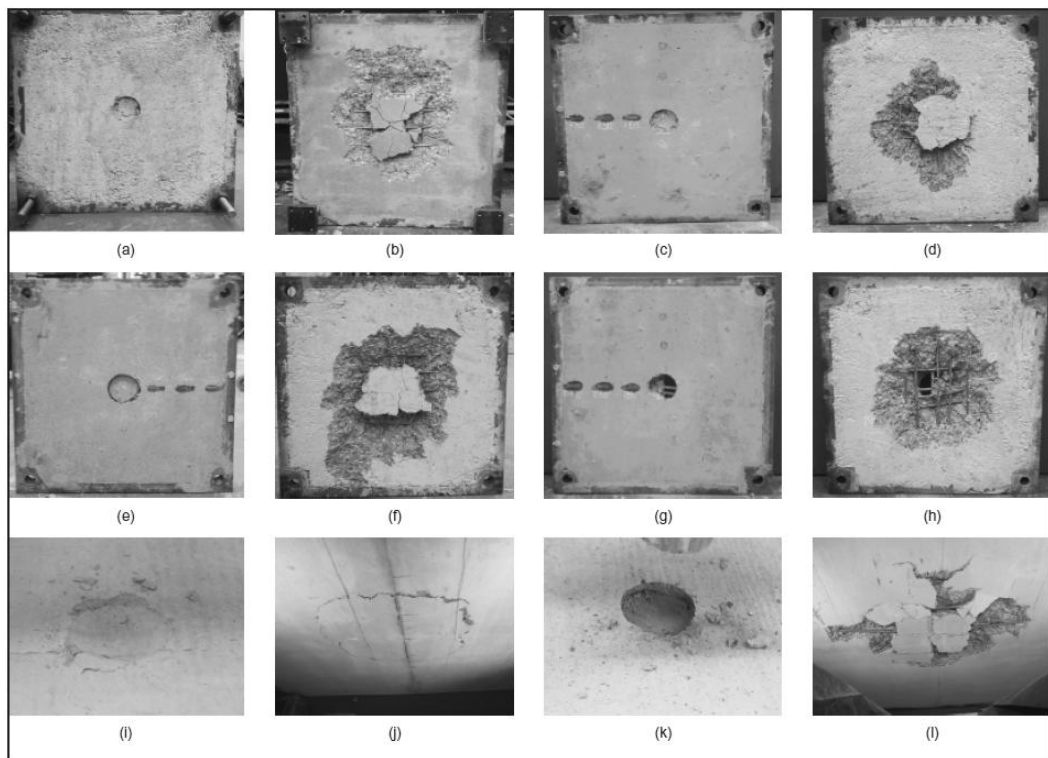


Figure 2.12. Slab faces after impact: a) top face of slab 1; b)bottom face of slab 1; c) top face of slab 2; d)bottom face of slab 2; e) top face of slab 3; f) bottom face of slab 3; g) top face of slab 4; h) bottom face of slab 4; i) top face of slab 5; j) bottom face of slab 5; k) top face of slab 6; l) bottom face of slab6 (Source: Chen and May, 2009)

As mentioned before, this study included the investigation of the low-velocity impact behavior of RC members to validate numerical modeling. For that reason, empirical formulae predicting scabbing diameters and slab thickness to prevent

perforation were compared with tests results. Transient impact load of the slabs and transient reinforcement strain were also presented.

Hummeltenberg et al. (2011) also carried out several impact tests on concrete slabs. In their study, the behavior of RC slabs with different types of concrete including standard concrete, high performance concrete (HPC) and ultra-high performance concrete (UHPC) were investigated.

Study involves testing of 15 RC slabs with 1000x1000x150 mm dimensions. Slabs were grouped according to their type of concrete. All slabs had same reinforcement layout with steel mesh Q524 which consists of bars with 10 mm diameter, 150 mm spacing in both directions and 500 MPa yield stress. In addition to longitudinal reinforcement, two slabs were reinforced with C-shaped stirrups to improve shear resistance. Six slabs were also enhanced with additional fiber mesh reinforcement. The condition of the supports was described as simply supported at four corners of the slab and support forces were obtained by the load cells.

Table 2.1. Experimental configuration
(Source: Hummeltenberg et al. 2011)

Name	Concrete	Cube strength [N/mm ²]	Reinforcement mesh	stirrup	Fabric	Drop mass [kg]	Drop height [m]	Velocity [m/s]
B1	C20/25	34,7	Q524	--		290	6,0	10,8
B2	C20/25	34,7	Q524	--		183	7,5	12,1
B3	C20/25	34,7	Q524	--		183	9,0	13,3
B4	C20/25	34,7	Q524	∅6 mm		183	7,5	12,1
B5	C20/25	34,7	Q524	∅6 mm		183	7,5	12,1
B6	C20/25	34,7	Q524	--	steel fabric	183	7,5	12,1
B7	C20/25	34,7	Q524	--	steel fabric	183	7,5	12,1
B8	C20/25	34,7	Q524	--	carbon fabric	183	7,5	12,1
B9	C20/25	34,7	Q524	--	carbon fabric	183	7,5	12,1
C1	C70/85	76,7	Q524	--		183	3,0	7,7
C2	C70/85	76,7	Q524	--		183	5,5	10,4
C3	C70/85	76,7	Q524	--	steel fabric	183	5,5	10,4
C4	C70/85	76,7	Q524	--	steel fabric	183	7,5	12,1
D1	UHPC	185,2	Q524	--		183	5,5	10,4
D2	UHPC	184,1	Q524	--		183	3,5	7,7

For impact of the tests, cylindrical hardened steel with 10 cm diameter and 20 cm height was dropped at the center of slabs. As seen on Table 2.1, drop heights and velocities of masses varied whereas drop mass remained same except for the first test. Drop height changed from 3 to 9 m resulting velocities from 7.7 to 13.3 m/s.

After the tests, all slabs with standard concrete and standard steel reinforcement suffered from perforation including slabs with the shear reinforcement (Figure 2.13). Slabs with additional fabric reinforcement were also damaged, but they were not entirely perforated.



Figure 2.13. Slabs with standard steel reinforcement (B3, left) and additional stirrup reinforcement (B4, right) (Source: Hummeltenberg et al., 2011)

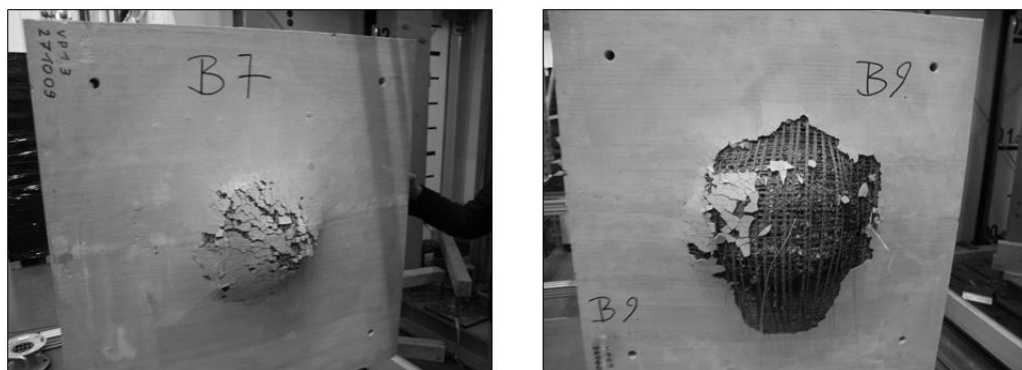


Figure 2.14. Standard concrete slab with additional steel fabric (B7, left) and with carbon fabric (B9, right) (Source: Hummeltenberg et al., 2011)

The difference in the behavior of the slabs mentioned above was also seen in the group of high performance concrete slabs with and without additional fabric reinforcement.

Figure 2.15 presents the measurements and global response of the slab D1. As clearly seen in the time-deflection history, bending started as the second part of the structural response. Reaction forces were also started to rise 4 ms after the first contact. At the instant of the impact, a tensile strain was observed on the upper face of the slab.

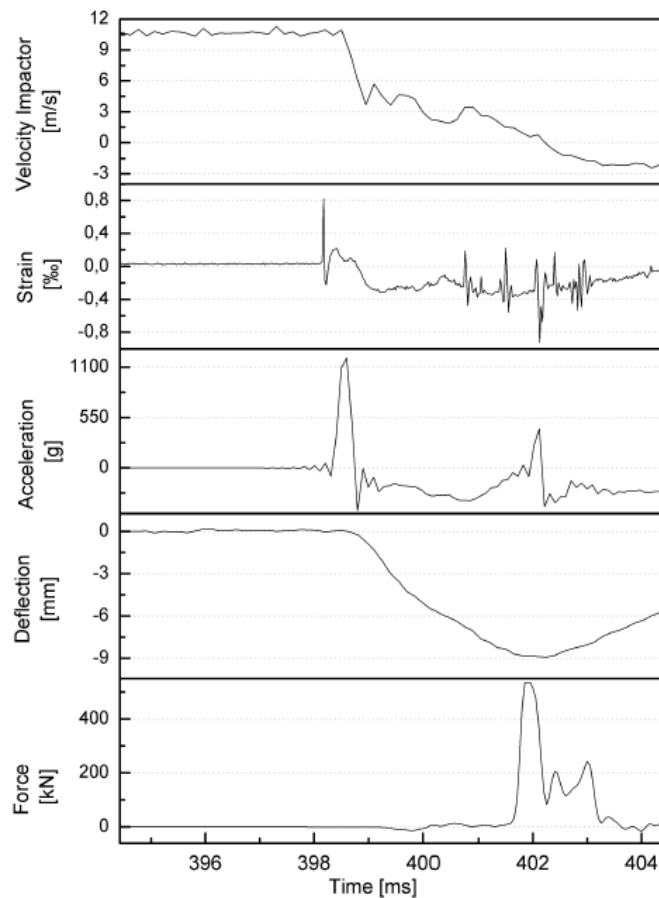


Figure 2.15. Measurements from slab D1
(Source: Hummeltenberg et al., 2011)

A study involving comparisons between numerical modeling and experimental data was conducted by Kishi et al. (2011). The tests were designed as falling-weight impact on RC slabs with three different types of support conditions; including supports along four edges, supports at opposite edges and supports at only one edge and point supports at two corners. Comparisons of numerical analysis with experimental data were made on time histories of dynamic response, maximum reaction forces, maximum deflections at the mid-point of slabs and major crack patterns.

Dimensions of RC slabs employed in tests were 2000x2000x180 mm and reinforcements were placed only at the bottom of the slabs with 150 mm spacing in both directions with 16 mm diameter. Reinforcement layout is given in Figure 2.16.

Load cells were placed at the supports to measure reaction forces and slabs were clamped at the corners to prevent lift off. Supports were allowed to rotate freely but horizontal movement was restrained.

Drop weight of the test was selected 300 kg and dropped freely at a fixed impact velocity of 4 m/s. The drop weight had a 90 mm diameter and its tip was spherical with a 507 mm radius and a 2 mm taper.

The deformations of the falling weight, supports and the load cells are assumed to be remained elastic region. The compressive strength of concrete was 26.6 MPa.

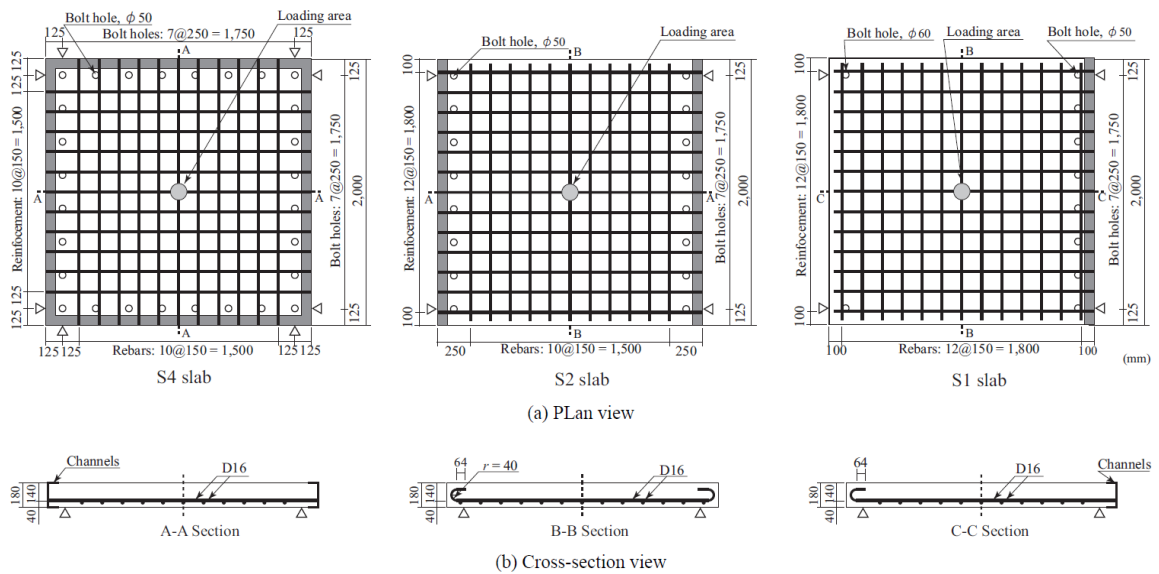


Figure 2.16. Dimensions, reinforcement layout and support conditions for each slab (Source: Kishi et al., 2011)

According to experimental results, maximum impact forces were independent from support conditions, and time history curves from numerical analysis were close to experimental data. However, maximum impact forces obtained from the numerical results were smaller than experimental results. For reaction forces, shapes of time histories did not seem different and deflection histories were also in similar shape to each other. In addition to deflection histories, maximum deflection of the slabs did not seem dependent on the boundary conditions (see Figure 2.17).

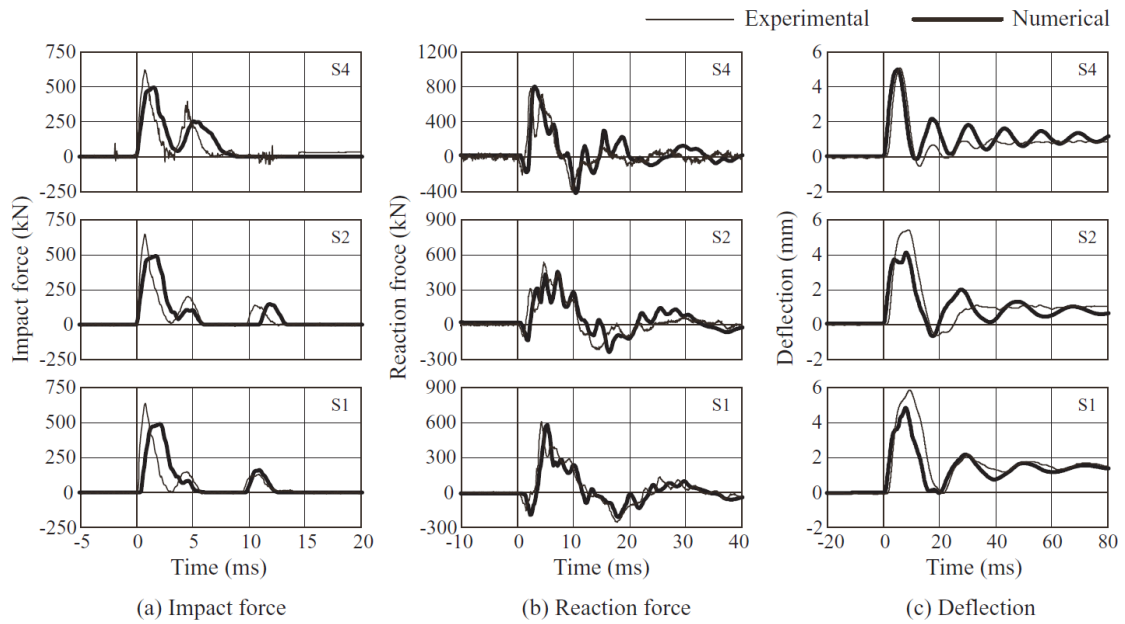


Figure 2.17. Time histories of impact force, reaction force and deflection
(Source: Kishi et al., 2011)

In Figure 2.18, it is clearly seen that S1 was more extensively cracked. Combination of punching shear, twisting moment and one way bending caused the crack patterns. Therefore, it can be indicated that the most flexible slab was S1 due to the support conditions.

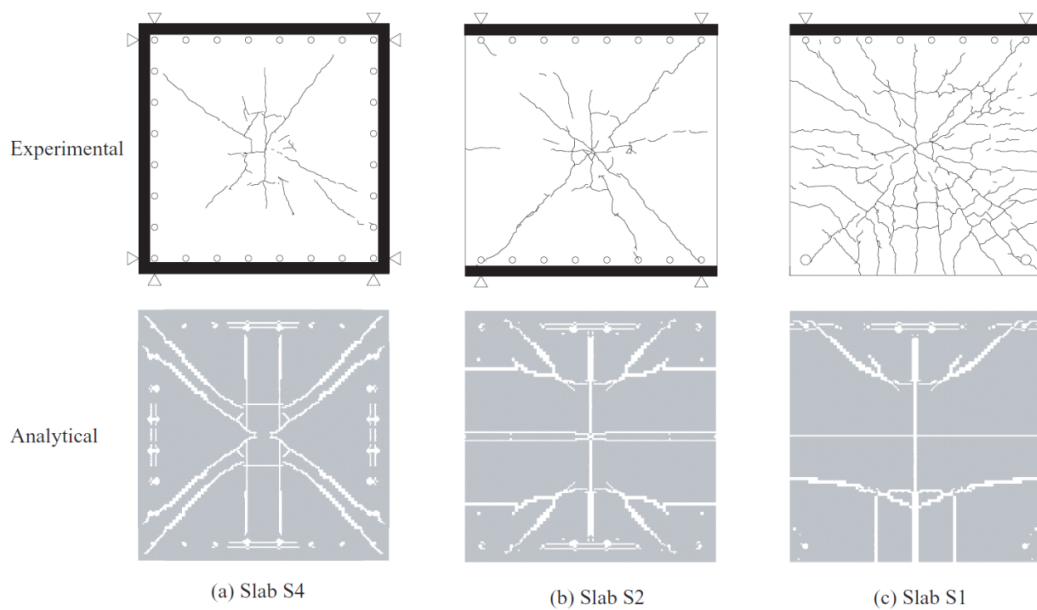


Figure 2.18. Crack patterns in each slab
(Source: Kishi et al., 2011)

Another experimental study on reinforced concrete slabs was carried out by Mougín et al. (2005). Their study concerned the rock-shed protection for mountainous regions. A concrete slab in 1/3 scale slab was cast for the test. Concrete strength was 30 MPa and steel reinforcement bars had 500 MPa yield strength. 8 mm diameter bars for shear reinforcement (vertical reinforcement), 14 mm diameter bars for longitudinal reinforcement and 16 mm diameter bars for transvers reinforcement were used. Throughout tests, a 450 kg block was from 30 m height. At the instant of the impact, the velocity was measured 24.5 m/s.

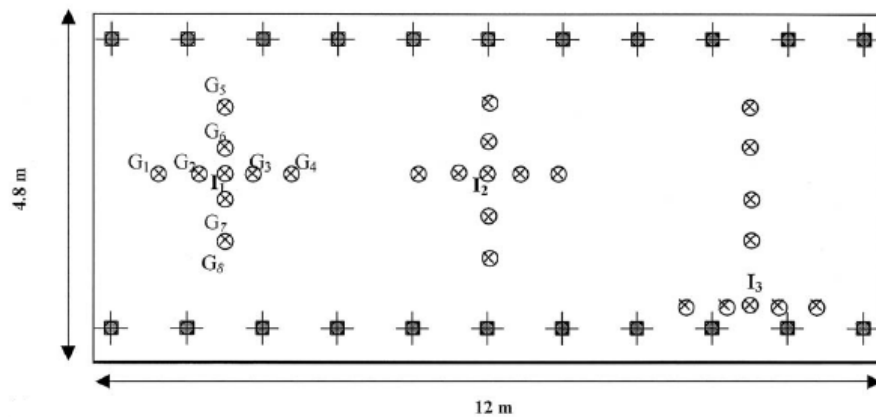


Figure 2.19. Illustration of the tested slab showing the impacted areas and position of stoneware clay sensors (Source: Mougín et al., 2005)

The slab was upheld by 26 specially designed supports and wet stoneware clay devices were used for measuring the displacements. This type of measurement device was based on penetration of a steel rod into the clay and measuring the depth of penetration after the test to obtain the maximum deflection. As a result, only maximum displacement profile of the slab was obtained (Figure 2.20).

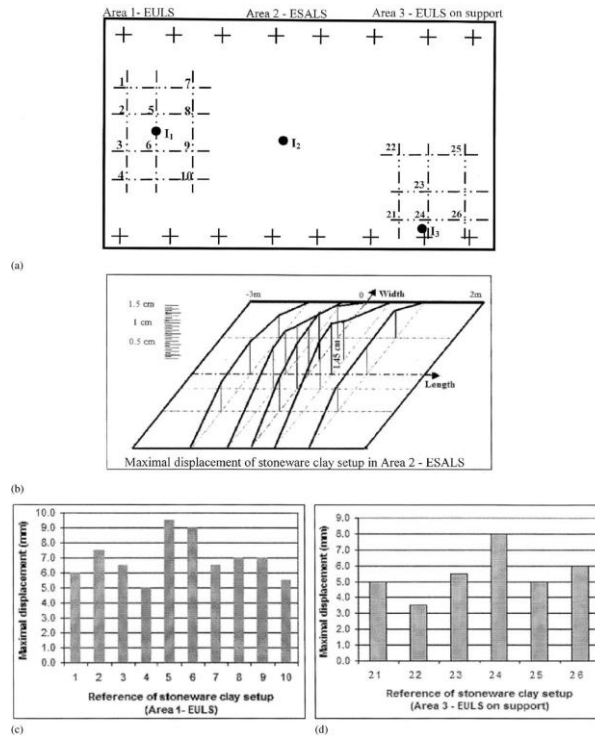


Figure 2.20. a) Localization of the impact points and stoneware clay devices on the slab; area 2, area 1 and area 3 displacements are presented in (b), (c) and (d) respectively. (Source: Mougin et al., 2005)

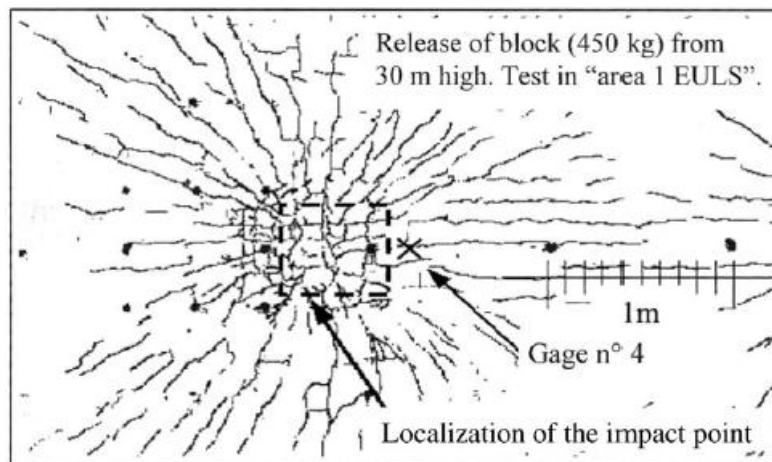


Figure 2.21. Local damage cracks on the slab surface in area 1 (Source: Mougin et al., 2005)

Another comparative study with large-scale was performed by Bhatti et al. (2011). To validate the numerical efforts in impact resistant design, actual conditions were tried to be built up. For this purpose, an RC structure used in parts of typical road tunnels was subjected to falling weight that imitates the falling rock. The falling weight

was 10000 kg and it was dropped from varying heights of 2.5, 5, 10 and 20 m. Figure 2.22 shows the details of experimental setup.

Only the highest case was considered for comparison of numerical analysis and experimental results (Figure 2.23).

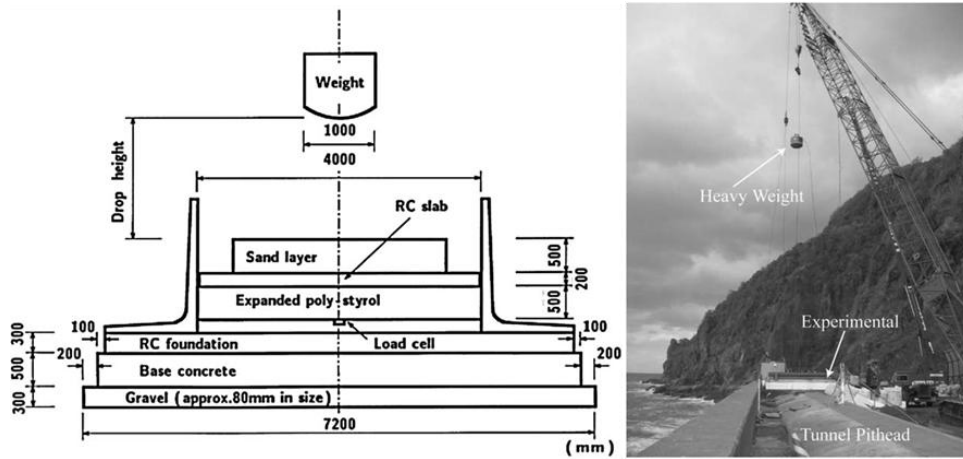


Figure 2.22. Details of setup
(Source: Bhatti et al., 2011)

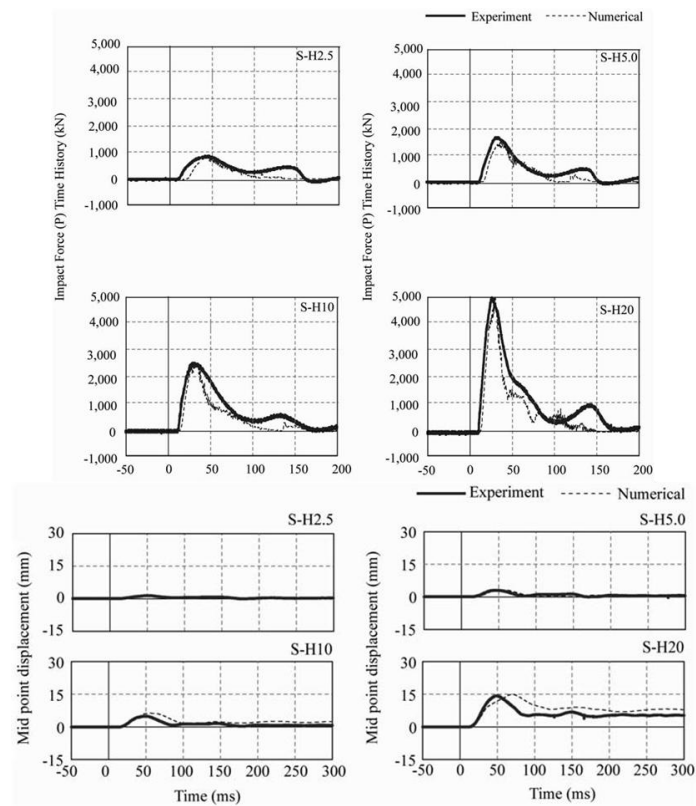


Figure 2.23. Time histories of impact and mid-point displacement
(Source: Bhatti et al., 2011)

CHAPTER 3

EXPERIMENTAL PROGRAM

Studying the behavior of reinforced concrete slabs subjected to impact loads requires a well-designed experimental program accompanied by numerical and analytical investigations. Experimental studies are crucial to the verification of analytical and numerical methods to be developed. Therefore, a well-instrumented test program was designed and executed in this study, results of which can be employed in further studies. This chapter explains the details of the test program, including test specimens, test setup and instrumentation.

3.1. Test Specimens

Six slab specimens were designed for the test program, which were tested under static and impact loads. Specimens were cast in three identical pairs and they were manufactured in Civil Engineering Structural Mechanics Laboratory at the İzmir Institute of Technology (IYTE). All three types of specimens had dimensions of 2015x2015x150 mm and 25 mm clear cover was provided for the reinforcement for all faces (see Figure 3.1).

Reinforcements of the slabs were in a mesh form, providing equal reinforcement ratio for all pairs of specimens. Meshes were obtained by bending the reinforcement bars at the middle to form top and bottom reinforcement from one single piece. $\phi 8$ steel bars, with 50.3 mm^2 cross-sectional area and 8 mm diameter, were used in all specimens, whereas spacing of the reinforcement were varied (see Figure 3.2).

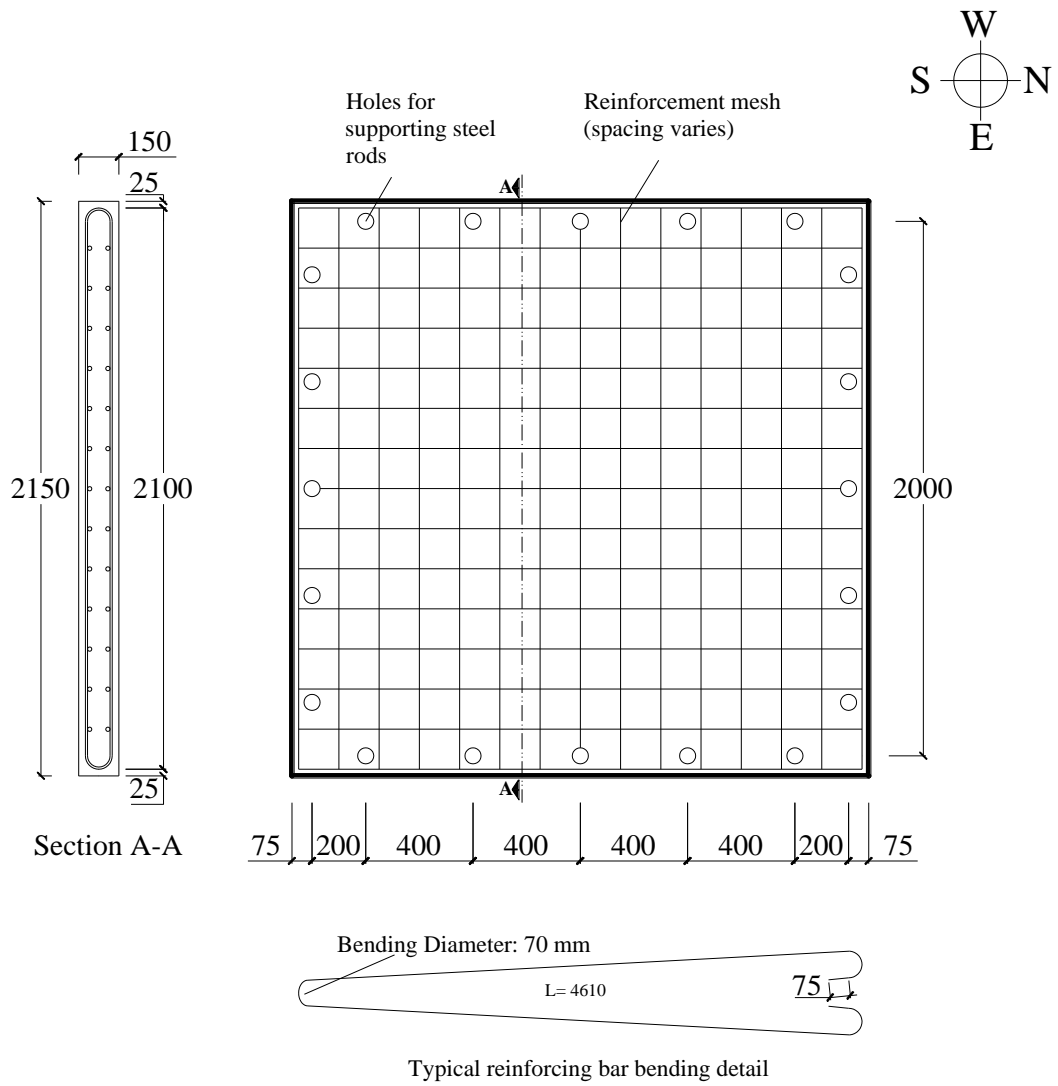


Figure 3.1. Test specimens (all dimensions in mm)

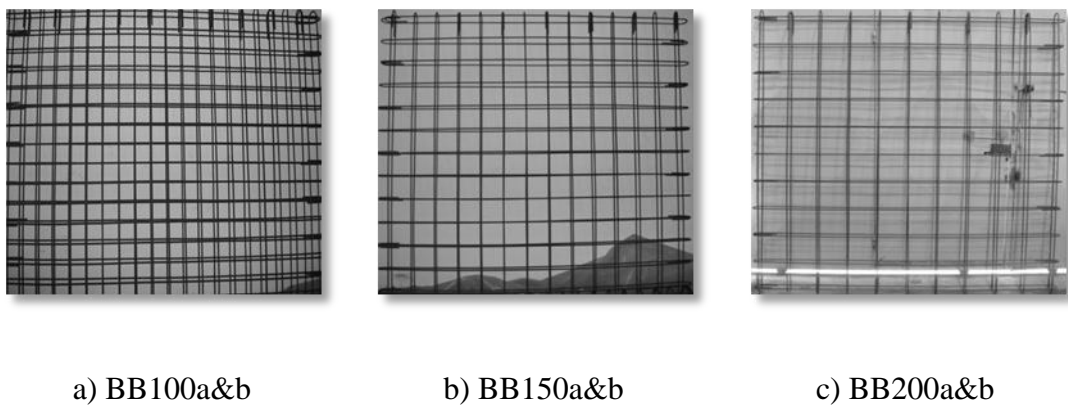


Figure 3.2. Reinforcing meshes for specimens

The specimens were named according to the spacing of the longitudinal reinforcement (see Figure 3.3). Tension reinforcement ratios for each direction, ρ , are given in Table 3.1.

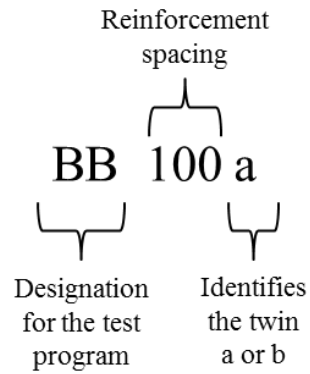


Figure 3.3. Naming conventions for the slabs

Table 3.1. Test specimens

<i>Specimen Name</i>	<i>Reinf. Mesh Layout (Bar Dia./Spacing, mm)</i>	<i>Tension Reinf. ratio for each Direction, ρ</i>
<i>BB100 a&b</i>	$\Phi 8/100$	0.40%
<i>BB150 a&b</i>	$\Phi 8/150$	0.30%
<i>BB200 a&b</i>	$\Phi 8/200$	0.20%



Figure 3.4 Manufacturing specimens

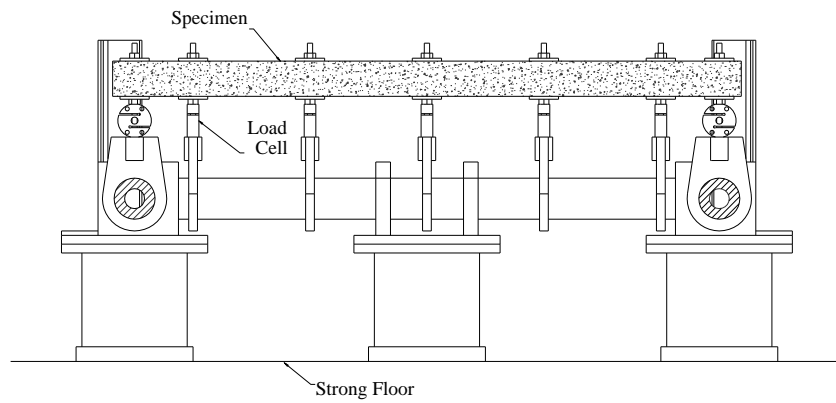
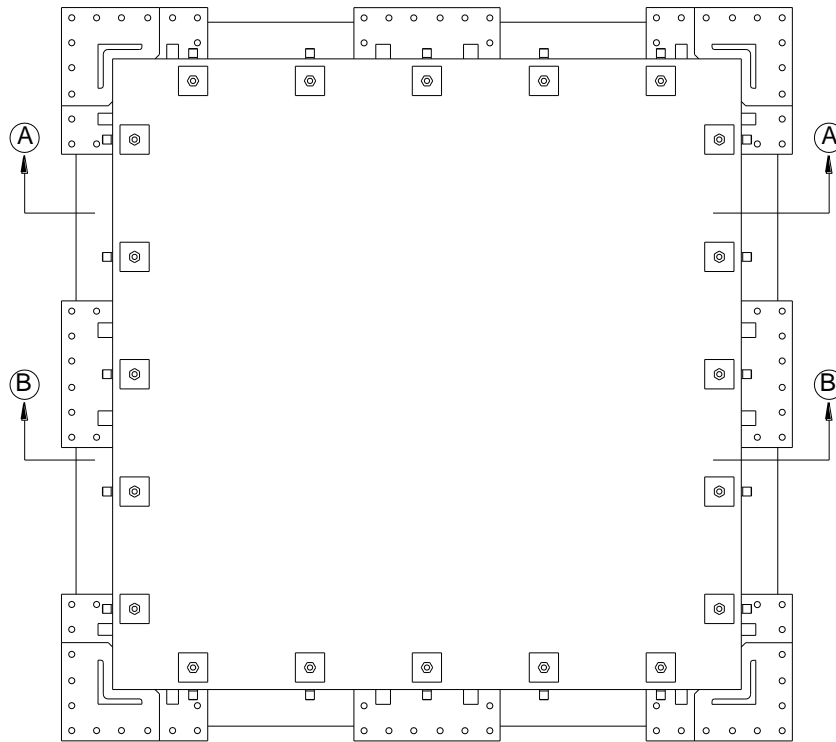
Manufacturing of formworks and casting specimens were carried out at the IYTE Structural Mechanics Laboratory (see Figure 3.4). All specimens were cast at the same time using the same concrete batch ordered from local company. Concrete properties are given in detail in section 3.3. Reinforcing steel material properties are also given in section 3.3.

3.2. Test Setup

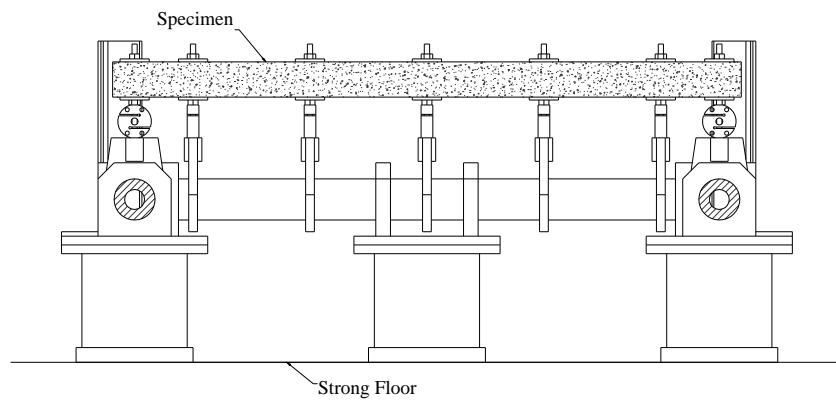
The experimental program of the study involves two phases; static and impact tests. For easier implementation of both tests, an innovative test setup was designed. The setup was manufactured in a local steel production company and mounted on the strong floor of the laboratory (see Figure 3.5).

Both static and impact tests were carried out using the same setup, providing the ideal simply supported conditions for the test specimens. The specimens were fixed on a steel frame at 20 locations. The connecting rods passing through the specimens were hinged on a circular shaft, allowing the free rotation of the ends yet restraining any vertical movement. This design aims to prevent uplift of the specimen without creating any moments at the supports during the impact and static tests. Each rod at the supports was equipped with a load cell, enabling the measurement of both tensile and compressive forces at the support point (Figure 3.6).

For both tests, setup remains same, but only loading procedure differs. In static tests, the slab was loaded at the mid-point using a hydraulic jack placed at the bottom of the slab and loading upwards. An extra load cell was placed between the jack and the specimen to measure the applied load. The load was applied through a circular steel plate of 200 mm diameter (see Figure 3.7).



Section A-A



Section B-B

Figure 3.5. Test setup

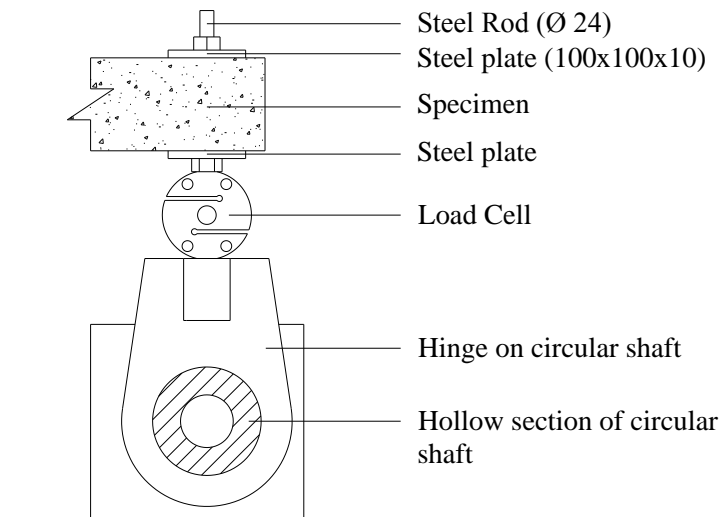


Figure 3.6. Detail of a hinge on the setup (all dimensions in mm)

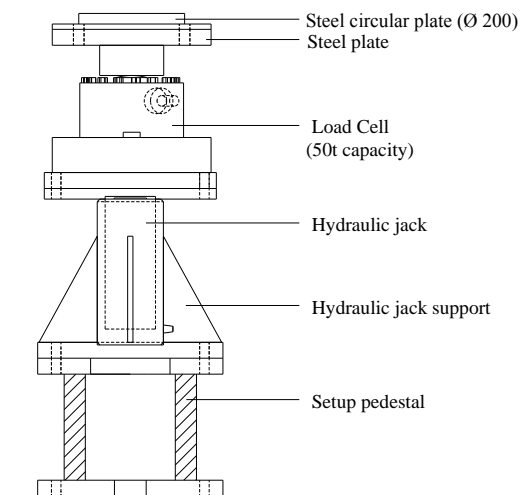


Figure 3.7. Hydraulic jack with the load cell

In impact tests, the impact load was applied by means of the free fall of a drop-weight from 2.5 m height (Figure 3.8). For free fall, the drop-weight was arranged for sliding between tracks on the drop-tower and impacted the specimens at the mid-point. The drop weight had a steel circular flat bottom of 200 mm in diameter, identical to the one used in static tests.

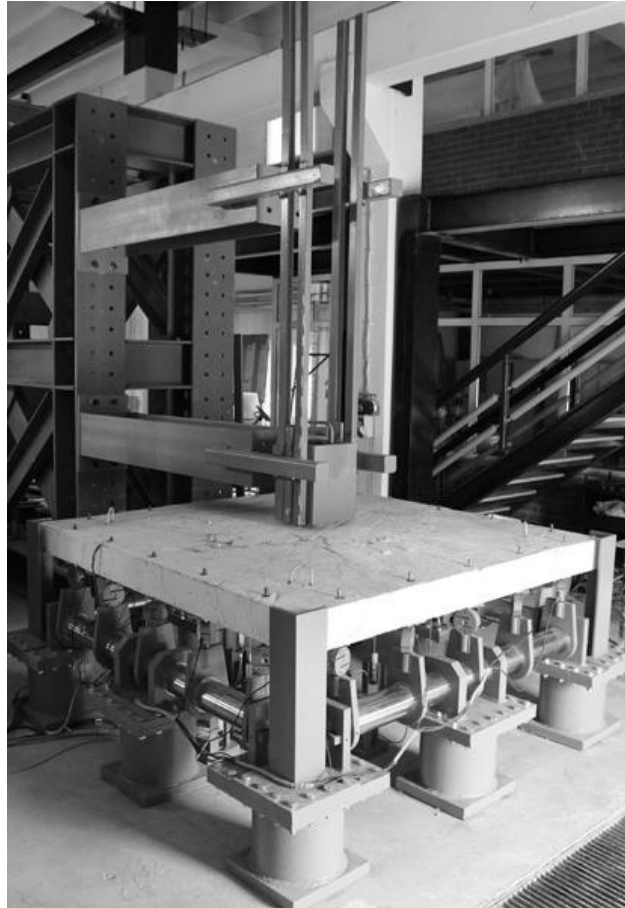


Figure 3.8. Test setup before impact test

3.3. Material Properties

The concrete used in the tests were ordered from local ready –mix company as mentioned before. All specimens were cast at the same time using the same concrete batch. Table 3.2. shows the compressive strength of the standard cylinder samples (150 mm in diameter and 300 mm in height) taken from the same concrete batch, cured and tested at the 28th day, 6 months and 20 months after the day of casting. Three specimens were tested at each date.

Reinforcement used in the specimens were tested as well, resulting $f_y=420$ MPa yield strength and $f_u=490$ MPa rupture strength.

Table 3.2. Cylinder test results

	<i>28th day</i>	<i>6 months after casting</i>	<i>20 months after casting</i>
	<i>Peak compressive stress, f_c' (MPa)</i>	<i>Peak compressive stress, f_c' (MPa)</i>	<i>Peak compressive stress, f_c' (MPa)</i>
<i>Standard cylinder samples</i>	20.9	31.5	28.5
	23.7	30.8	27.1
	21.7	28.5	30.2

3.4. Instrumentation

As mentioned before, the aim of the experimental program was to aid further analytical and numerical investigations. Therefore, specimens were extensively instrumented both for static and impact test in order to provide extensive experimental data. This section gives information about the measuring instruments employed during the experiments.

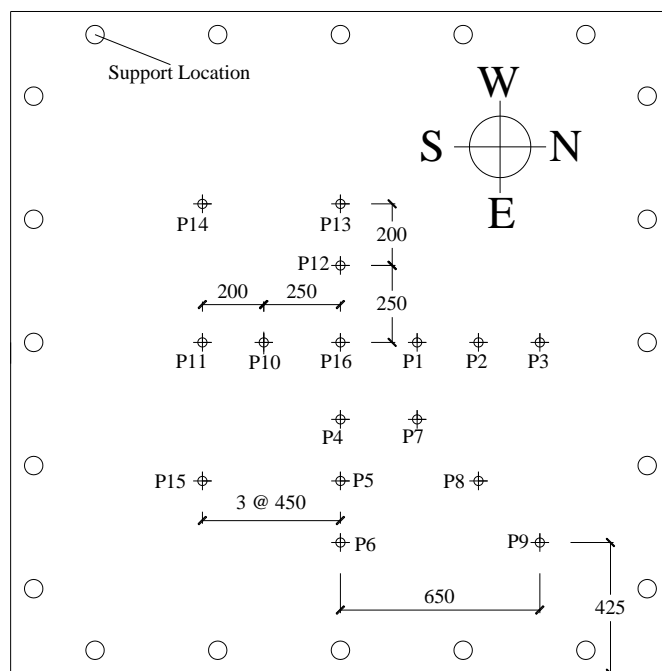
3.4.1. Resistive Linear Position Transducers (RLPT's)

Resistive linear position transducers (RLPT) were used to measure the displacements during the tests. All RLPTs are product of the same company (see Figure 3.9). Detailed product information is given in appendix A.



Figure 3.9. Resistive Linear Position Transducer

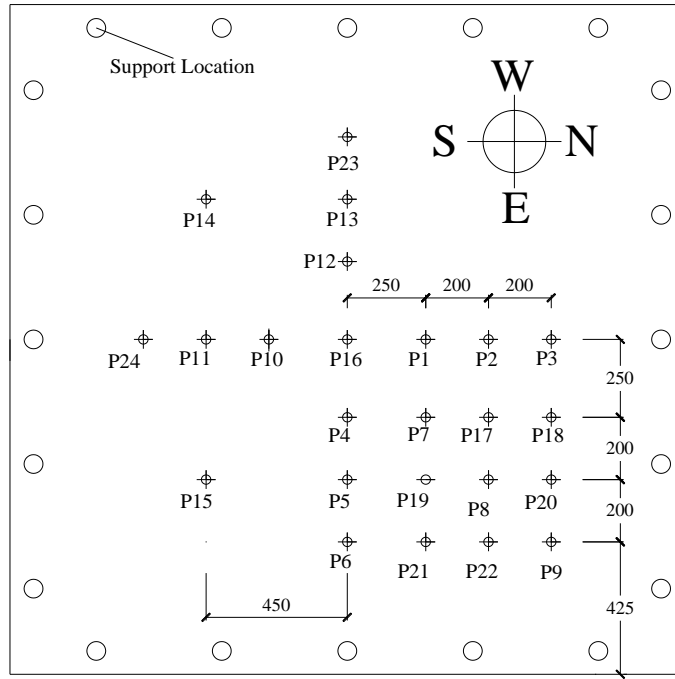
In both static and impact tests, RLPTs were connected to the specimens at the bottom. For the static tests, 16 transducers were used to measure the displacements. Because of the limited number of the transducers, locations of the RLPTs were tried to be chosen more efficiently to obtain the better displacement profile. Figure 3.10(a) shows the distribution of 16 RLPTs in static tests. In impact tests, numbers of RLPTs were increased. As seen on Figure 3.10(b), RLPTs were located closely on a grid at one quarter of the specimens to obtain accurate displacement profile. Additional RLPTs were located at symmetrical points with respect to horizontal and vertical axes. Steel extension rods were chosen to connect RLPTs to the hinges attached beneath the specimen in order to avoid any bending in the extension rods (Figure 3.11). Attachment of the hinges to specimen surface was provided by steel U-profiles screwed on the specimen surface. This kind of attachment was an acceptable solution for the static tests. But trial impact tests showed that screws in concrete cannot resist the impact load. Therefore, the hinges of the RLPTs were fixed into holes with epoxy for the impact tests (Figure 3.11). A view of the RLPTs for impact tests is shown in Figure 3.12.



a) RLPTs' locations for static tests

Figure 3.10. Locations of RLPTs (all dimensions in mm)

(cont. on next page)



b) RLPTs' locations for impact tests

Figure 3.10. (cont)

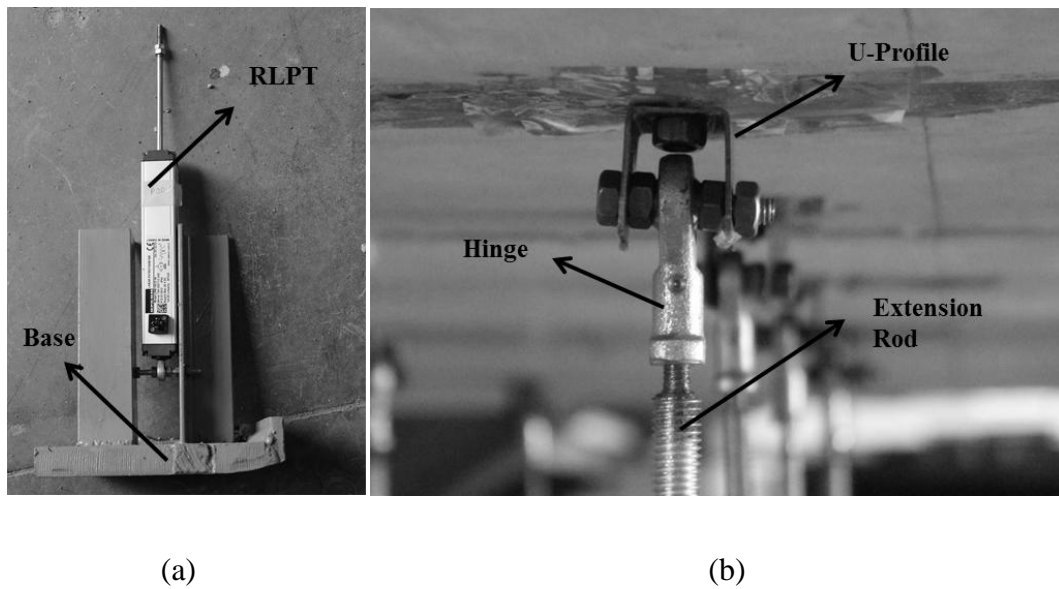


Figure 3.11. (a) Connection between potentiometer and rod; (b) connection between specimen and hinge



Figure 3.12. A view of RLPTs for impact tests

3.4.2. Strain Gauges

Strains of the reinforcing bars in the specimens were measured with strain gauges. 12 strain gauges were attached on the bar surfaces in total for each specimen, 6 of them for bottom reinforcement and 6 of them for the top reinforcement. The gauges were type FLA-5-11 with a 5 mm gauge length, manufactured by Tokyo Sokki Kenkyujo Co. Ltd. The reinforcement bars were grinded lightly and cleaned in order to obtain a suitable surface for the attachment of the gauges. The gauges were glued using the glue provided by the manufacturer. All gauges were well-coated by varnish and covered with paraffin wax and tape with the purpose of protection from water in concrete mix (see Figure 3.13).

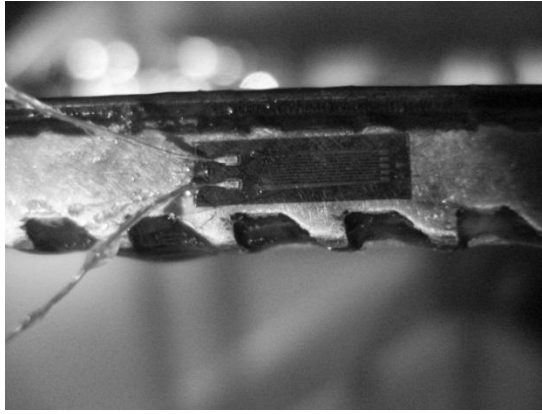


Figure 3.13. Strain gauge on bars before covered

Gauges were located on the diagonal axes in a quarter of the specimens. The exact locations of the gauges were also measured for each specimen before casting. Typical locations for each type of slab are shown in Figure 3.14, Figure 3.15 and Figure 3.16.

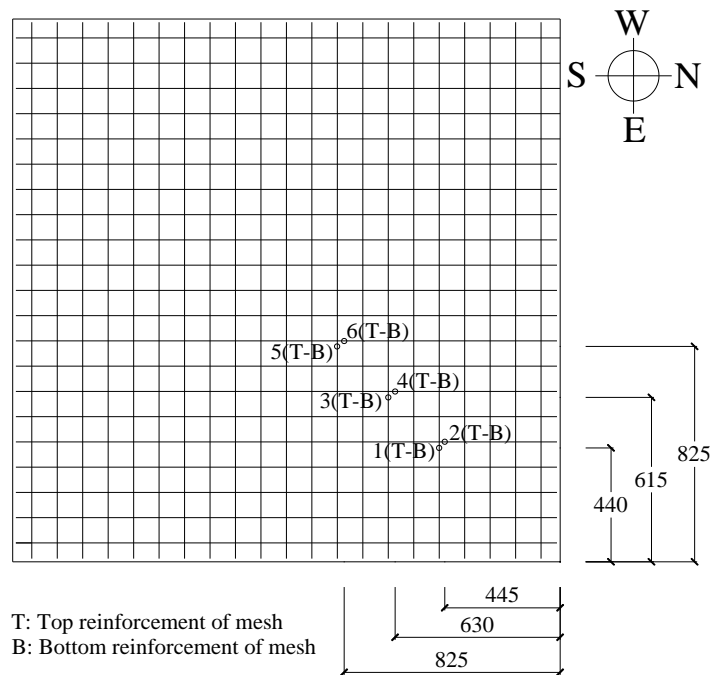


Figure 3.14. Strain gauge locations for BB100a&b (all dimensions in mm)

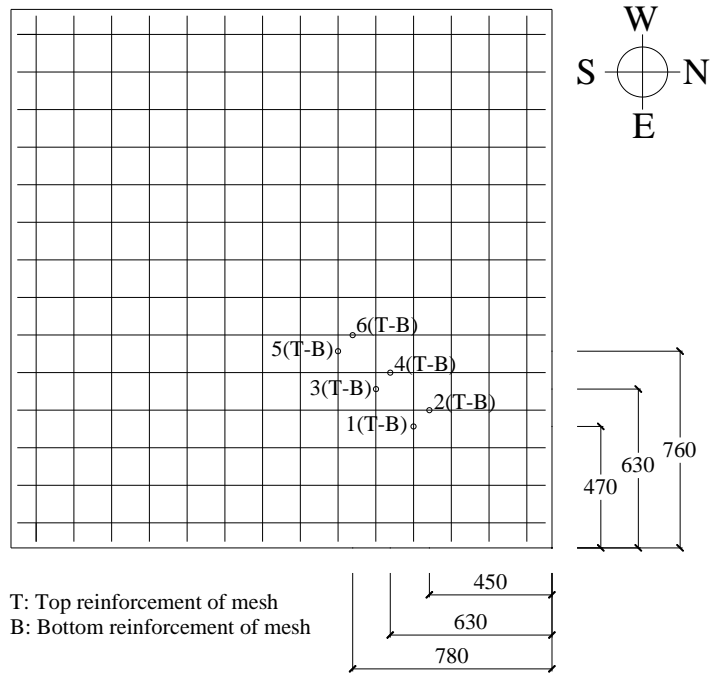


Figure 3.15. Strain gauge locations for BB150a&b (all dimensions in mm)

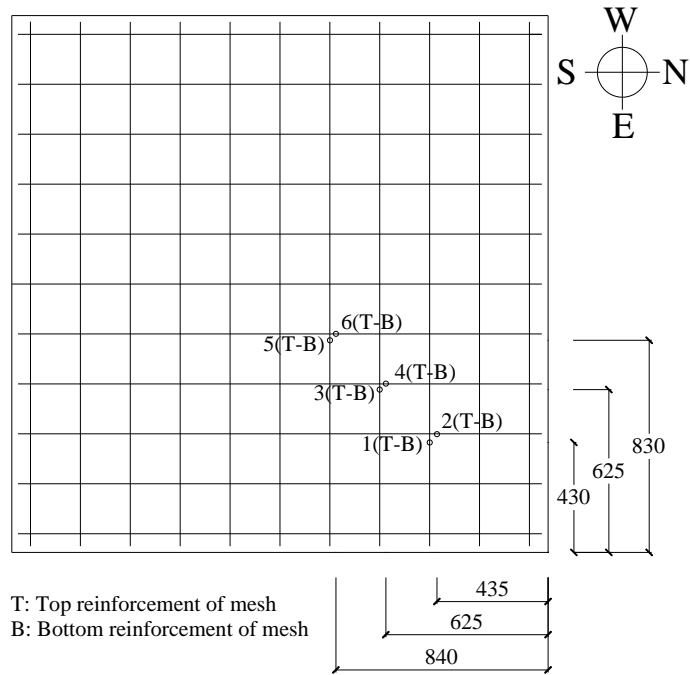


Figure 3.16. Strain gauge locations for BB200a&b (all dimensions in mm)

3.4.3. Load Cells

As mentioned earlier, the test setup was designed to provide simply supported conditions, allowing free rotation at the hinges. Load cells were placed on every hinge with the purpose of measuring reactions. The load cells used on the hinges were S type model TB with 5000 kg capacity and model SC with 10000 kg capacity, manufactured by ESIT Electronics Production and Trade Co. (Figure 3.17). In addition to the 5000 kg capacity load cells used in static tests, an extra load cell was placed on the hydraulic jack during static tests. After completing static tests, a few trial impact tests were carried out over damaged specimens from the static tests in order to test the performance of the setup and instruments under impact conditions. Those trials showed that during the impacts, three load cells in the middle of each side may exceed their capacities. For this reason, 12 of 5000 kg capacity load cells were replaced with 10000 kg capacity load cells.



Figure 3.17. 5000 kg (on the left) and 10000 kg capacity (on the right) load cells on the hinge

3.4.4. Accelerometers

Accelerometers used in impact tests were products of Kistler Group. Two types of accelerometers were selected to measure accelerations on specimens and drop weight. Four 8742A5 type of the accelerometers with $\pm 5000g$ range were mounted on specimens (Figure 3.18) and two 8742A50 type of accelerometers with $\pm 50000g$ range were mounted on the drop weight. Four of the accelerometers mounted on the specimen

were attached to bolts that were embedded 3 - 4 cm into specimens. Rubber washers were used between all accelerometers and metal surfaces to reduce unwanted high-frequency vibrations. Protection blocks were manufactured to prevent any damages from debris during impact (Figure 3.19).

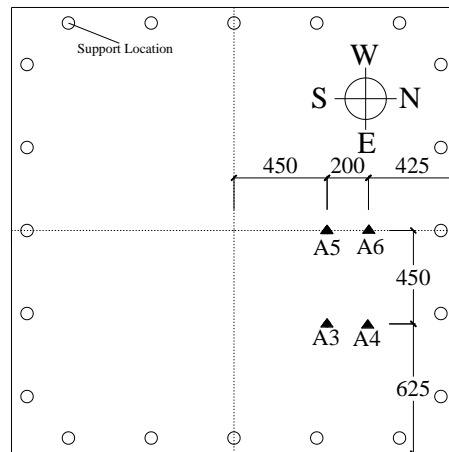


Figure 3.18. Locations of accelerometers (all dimensions in mm)

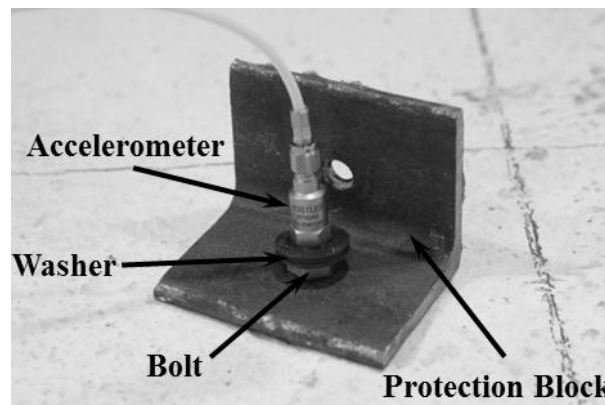


Figure 3.19. Accelerometer and protection block

3.4.5. Data Acquisition System

For all tests, a high speed data acquisition system was employed (Figure 3.20). National Instruments NI PXI-6143 S series multifunction device was used for recording and capturing data at a rate of 250 kilosample/second/channel. 8-channel universal strain/bridge module (SCXI-1520), 8-channel ICP accelerometer module (SCXI-1531), and SCB-68 connector block were also used to gather data for strains, accelerations and

displacements. Data were acquired with the help of LabVIEW Academic Standard Suite software.



Figure 3.20. Data acquisition system

3.4.6. Drop Weights

Two hollow steel buckets with a 200 mm diameter flat impact surface was manufactured by a local steel company in order to obtain varied weights (Figure 3.21). For this purpose, one of the buckets was filled with only concrete (Figure 3.22a) and other bucket was filled with both steel plates and fine aggregate concrete. First impact test on BB100b revealed that neither drop weight can have enough energy to cause significant damage. Therefore, four additional steel plates were welded on the lighter bucket to increase weight (Figure 3.22b). By the end, two drop weights were used in tests, lighter with a 210 kg mass and heavier with a 320 kg mass.

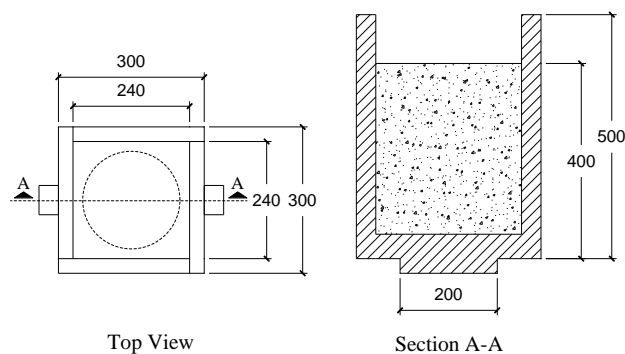


Figure 3.21. Details of drop weights (all dimensions in mm)

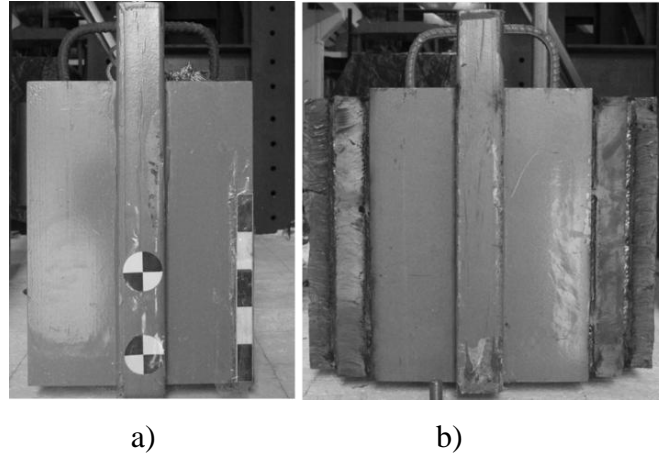


Figure 3.22. Drop weights (210 kg and 320 kg, respectively)

3.4.7. High-Speed Camera

Impact tests were recorded by the MotionBLITZ high speed camera system, product of Mikrotron GmbH. The camera is able to record at rate from 50 to 16000 fps. Frame rates were changed from 800 fps to 1262 fps throughout the impact test. General view of the test setup was recorded with this camera and impact velocity of the drop weight was measured by the analysis of recorded frames.

3.5. Loading Protocol

As pointed out previously, the experimental program consists of two phases: static and impact phases. In this manner, three identical pairs of specimens were manufactured in order to employ the test to specimens with the same characteristic.

At the first stage of the experiments, static tests were carried out for all three specimens. After execution of the static tests, impact tests followed the procedure. Following sections briefly describe the test procedures.

3.5.1. Static Tests

Static tests were carried out by loading the specimens at their mid-point with a manually operated hydraulic jack. During testing, loading was stopped few times to mark the cracks and take photographs of the specimens. Loading was continued until specimens failed by punching.

3.5.1.1. BB100a (Test Date: February 13, 2012)

Load carrying capacity of BB100a, with the highest reinforcement ratio, was highest among all specimens. It reached 248 kN capacity and the mid-point displacement was 24 mm before the failure. Figure 3.23 shows the crack profile of the specimen after test.

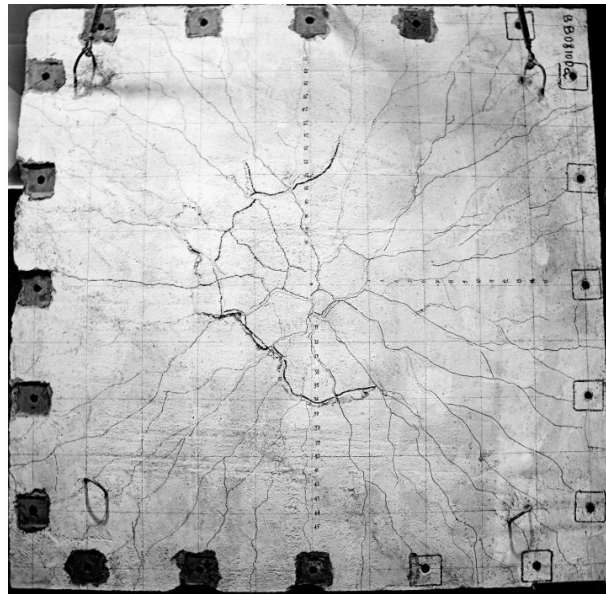


Figure 3.23. View of the BB100a tension surface after test

3.5.1.2. BB150a (Test Date: March 01, 2012)

Loading capacity of BB150a reached 184 kN and the mid-point displacement of the specimen was 34 mm before the failure. Figure 3.24 shows the crack profile of the specimen after test.

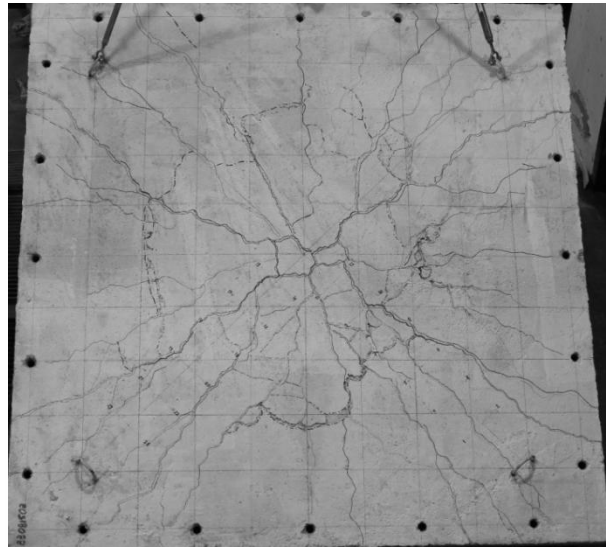


Figure 3.24. View of the BB150a tension surface after test

3.5.1.3. BB200a (Test Date: March 14, 2012)

Load carrying capacity of BB200a, specimen with the lowest reinforcement ratio, was lowest as expected. The capacity reached 161 kN. However, BB200a showed higher ductility than the other specimens. The mid - point displacement was 43 mm before the failure. Figure 3.25 shows the crack profile of the specimen after test.

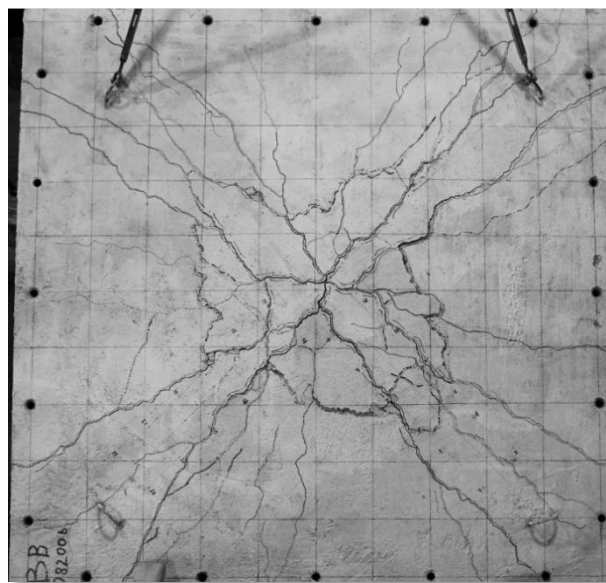


Figure 3.25. View of the BB200a tension surface after test

3.5.2. Impact Tests

The test setup was arranged for the impact test such as removing the hydraulic jack from the middle of the setup and mounting the drop tower. Drop weights of the impact tests varied according to specimen, whereas the height of the free fall was fixed at 2.5 m, resulting 7.0 m/s contact velocity at the instant of impact. The first of the impact tests was performed on BB100b with the highest reinforcement ratio showed 210 kg weight was insufficient to cause a significant damage. Hence, weight of one of the drop weights was increased to 320 kg, as mentioned before. Two more drops were applied on this specimen. Only one drop of 320 kg created significant cracking and scabbing on BB150b. In accordance with these experiences, lighter drop weight was used on BB200b. For all these impact tests, excessive scabbing or perforation of the drop weight was tried to be prevented. To obtain the crack profiles, cracks were marked after every impact. Table 3.3. shows the impact protocol briefly. Following sections summarize the individual tests. Note that the number following the specimen name indicates the number of impact test carried on the specimen.

Table 3.3. Loading protocol for impact tests

<i>Impact #</i>	<i>Drop-Weight (kg)</i>		
	<i>BB100b</i>	<i>BB150b</i>	<i>BB200b</i>
1	210	320	210
2	320	-	210
3	320	-	-

3.5.2.1. BB100b-1 (Test Date: January 24, 2013, Drop Weight: 210 kg)

In the first of the impact tests, BB100b was subjected to 210 kg drop weight. Hardly visible cracks were occurred and connection of the RLPTs P10, P12, and P16 detached after the impact.

3.5.2.2.BB100b-2 (Test Date: February 12, 2013, Drop Weight: 320 kg)

The second impact on BB100b was with 320 kg drop weight. Detached RLPTs from first impact test were reattached to the specimen, but the same RLPTs- P10, P12, and P16 –came off from the specimen. Existing cracks became more visible and a circumferential crack occurred. Moreover, a punching behavior and penetration of the drop weight were observed after the impact.

3.5.2.3.BB100b-3 (Test Date: February 12, 2013, Drop Weight: 320 kg)

The third and the last impact on specimen BB100b caused significant spalling compared to the previous impact. Before carrying out the test, all RLPTS were checked and repaired their connections. Therefore, RLPTs P4, P7 and P10 were detached as a result of scabbing. Additionally, two more RLPTs P1 and P16 also came off during the impact. Depth of penetration reached approximately 3 cm. Figure 3.26 shows the bottom surface of the specimen after the impact.

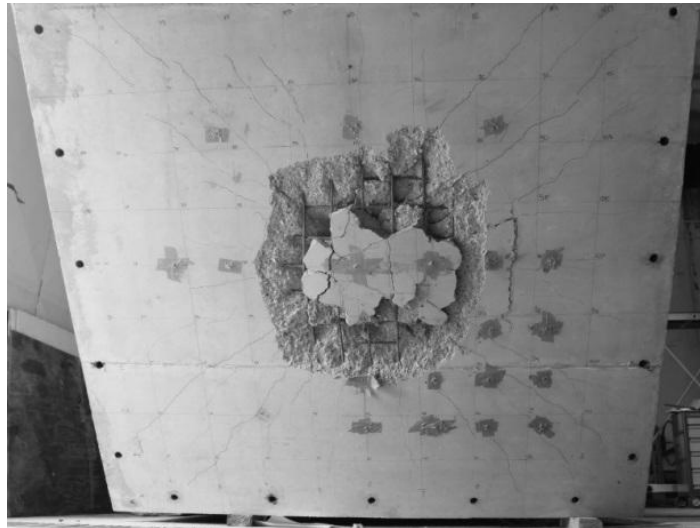


Figure 3.26. Final state of the specimen BB100b after second impact

3.5.2.4.BB150b-1 (Test Date: April 18, 2013, Drop Weight: 320 kg)

BB150b was subjected to impact only once to prevent excessive scabbing. Apparent cracks, penetration of the drop weight and punching cone formation were observed. Two RLPTs P4 and P13 came off from the specimen. Bottom surface of the specimen can be seen in Figure 3.27 after the impact.

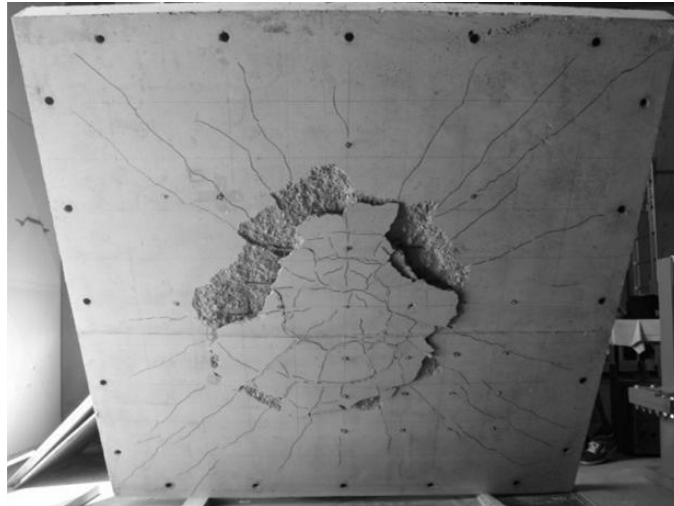


Figure 3.27. Final state of the specimen BB150b after impact test

3.5.2.5.BB200b-1 (Test Date: April 30, 2013, Drop Weight: 210 kg)

Among the specimens for the impact series, BB200b was the one which had no loss of the RLPTs. Radial crack profile was clearly seen with respect to first impact of other specimens.

3.5.2.6.BB200b-2 (Test Date: April 30, 2013, Drop Weight: 210 kg)

The impact test series ended with BB200b-2. Three RLPTs P7, P12 and P13 were detached. Drop weight penetration was increased and cracks were widened as expected. Figure 3.28 shows bottom surface of the specimen after tests.

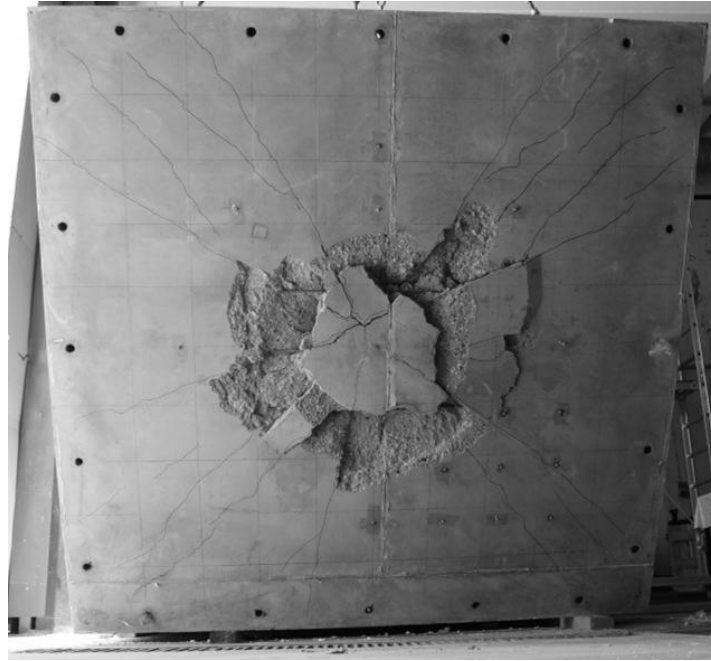


Figure 3.28. Final state of the specimen BB200b after impact test

3.5.3. Punching Cone Observations

As mentioned previously, all specimens were tested until failure, and crack profiles of all specimens were sketched (see Sections 4.1. and 4.3). Using these profiles, punching cone diameters were approximately calculated (see Figure 3.29 for BB100b).

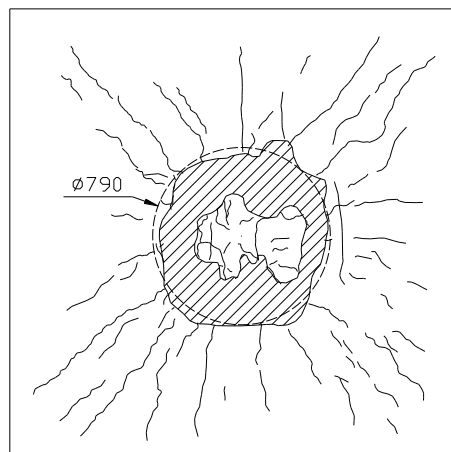


Figure 3.29. Punching cone diameter for BB100b

Angles of punching cones for each slab were also calculated as shown in Figure 3.30. Table 3.4. shows the angles (β) of punching cones for each slab.

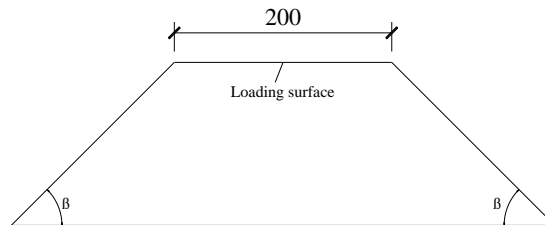


Figure 3.30. Typical punching cone

Table 3.4. Punching cone angles for all specimens

	<i>Static Tests</i>			<i>Impact Tests</i>		
	<i>BB100a</i>	<i>BB150a</i>	<i>BB200a</i>	<i>BB100b</i>	<i>BB150b</i>	<i>BB200b</i>
<i>Angle, β (degree)</i>	32	20	28.6	27	20	27

CHAPTER 4

DISCUSSION OF RESULTS

In the previous chapter, the test program and the details of data collection were explained. In this chapter, collected data are meticulously examined and the findings are discussed.

4.1. Static Test Observations

This section presents the observations made during the static tests in the form of crack patterns of specimens and the load –midpoint displacement responses at different stages of loading. As mentioned in the previous chapter, loading has stopped a few times to mark the cracks and take photos in order to acquire the progress of crack profiles.

4.1.1. BB100a (Test Date: February 13, 2012)

Crack patterns of this specimen were recorded at four stages during testing. Loading has stopped at 5 mm, 12 mm, 20 mm midpoint displacements and formed cracks were traced. Final state of the crack pattern was recorded at failure (24 mm). Cracks on the tension surface were concentrated on diagonals, extending radially from the loading point (center) towards the edges of the specimen. With the increased loading, newer cracks developed along the middle axes and cracks were widely spread on tension surface as clearly seen in Figure 4.1. As expected, specimen failed by punching. The circular loading plate punched suddenly and slight scabbing and circular wide cracks were observed around the center on tension surface as a result of the punching cone (Figure 4.1d).

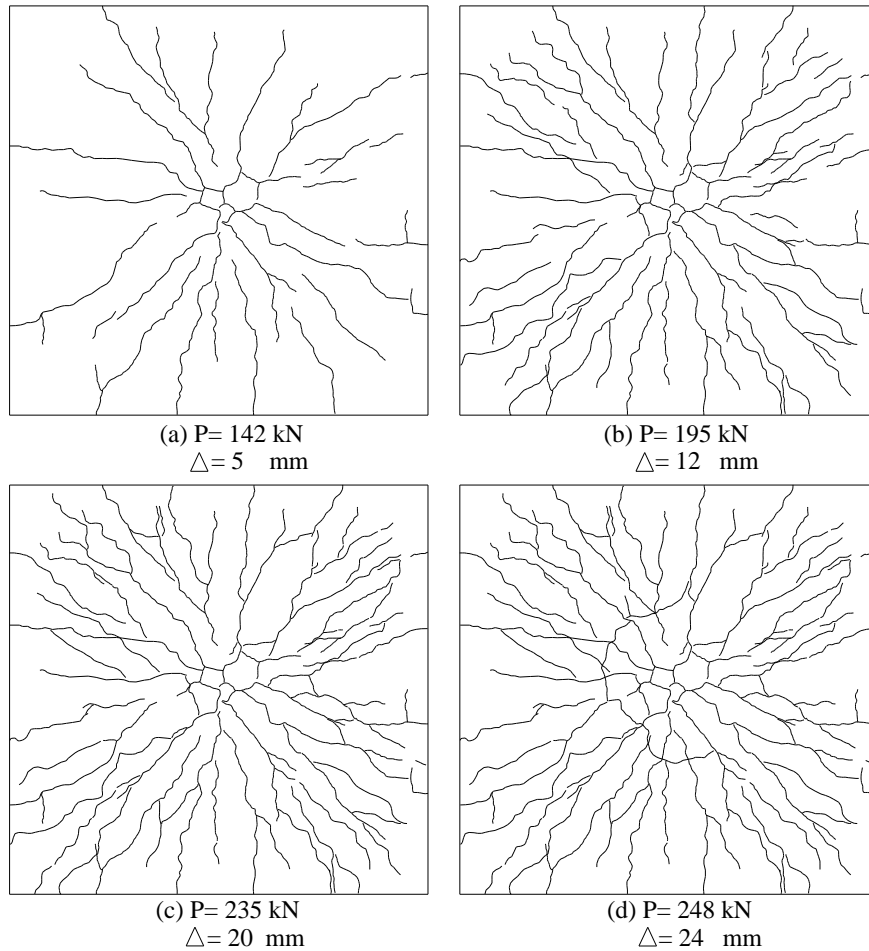


Figure 4.1. Crack profiles of tension surface for BB100a specimen

4.1.2. BB150a (Test Date: March 01, 2012)

For BB150a, loading applied at five stages to record crack profiles. Spacing of reinforcement for this specimen was larger than BB100a. Therefore, crack formation started to develop in early stages compared to BB100a as expected (Figure 4.2). However, wider cracks were observed in BB150a for the same midpoint displacements and loads with respect to BB100a. This specimen failed by punching as well and punching region can be seen from the tension surface which is shown in Figure 4.2e.

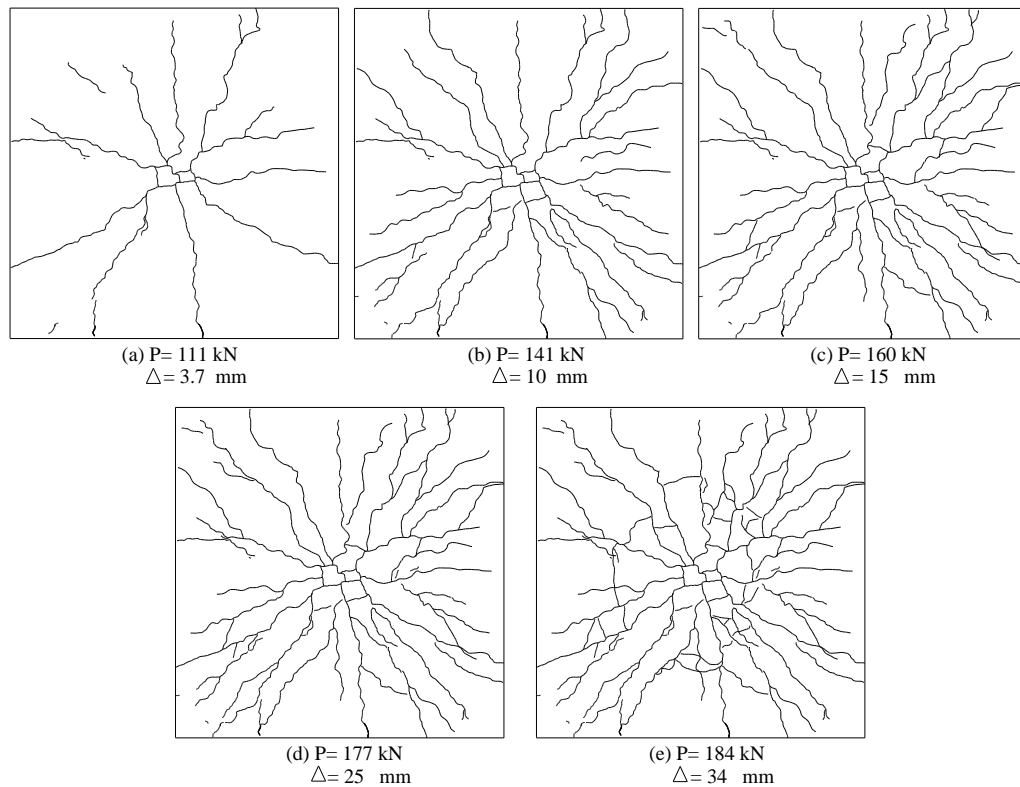


Figure 4.2. Crack profiles of tension surface for BB150a specimen

4.1.3. BB200a (Test Date: March 14, 2012)

Specimen BB200a with lesser amount of ratio showed higher ductility but lower strength as a result of reinforcement spacing. In BB200a, cracks were wider and decreased in number compared to the other two static tests.

In three static tests, the highest midpoint displacement was measured in BB200a (Figure 4.3e). On the other hand load carrying capacity of this specimen was the lowest among three. In other words, the specimens with lesser amount of reinforcement ratios carried lesser amount of load, but they were able to sustain the load with increasing displacement.

All statically tested specimens were failed by sudden punching, created visible punching cone from the tension surface as circular wide cracks around the center.

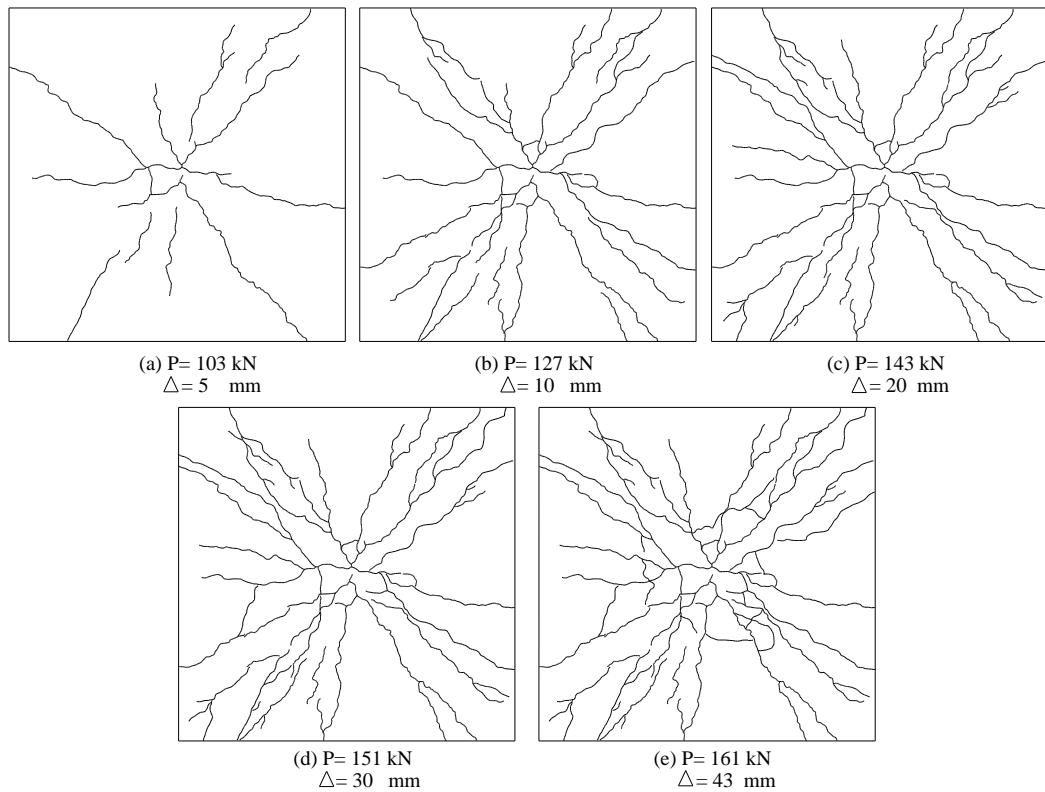


Figure 4.3. Crack profiles of tension surface for BB200a specimen

4.2. Discussion of Static Tests

Capacities of the specimens obtained from the static tests should be compared and interpreted with common formulations available in the literature. For this purpose, current code provisions - ACI 318 2011, CSA A23.3-04, EC2 2004 and TS 500 - were investigated in order to calculate the punching strength of slabs. In addition to punching capacities of slabs, yield line mechanisms were investigated as well to predict the flexural strength of slabs. Following sections present the details of these calculations.

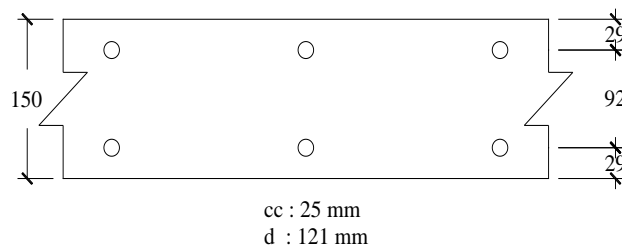


Figure 4.4. Strip illustration of slab (cc is clear cover; d is effective depth)

4.2.1. Flexural Strength

A software, Response2000 (Bentz 2000), was employed to calculate the moment-curvature behavior of a strip of slabs. Figure 4.4 shows a strip illustration of the slab that includes some parameters used in calculations. To compute the ultimate moment capacity of slabs, yield line theory was employed. This method depends on estimation of a collapse mechanism with compatible boundary conditions and computation of ultimate load using the principle of virtual work. For the determination of a collapse mechanism for tested slabs, three of yield line mechanisms were examined to calculate the flexural strength of slabs. Among the calculated capacities for each case, the most critical case was chosen as the ultimate flexural capacity.

- Yield Line Mechanism – Case A

This failure mechanism is formed by a point load at the middle and diagonal yield lines extending from center to the corners. Note that the positive (M_u) and negative (M_u') moment capacities are identical due to the symmetric reinforcement placement (Eq. 4.1). For a virtual displacement δ at the center, the work done by internal and external forces are given in the left and right side of Eq. 4.2, respectively, where L is the length of one side of the square slab. The ultimate load P depending on the moment capacity is given in Eq. 4.3.

$$M_u = M_u' \quad (4.1)$$

$$4M_u L \frac{\delta}{L/2} = P\delta \quad (4.2)$$

$$P = 8M_u \quad (4.3)$$

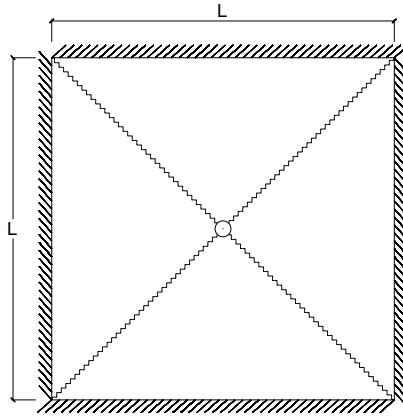


Figure 4.5. Yield line mechanism (Case A)

- Yield Line Mechanism – Case B

This mechanism is formed by the point load at the middle and radial fan of yield lines. The calculated load capacity is given in Eq. 4.4.

$$P = 2\pi(M'_u + M_u) = 12,6M_u \quad (4.4)$$

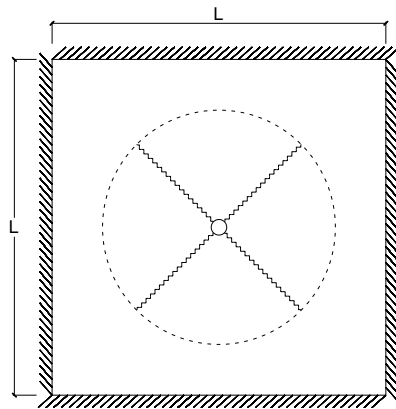


Figure 4.6. Yield line mechanism (Case B)

- Yield Line Mechanism – Case C

This failure mechanism is formed by the circular loading plate with radius r_c (100 mm), creating yield lines at the circumference of the loading plate and a fan of yield lines extending radially with a radius of r (1000 mm). Calculated internal and external work due to a virtual

displacement δ of the loading plate is given at the left and right sides of Eq. 4.5, respectively.

$$\left(\frac{2\delta\pi}{r_c}\right)(M_u' + M_u) = P\delta \quad (4.5)$$

Substituting Eq. 4.1, ultimate load capacity P can be calculated as follows.

$$P = \frac{4\pi r M_u}{r - r_c} = 13,96 M_u \quad (4.6)$$

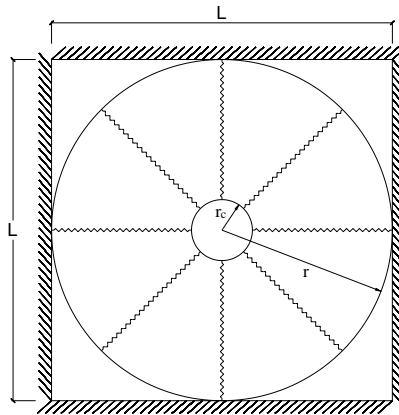


Figure 4.7. Yield line mechanism (Case C)

According to calculations of each case of yield line mechanisms, the most critical case is found to be Case A. Ultimate sectional moment capacities of a unit strip (M_u) were obtained using software Response2000. Moment-curvature diagram for each type of slab as calculated by Response2000 are shown in Figure 4.8.

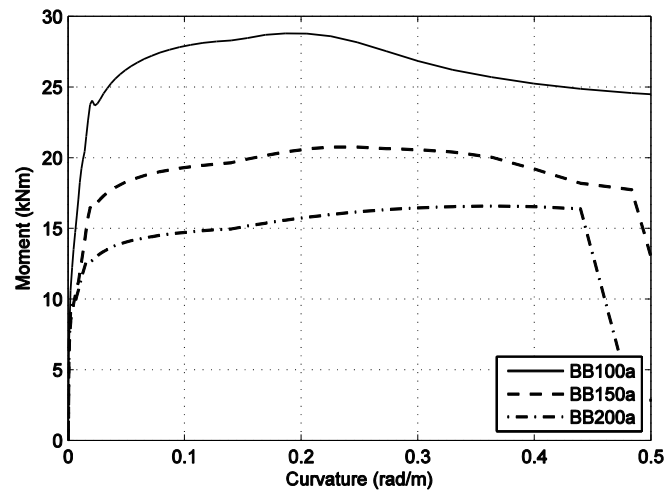


Figure 4.8. Moment- curvature diagrams obtained from Response2000

According to results of Response2000, loading capacities causing flexural failure of slabs were computed as follows:

For specimen BB100a: $P_u = 8(28,8) = 230$ kN;

For specimen BB150a: $P_u = 8(21,1) = 169$ kN;

For specimen BB200a: $P_u = 8(16,6) = 133$ kN;

4.2.2. Punching Strength

As stated previously, four of current codes were employed to calculate the punching capacities of the specimens.

4.2.2.1. ACI 318-11 (American Concrete Institute, 2011)

The provision of ACI 318-11 expresses the punching strength of nonprestressed slabs and footings in three categories. The smallest of three should be selected as punching shear strength of structure (Eq. 4.8a, Eq. 4.9a and Eq. 4.10a). Figure 4.9 shows the control perimeter of tested slabs loaded by a circular loading plate with 200 mm diameter.

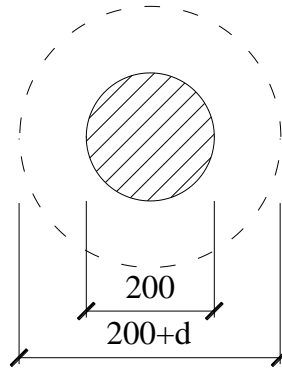


Figure 4.9. Control perimeter according to ACI 318-11 Clause 11.11.1.2

Hence, control perimeter can be calculated as in Eq. 4.7, where effective depth, d is 121 mm.

$$b_0 = \pi(200 + 121) = 1008 \text{ mm} \quad (4.7)$$

According to Clause 11.11.2.1, three capacities can be calculated as follows.

$$V_c = 0,17 \left(1 + \frac{2}{\beta} \right) \lambda \sqrt{f_c} b_0 d \quad (4.8a)$$

$$V_c = 0,17 \left(1 + \frac{2}{1} \right) 1 \sqrt{30} (1008) (121) = 377 \text{ kN} \quad (4.8b)$$

$$V_c = 0,0083 \left(\frac{\alpha_s d}{b_0} + 2 \right) \lambda \sqrt{f_c} b_0 d \quad (4.9a)$$

$$V_c = 0,0083 \left(\frac{40(121)}{1008} + 2 \right) 1 \sqrt{30} (1008) (121) = 377 \text{ kN} \quad (4.9b)$$

$$V_c = 0,33 \lambda \sqrt{f_c} b_0 d \quad (4.10a)$$

$$V_c = 0,33(1) \sqrt{30} (1008) (121) = 220 \text{ kN} \quad (4.10b)$$

where,

f_c = the compressive strength of concrete in MPa

d = effective depth of the slab

β = ratio of long to short spans;

λ = modification factor reflecting the reduced mechanical properties of lightweight concrete, all relative to normal weight concrete of the same compressive strength. This parameter is taken as 1.0 for normal strength concrete.

Accordingly, punching capacity of the slabs is calculated as 220 kN using ACI 318-11.

4.2.2.2. CSA A23.3-04 (Canadian Standards Association, 2004)

Punching strengths were also categorized in Canadian standards. The smallest of three calculations (Eq. 4.11, Eq. 4.12 and Eq. 4.13) should be selected as punching shear strength of structure. Control perimeter, b_0 was defined as in ACI 318-11 (Eq.4.7). Three capacities can be calculated as follows according to Clause 13.3.4:

$$V_c = \left(1 + \frac{2}{\beta_c}\right) 0,19 \lambda \phi_c \sqrt{f'_c} b_0 d \quad (4.11)$$

$$V_c = \left(\frac{\alpha_s d}{b_0} + 0,19\right) \lambda \phi_c \sqrt{f'_c} b_0 d \quad (4.12)$$

$$V_c = 0,38 \lambda \phi_c \sqrt{f'_c} b_0 d \quad (4.13a)$$

Among these, Eq.4.13a is the most critical, which can be calculated as follows.

$$V_c = 0,38(1)(1)\sqrt{30}(1008)(121) = 254 \text{ kN} \quad (4.13b)$$

where,

d = effective depth of the slab

f'_c = the compressive strength of concrete in MPa

β_c = the ratio of long side to short side of the column, concentrated load, or reaction area;

ϕ_c = resistance factor for concrete (taken as 1.0)

λ = factor to account for low-density concrete (taken as 1.0)

α_s = factor that adjusts V_c for support dimensions (taken as 1.0)

4.2.2.3. EUROCODE 2 (European Committee for Standardization, 2004)

In Eurocode 2 provision, reinforcement ratio and size effect are taken into account unlike ACI 318-11 and CSA A23.3 04. Furthermore, control perimeter b_0 is also increased as seen in Figure 4.10, and calculated in Eq.4.14.

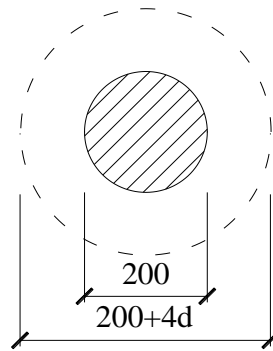


Figure 4.10. Control perimeter according to EC2 2004

$$b_0 = \pi(200 + 4(121)) = 2150 \text{ mm} \quad (4.14)$$

Punching strength is given in Clause 6.4.4 as follows.

$$V_{RC} = 0,18k(100\rho f_c)^{1/3} b_0 d \geq v_{\min} b_0 d \quad (4.15)$$

where

b_0 = control perimeter

d = effective depth of the slab

f_c = the compressive strength of concrete in MPa

ρ = flexural reinforcement ratio, $\rho \leq 0,02$

k = factor accounting for the size effect

$$k = 1 + \sqrt{\frac{200}{d}} \leq 2,0 \quad (4.16a)$$

$$v_{\min} = 0,0035k^{3/2} f_c^{1/2} \quad (4.17b)$$

which can be calculated as,

$$k = 1 + \sqrt{\frac{200}{121}} = 2,28 \therefore k = 2,0 \quad (4.16b)$$

$$v_{\min} b_0 d = 0,0035(2^{3/2})(30^{1/2})(2150)(121) = 140 \text{ kN} \quad (4.17b)$$

Reinforcement ratios for specimens can be calculated as follows.

For specimen BB100a;

$$\rho = \frac{50}{(100)(121)} = 0,0041 \quad (4.18)$$

For specimen BB150a;

$$\rho = \frac{50}{(150)(121)} = 0,0028 \quad (4.19)$$

For specimen BB100a;

$$\rho = \frac{50}{(200)(121)} = 0,0021 \quad (4.20)$$

Accordingly, punching capacities of specimens are calculated in Eq.4.21 to Eq.4.23.

For specimen BB100a;

$$V_{RC} = 0,18(2)(100.0,0041.30)^{1/3}(2150.121) = 216 \text{ kN} > 140 \text{ kN} \quad (4.21)$$

For specimen BB150a;

$$V_{RC} = 0,18(2)(100.0,0028.30)^{1/3}(2150.121) = 173 \text{ kN} > 140 \text{ kN} \quad (4.22)$$

For specimen BB200a;

$$V_{RC} = 0,18(2)(100.0,0021.30)^{1/3}(2150.121) = 173 \text{ kN} > 140 \text{ kN} \quad (4.23)$$

4.2.2.4. TS 500 (Turkish Standards Institution, 2003)

In Turkish standards, formula of punching strength is slightly different than other code provisions. Control parameter and effective depth of slab remains same whereas design tensile strength of concrete is used in the formulation. Punching strength is given as in Eq. 4.24 in Clause 8.3.

$$V_{pr} = f_{ctd} U_p d \quad (4.24)$$

$$f_{ctk} = 0,35\sqrt{f_{ck}} \quad (4.25)$$

where;

f_{ctd} = design tensile strength of concrete in MPa

U_p = control perimeter

f_{ck} = characteristic compressive strength of concrete in MPa

d = effective depth of the slab

Accordingly, the punching capacity of specimens can be calculated as:

$$V_{pr} = 0,35\sqrt{f_{ck}}(1008).(121) = 232 \text{ kN} \quad (4.26)$$

Static load-displacement responses of three specimens are given in Figure 4.12. As seen from the responses, BB100a displayed a brittle failure compared to other specimens, whereas BB150a and BB200a failed in a more ductile manner. Capacities calculated according to code provisions and yield line theory is tabulated in Table 4.1 along with the test results. For BB100a, calculated flexural capacity is very close to the punching capacities calculated using different code provisions. Hence, a flexural-punching failure would be expected. Test result is also close to the calculated capacities, supporting the observations from the test in which punching failure came after extensive flexural cracking. For specimens BB150a and BB200a, calculated flexural capacities are smaller than the punching capacities calculated by ACI 318-11, CSA A23.3-04 and TS 500, where as they are closer to EC2 2004. It should be noted codes other than EC2 2004 do not consider the reinforcement ratio. Test results for these specimens are in the same range with the flexural capacities and punching capacity calculated by EC2 2004. Extensive ductile deformations followed by a final punching failure observed in these tests are in line with the calculations. It is observed that the punching capacities as calculated by codes except EC2 2004 are overestimated since they do not consider the effect of reinforcement ratios. It is likely that extensive deformations in the loading region cause a reduction in the punching strength, which caused the final failure in these specimens. EC2 2004 somewhat takes this effect into account by reducing the punching capacity with the reduced reinforcement ratios.

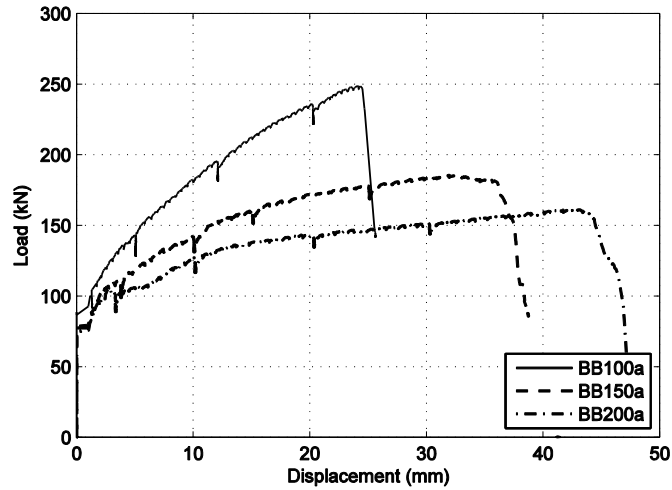


Figure 4.11. Static load-displacement behavior of test specimens

Table 4.1. Comparison of results for static tests

Specimen Name	Punching Capacity (kN)				Flexural Capacity (kN)	Test Results (kN)
	ACI 318-11	CSA A23.3-04	EC2 2004	TS 500		
BB100a	220	254	216	232	230	248
BB150a	220	254	173	232	169	184
BB200a	220	254	173	232	133	161

4.3. Impact Tests Observations

In this section, visual observations from the impact tests such as crack profiles formed by varied drop weights and final states of the specimen after tests are presented.

4.3.1. BB100b Tests

As indicated in previous chapter, loading program started with the BB100b specimen. This specimen was subjected to impact loads three times by different drop weights. First impact, BB100b-1, was performed by 210 kg weight as seen in Figure 4.12a. After carrying out the first impact test, it is observed that increasing the drop weight would be more effective in order to obtain the global behavior of specimens.

Dropping 210 kg weight caused hardly visible hairline cracks at the bottom surface and did not generate mass penetration into the slab. Therefore, second impact test was applied after load has increased to 320 kg by welding additional steel plates.

Following the first impact, 320 kg of mass was dropped on BB100b specimen. Inherited hairline cracks from the first impact were widened and extended. In addition to these cracks, new cracks on the diagonals and a circular crack on the bottom surface developed. In addition, partial scabbing was observed in circular crack region at the bottom surface (Figure 4.12b).

For the last testing of BB100b, 320 kg of drop mass was used on the specimen. Residual cracks from previous tests were widened and few newer cracks developed. As clearly seen in Figure 4.12c, significant scabbing was observed around the location of circular crack, exposing reinforcing bars after impact. Moreover, mass penetration occurred locally on the top surface.

4.3.2. BB150b Test

BB150b specimen was tested once by impact of 320 kg of mass. As observed in previous tests, cracks developed on diagonals and substantial circular crack profile was observed as a sign of punching failure. Additionally, scabbing occurred partially around circular crack as can be seen in Figure 4.13. Penetration of mass was also observed on the top surface.

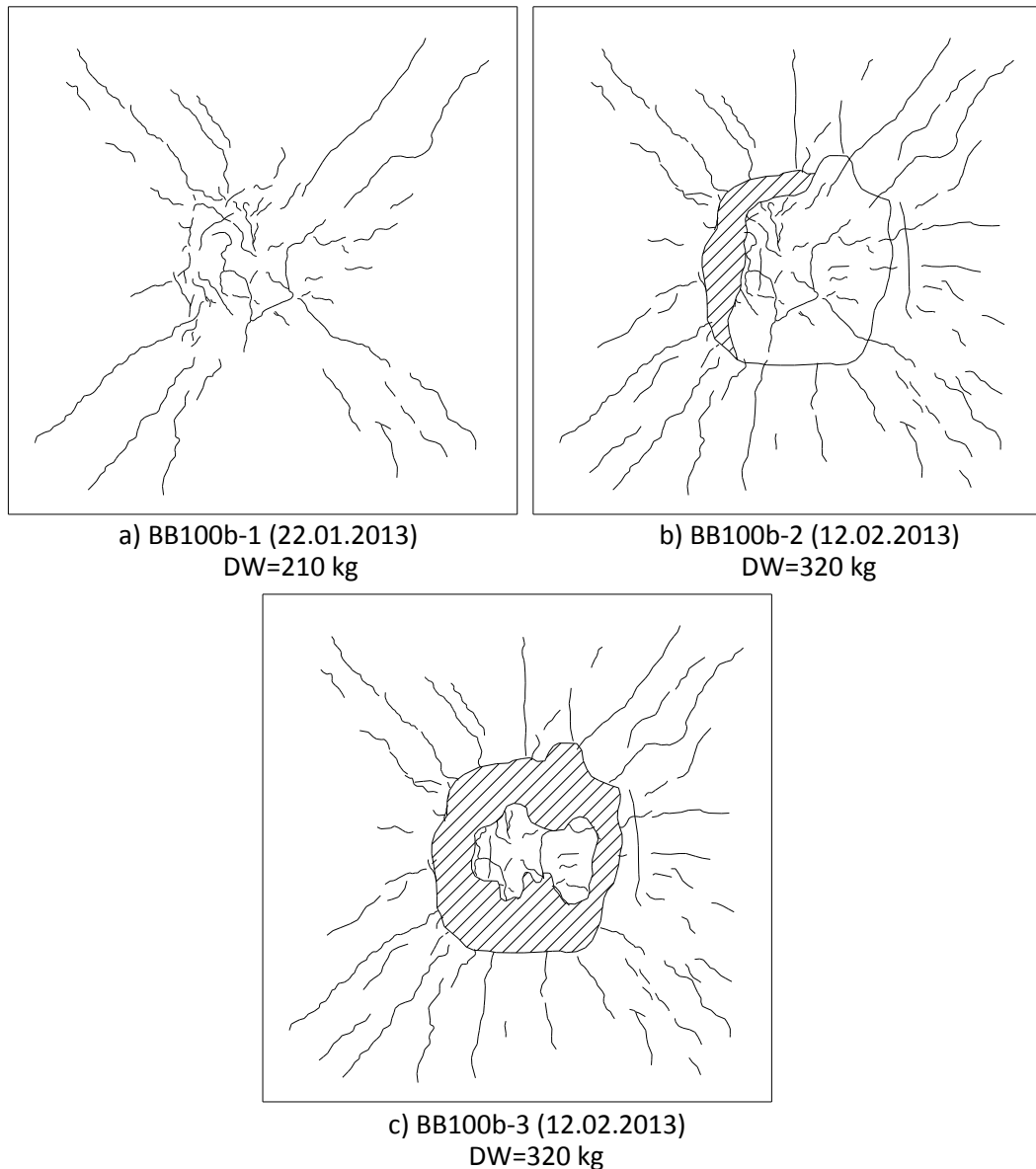
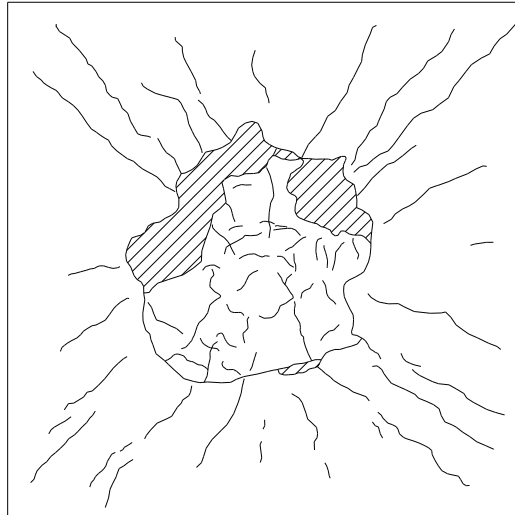


Figure 4.12. Impact crack profiles of bottom surface for BB100b

4.3.3. BB200b Tests

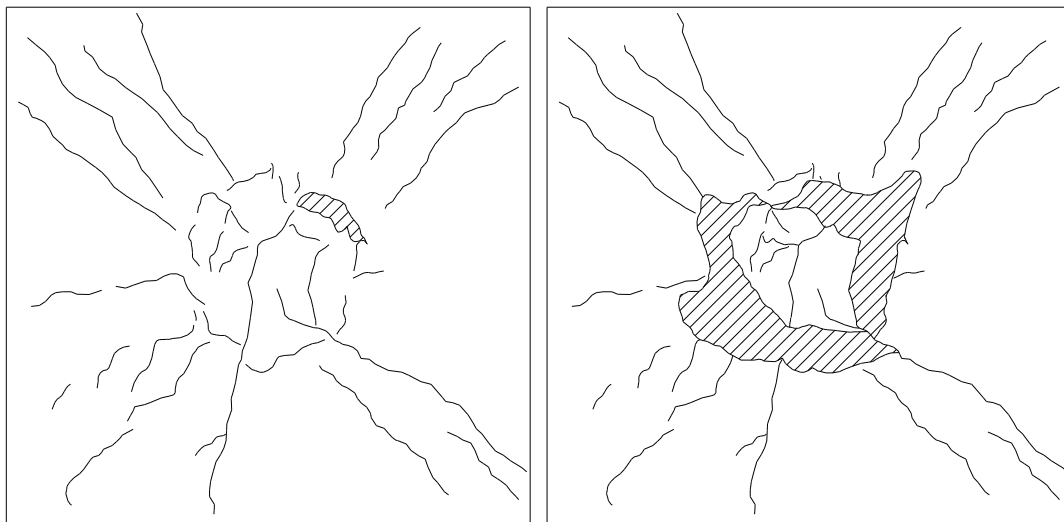
The last specimen of impact tests was subjected to impact loads twice with 210 kg mass of drop weight. In first impact, not only expected diagonal cracks occurred, but also circular cracking and slight scabbing on the bottom surface were observed (Figure 4.14a).

Number of cracks did not increase after second impact for this specimen. Residual cracks were widened significantly and excessive scabbing of concrete from the bottom surface was observed.



BB150b (18.04.2013)
DW=320 kg

Figure 4.13. Impact crack profile of bottom surface for BB150b



a)BB200b-1 Impact (30.04.2013)
W=210 kg

b)BB200b-2 Impact (30.04.2013)
W=210 kg

Figure 4.14. Impact crack profile of bottom surface for BB200b

4.4. Discussion of Impact Tests

This section is comprised of digital data analysis, discussions on displacements and deformations, reactions and loads, and dynamic equilibrium. Interpretations of collected data and accompanying calculations are illustrated.

4.4.1. Digital Data Analysis

As mentioned in previous chapter, data presented herein for both tests were collected with a high speed digital data acquisition system at a rate of 250 kilosample/second/channel. According to Nyquist's sampling theorem, sampling frequency should be greater than twice the maximum frequency response (Marks II 1991). To ensure collected and recorded digital data, selected power spectrums are examined in order to reveal the dominant frequencies of signals.

Impact or shock events are developed in extremely short time interval as clearly observed throughout the impact tests. The entire impact data captured by high speed data acquisition system were very large in volume and contained redundant parts that would cause unnecessary time consumption for data processing. Thus, whole data for each impact were scanned and clipped into manageable size which started from just prior to impact and ended until the displacements, loads and accelerations were stagnant. Data processing were performed with the help of MATLAB program.

The displacement data captured from the RLPTs have been analyzed with regard to their frequencies in order to determine dominant frequencies of digital signals. A simple code using the FFT (Fast Fourier Transform) method was written in MATLAB to develop the power spectrums of displacement data measurements. According to results of the developed spectrum (see Figure 4.15b), sampling rate of the data acquisition system is adequate enough to capture all significant frequencies from RLPTs, evidenced by the minimal frequency content larger than 0.4 kHz. This developed power spectrums had played a key role for filtering the measured signals which are used in derivation of accelerations of the slab. Filtering of displacement response signals were performed in MATLAB as well, using '*filtfilt*' command. The '*filtfilt*' command provides the designing of a low-pass filter with predefined cut-off frequency. The '*filtfilt*' filtering is advantageous over the other filtering methods due to its ability to avoid any phase distortion. For the displacement response signals, the low-pass filters using '*filtfilt*' command were designed as fifth-order Butterworth with 0.05 cut-off frequency. As clearly seen in Figure 4.16, zero-phase lag of the signal is provided and peak value of the measurement is not altered by this filtering method. Besides, desired smooth curve of the filtered data used in derivation of the accelerations of slab is obtained as well.

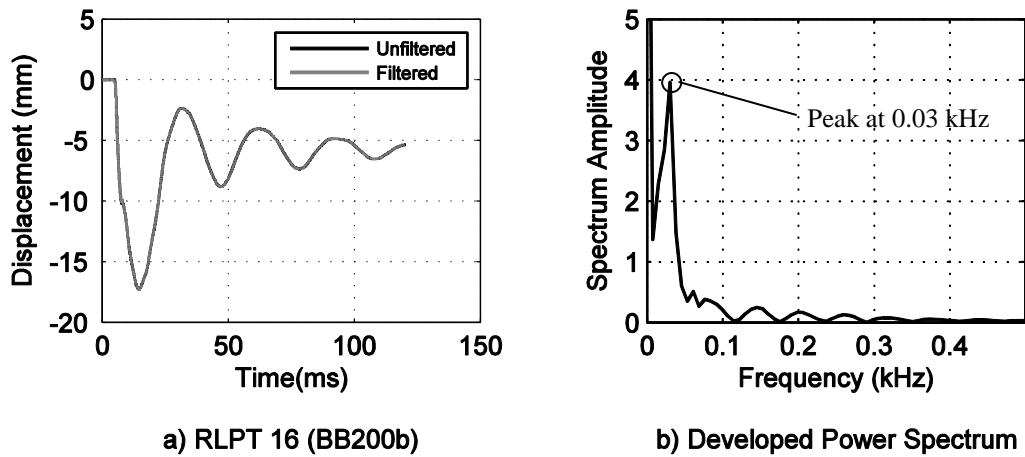


Figure 4.15. Midpoint displacements for BB200b-1 (P16)

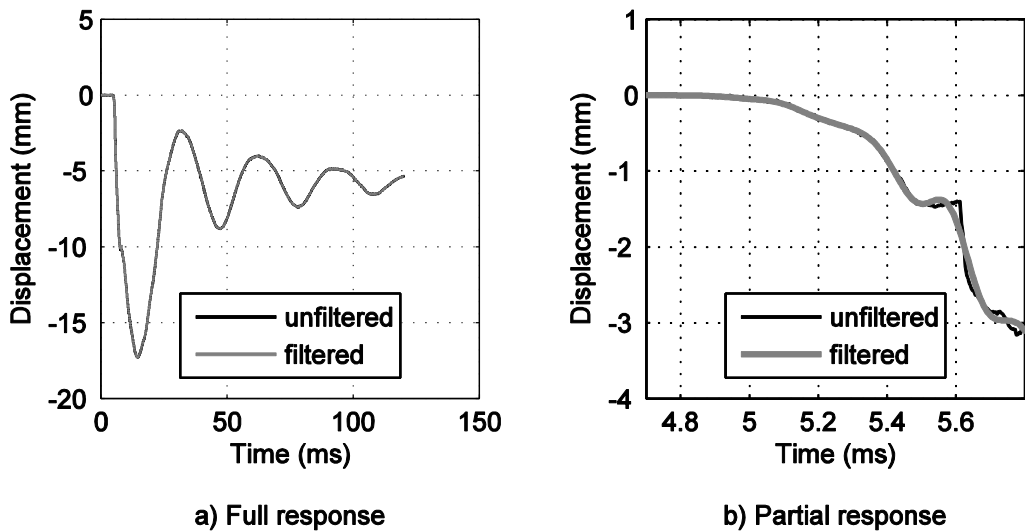


Figure 4.16. Midpoint displacement response for BB200b-1 (P16)

Acceleration signals of tests collected from the accelerometers- two of them on drop weights and four of them on slabs at the same location with RLPTs- were also filtered. To calculate inertial forces for the whole mass of slabs, only four accelerometers were not adequate and accurate enough. Therefore, accelerations were tried to be derived from displacement responses obtained the RLPTs. With the purpose of obtaining accelerations derived from displacement, some methods such as second-order central, fourth-order central, forward and backward methods were examined and second-order method was decided to be used. After selecting the method, combinations of filtering steps were investigated as well. Filtering steps started from the measured

displacement response and filtered in each step such as a filtration of velocity and continued with calculation of acceleration from filtered velocity and ended up with final filtration of accelerations. After providing smooth curves for the displacements, derived velocity responses were filtered by MATLAB using the *'filtfilt'* command designed as fifth-order Butterworth with 0.001 cut-off frequencies.

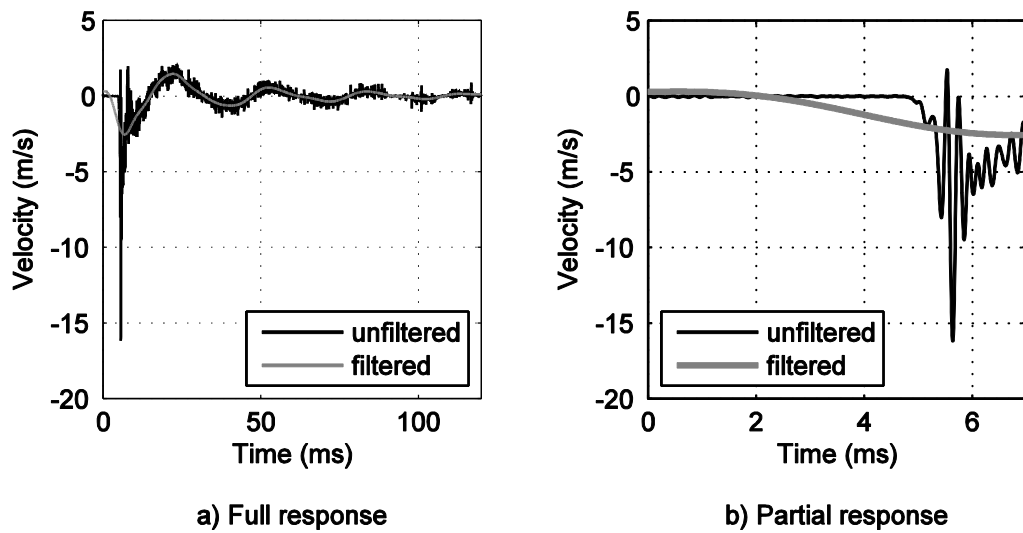


Figure 4.17. Derived velocity response for BB200b-1 at P16 location

With the filtration of velocity response, accelerations derived from displacements were obtained Figure 4.18.

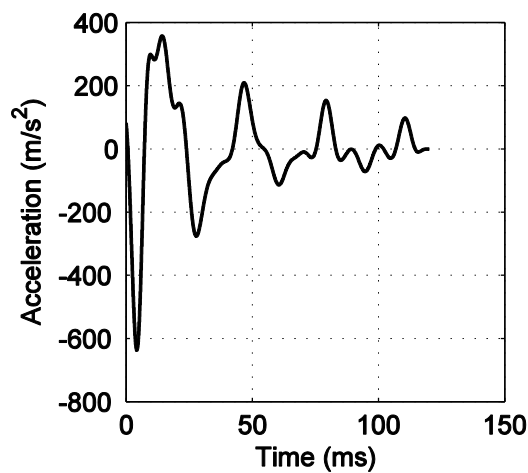


Figure 4.18. Derived acceleration response for BB200b-1 at P16 location

For the accelerations measured from the accelerometer both on slabs and drop-weights, parameters of designed low-pass filter had same cut-off frequency and number of order with accelerations derived from displacement (see Figure 4.19).

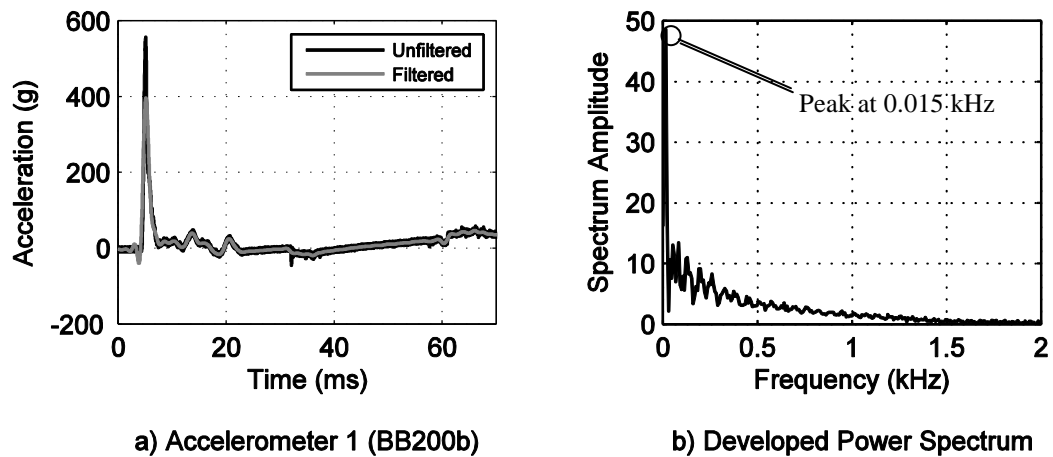


Figure 4.19. Drop-weight (210 kg) accelerations for BB200b

For the responses of measured accelerations on slab and measured displacements at the same locations, Figure 4.20 shows that increasing in measured displacement is to start when the measured accelerations has reached its peak value. This lag between displacement and accelerometer at the same location causes the same effect in dynamic equilibrium calculations that will display in section 4.4.5.

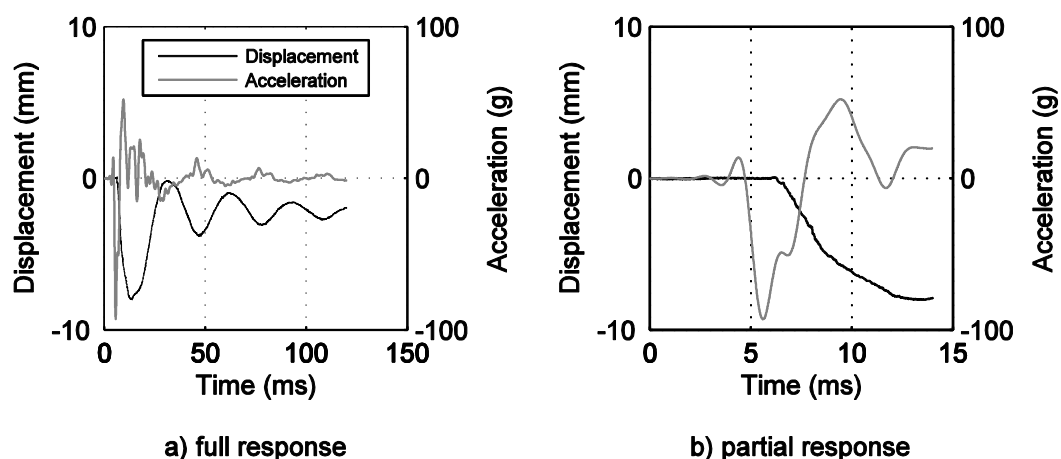


Figure 4.20. Acceleration and displacement response for BB150b at the P8 location

4.4.2. Displacements and Deformations

The midpoint displacement responses and displaced shapes of middle axes and a quadrant of slabs at different stages were examined and represented in this section.

4.4.2.1. Midpoint Displacement- Time History

As stated in previous chapter, some of midpoint displacements were not captured due to detachment of their connections from the slabs. Throughout the impact tests, only three midpoint displacements were captured for the last three, BB150, BB200-1 and BB200-2, impact tests (Figure 4.21). Due to the punching behavior in impact region, BB150b specimen had more residual displacement compared to BB200b-1 impact event. In other words, BB200b specimen for the first impact showed more elastic behavior than BB150b specimen under impact of 320 kg mass. However, preexisted punching cone could not resist the second impact of 210 kg mass as expected, and maximum residual displacement of midpoints was measured among these tests.

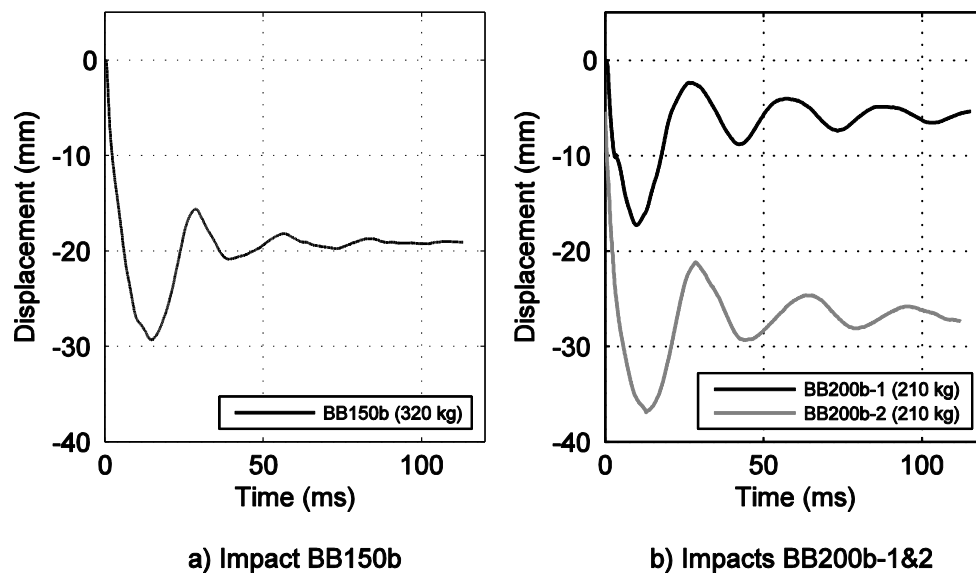


Figure 4.21. Midpoint displacement-time histories (P16)

4.4.2.2. Displaced Shapes

For the purpose of obtaining displacement profiles under impact loads, displacement transducers- 24 RLPTs for impact tests- were located effectively on bottom surface of each specimen as explained in previous chapter. In this section, displacement measurements were discussed in terms of displaced profiles for a middle axis at the times of maximum, minimum and residual displacements. A comparative approach for impact tests and static tests at the same midpoint deflections are provided. Three-dimensional displacement response illustrations for the quadrants of specimens at different times during the impacts are also presented.

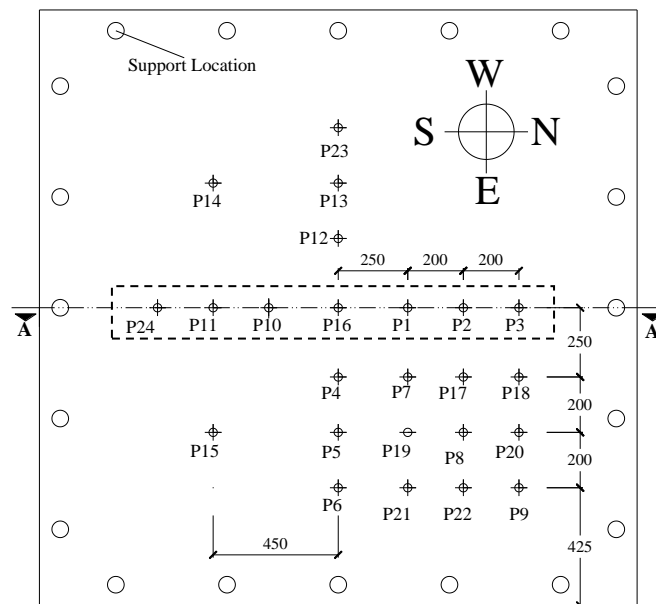
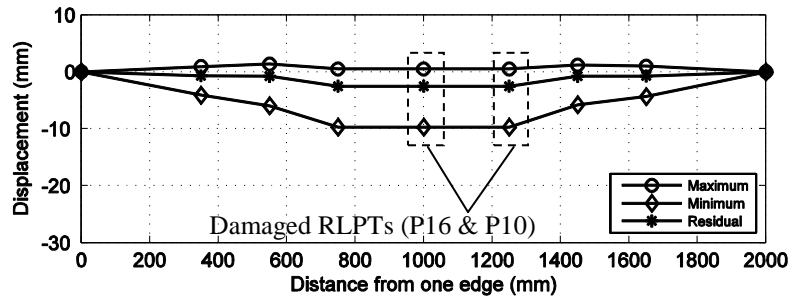


Figure 4.22. RLPT locations for displaced shapes

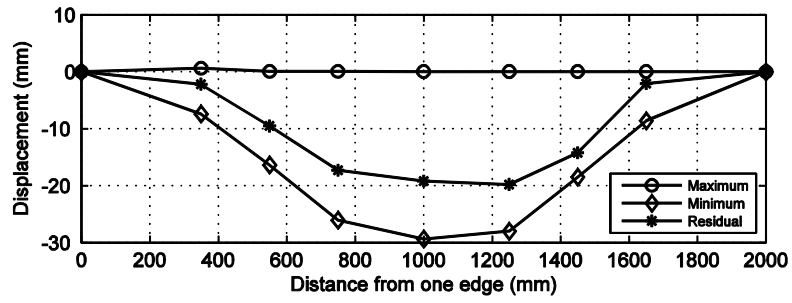
For section A-A (Figure 4.22), only two RLPTs were lost for BB100b-1 whereas none of RLPTs were detached for the BB150b and BB200b-1 tests. In course of testing BB100b-1, midpoint RLPT (P16) and its adjacent RLPT (P10) were damaged (see Figure 4.23a). To provide continuity for presentation of profile, RLPT 1, which is adjacent to RLPT 16, was taken into account instead of damaged RLPTs.

The displaced shape plots of specimens were investigated at their minimum, maximum and residual displacement profiles under impact loads. Note that BB100b exhibited close to elastic behavior under 210 kg mass impact as clearly seen in Figure

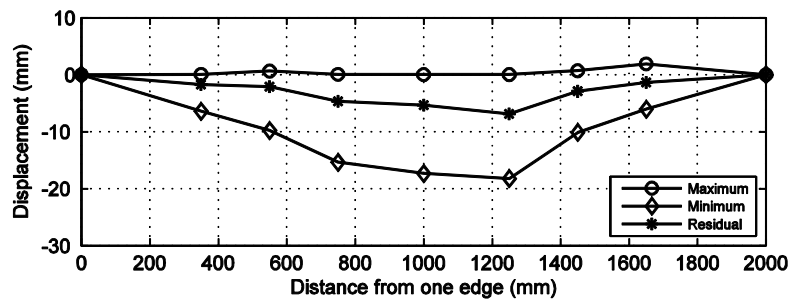
4.23a. Signs of punching behavior were not observed according to its maximum and residual displaced shapes. However, punching formation for the specimen B150b was obviously obtained under 320 kg drop weight (Figure 4.23b). The impact load caused extensive and residual deformations in punching zone. Similar to this test, under impact of 210 kg mass, BB200b exhibited similar profile as well (Figure 4.23c). For all three impact events, RLPTs, which are close to supports, measured positive displacements at the impact instant that can be explained by nature of the impact event. For instance, as the portion of the specimen under impact point starts to deflect downwards, the other portions cannot follow immediately due to their inertia. This lag in response creates upwards curvature. For better representation of this lag, displacement profiles of the specimen tested under impact loads and static loads were compared at the same midpoint deflections. Since the deflection of specimens for static tests were higher than impact cases, maximum midpoint deflections of impact tests were matched up with static midpoint deflection. Due to the loss of the RLPTs 10 and 16 for BB100b-1 specimen, adjacent RLPT (1) measurements were matched up instead of midpoint deflection. Comparisons of the displaced shapes were investigated at four steps in order to see the deflection differences between static tests and impact tests. As obviously seen in Figure 4.24, some portions cannot pursue the portions in impact region as in static loading. 3-D plots of displacement profiles for quadrants were displayed as well in Figure 4.25.



a) BB100b-1 Deformations

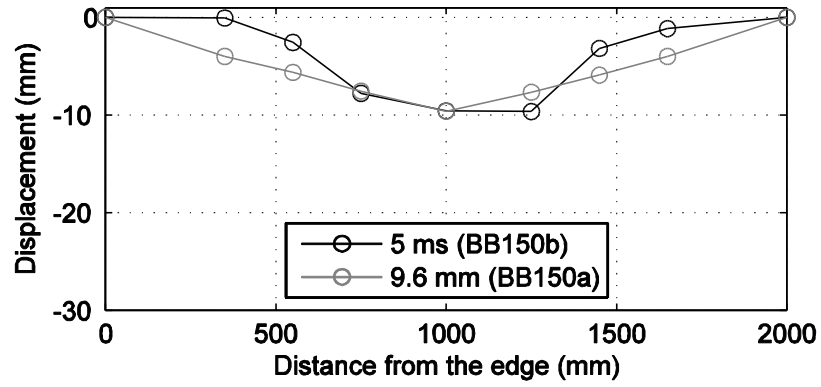


b) BB150b Deformations

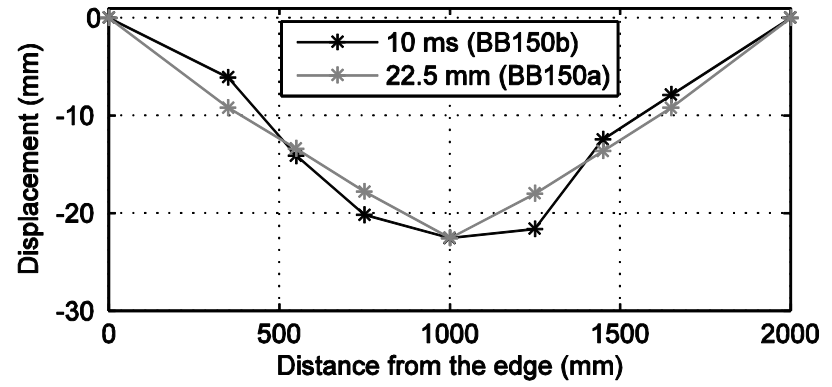


c) BB200b-1 Deformations

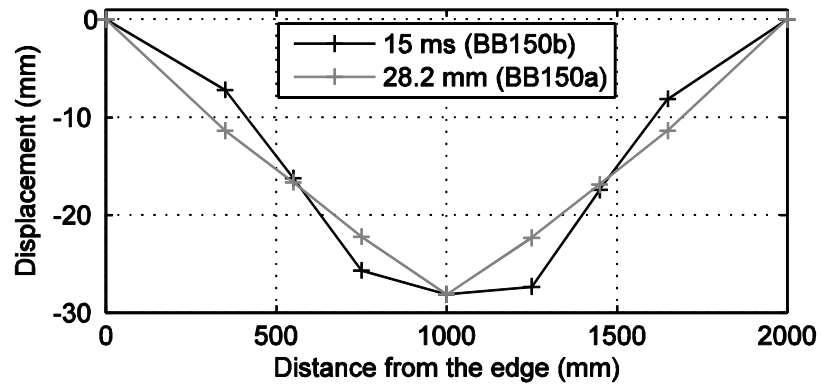
Figure 4.23. Maximum, minimum and residual deformations for BB100b-1, BB150b and BB200b-1, respectively



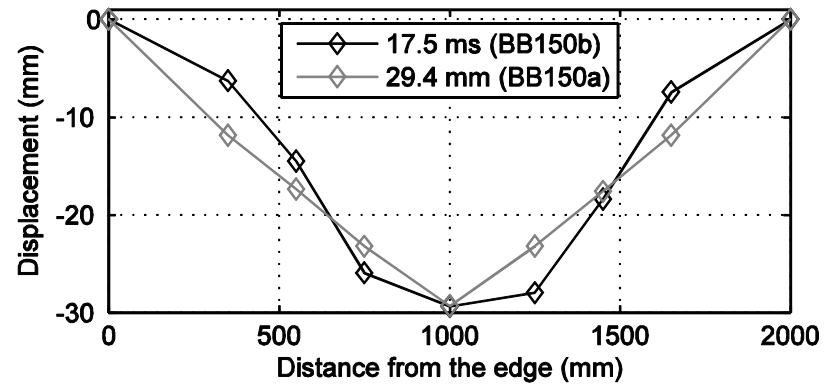
a)



b)



c)



d)

Figure 4.24. Displacement profiles of BB150a and BB150b for the same midpoint displacements

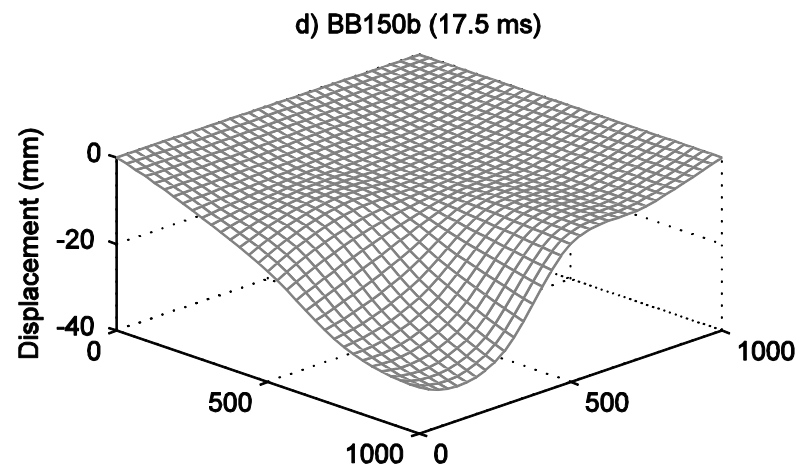
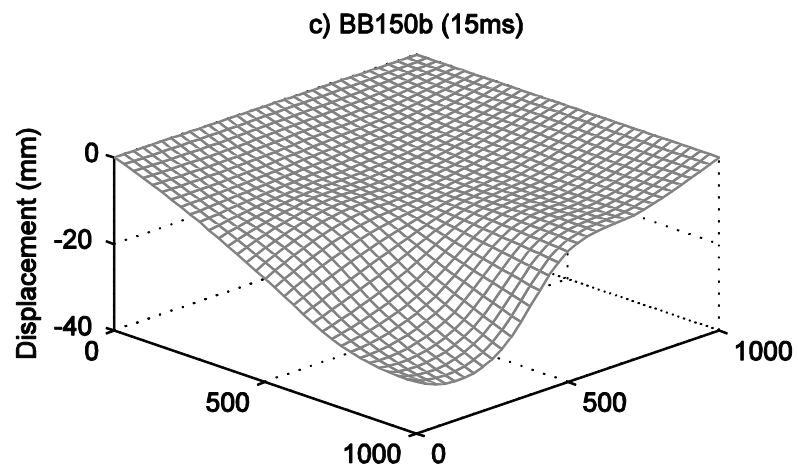
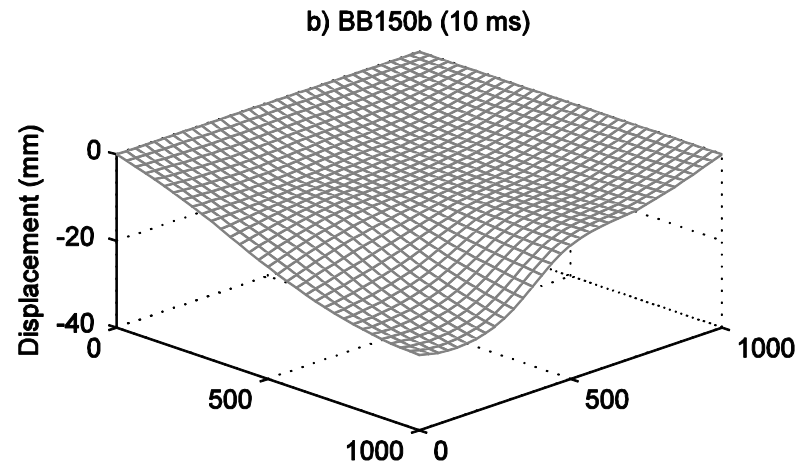
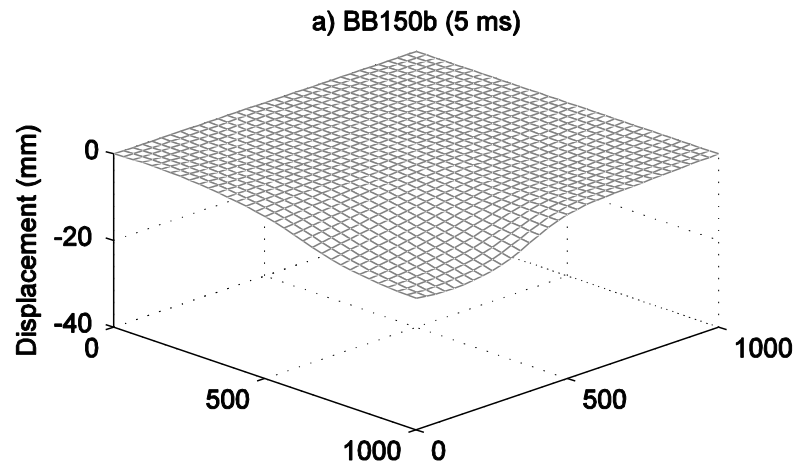


Figure 4.25. 3-D plots of displacement profiles for quadrants of BB150b

4.4.2.3. Strain Gauge Measurements

Strains of reinforcing bars were measured at 12 locations for each specimen as explained in section 3.3.2. No reliable data were obtained from these gauges in static tests due to excessive noise. In impact tests, noise problem was solved to an extent and data were collected. As measured in impact tests, slabs were deflected in both upward and downward directions due to the nature of impact event. Therefore, strain measurements were expected to be in both tension and compression. However, most of the strain gauge measurements were positive indicating tensile forces. Throughout the impact tests, strain gauges at bottom reinforcement measured larger peaks and residual strains compared to strain gauges located on top.

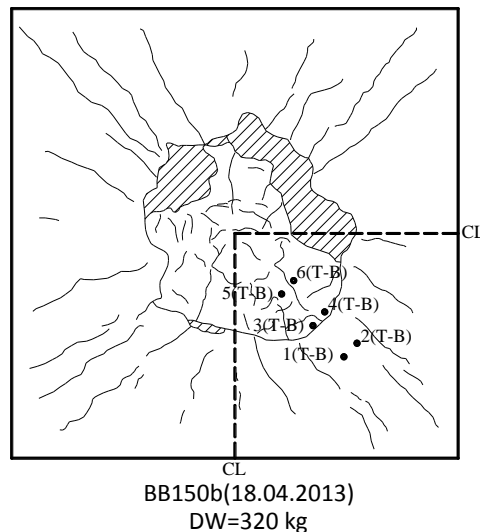


Figure 4.26. Crack profile and strain gauge locations for BB150b specimen

As an example, according to the strain gauge 3 for BB150b (Figure 4.26) , strain on the bottom reinforcement was measured negative at the instant of impact, whereas strain at top reinforcement was positive (Figure 4.27). It may be interpreted that slab is starting to deflect upwards at the instant of impact which causes compressive forces for bottom reinforcing bar, but top reinforcement was subjected to tensile force due to the impact

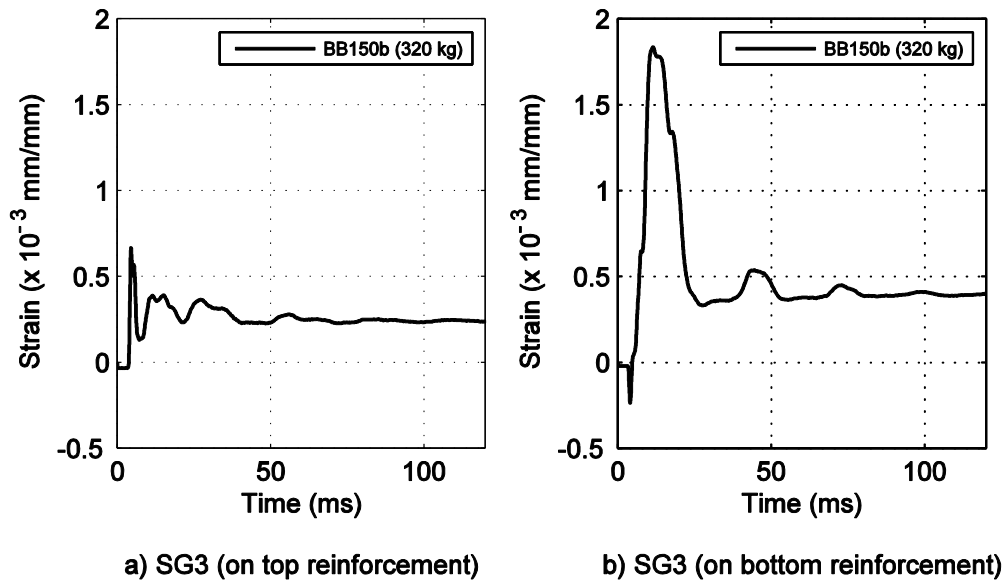


Figure 4.27. Strain gauge 3 measurements for BB150b

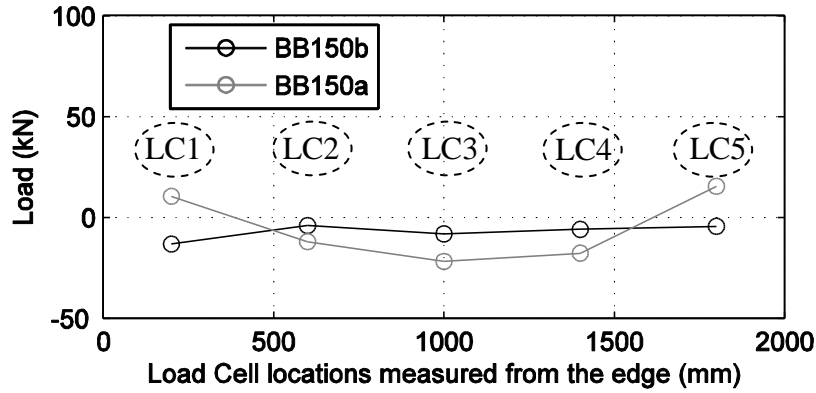
4.4.3. Reactions and Loads

Examined support reactions for both static and impact tests, compared reaction forces for the same midpoint displacements and total reaction forces are represented in this section.

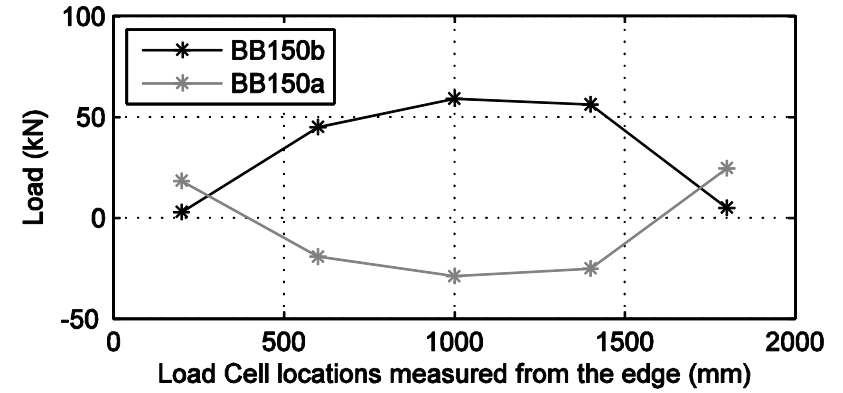
4.4.3.1. Support Reactions

Reactions measured in both tests were examined and compared along one edge from the load cell 1 to 5. In Figure 4.28, comparisons between support reactions for static and impact tests were displayed. Note that in static tests, load was applied from bottom whereas impact load was applied from top. Directions for measured static reactions were reversed in these discussions to provide a better comparison. Similar to displaced shape comparisons, measured reactions were examined for the same midpoint displacements of static and impact test. Dissimilarity in the distribution of forces for both tests can be easily observed at different midpoint displacements. In all displacement steps, great majority of reaction forces developed at the middle supports for both tests, whereas direction of reaction forces are opposite to each other. For the impact case, support reactions in the corners measured compression loads; the midpoint support was subjected to tensile load (see Figure 4.29). On the contrary, in static cases

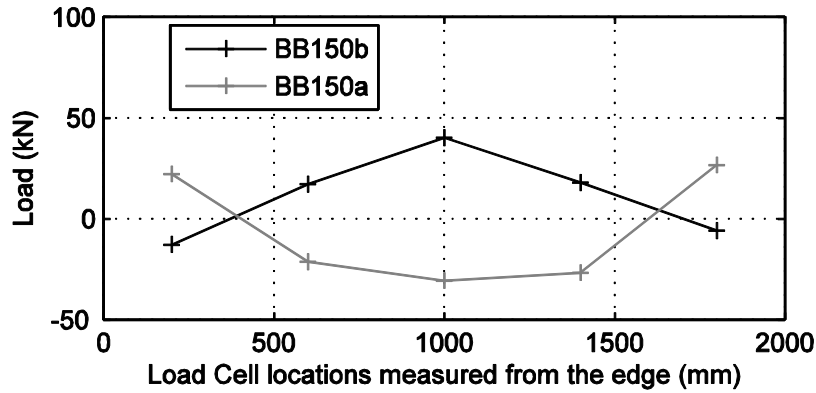
midpoint supports measured compressive loads, whereas supports at the corners were subjected to tensile loads as it can be seen in Figure 4.30. These differences for the support reactions in the tests can be explained as a result of the displacement profile formation as mentioned in previous section. Creating upward deflection due to lag in response between portions of slab in impact case causes tensile loads at the supports. As clearly seen in Figure 4.31, majority of support reactions, approximately twice as its adjacent supports, were carried by the middle support. For the first impact of specimens, total support reactions were represented in the Figure 4.32. Note that BB100b, BB150b and BB200b specimens were subjected to 210, 320 and 210 kg of mass, respectively. Despite impact of varied masses, total support reactions for the first impacts of three specimens reached approximately same peak values. Figure 4.33 and Figure 4.34 show the total reaction forces for all impact tests of specimens BB100b and BB200b, respectively. All peak reactions for impact tests were represented in Table 4.2. Peak support reactions decreased after first impact for specimen BB200b as expected. But this was not observed in BB100b-2 and BB100b-3 tests. Increasing the drop weight caused the pre-existing punching cone separate from the rest of the specimen, and the behavior of the structure under impact load started to turn from global to local. However, closely spaced reinforcement still provided integrity of the damaged slab under impact.



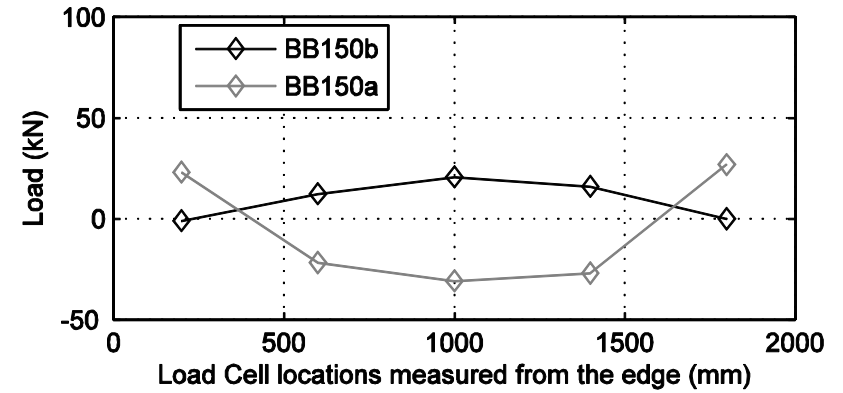
a) 5 ms (BB150b) - 9.6 mm (BB150a)



b) 10 ms (BB150b) - 22.5 mm (BB150a)

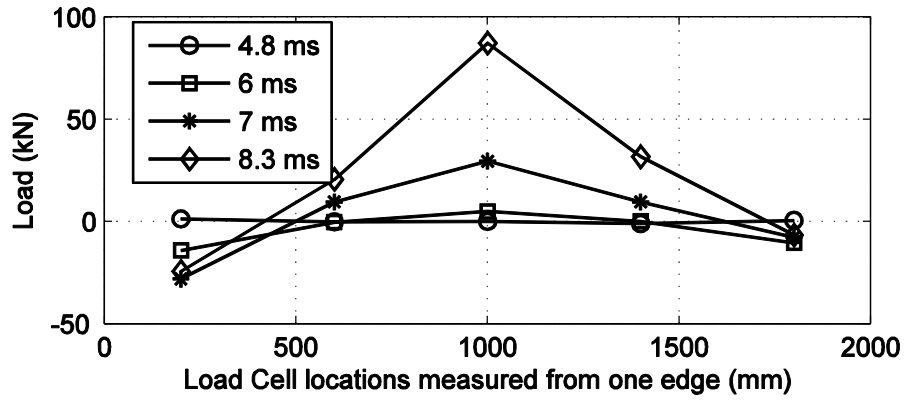


c) 15 ms (BB150b) - 28.2 mm (BB150a)

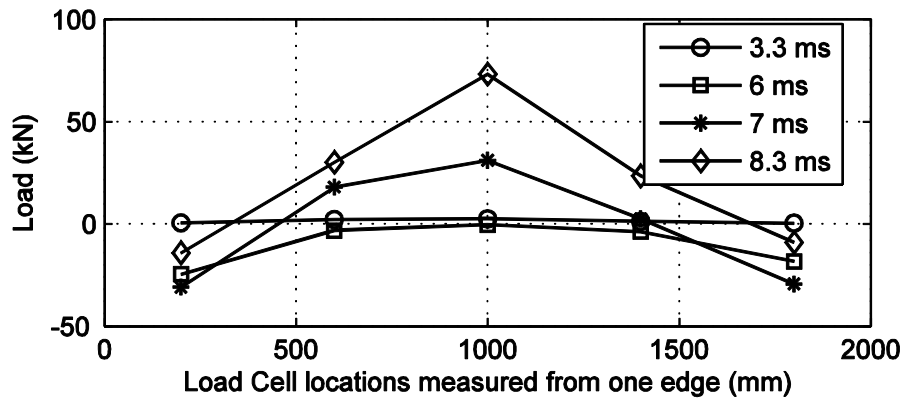


d) 17.5 ms (BB150b) - 29.4 mm (BB150a)

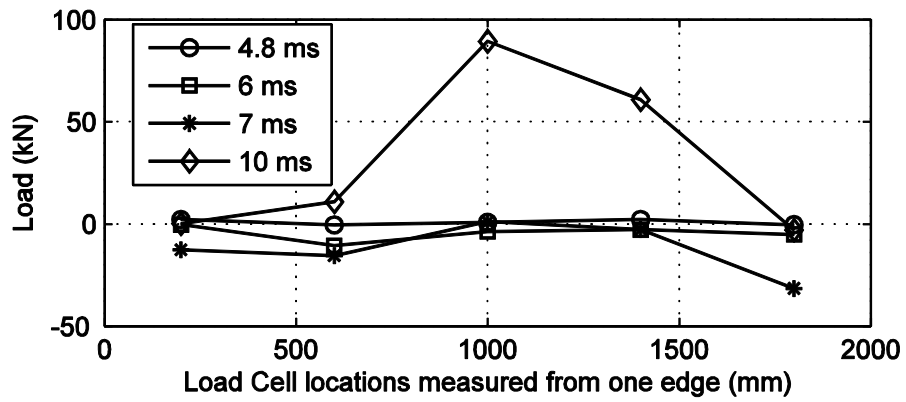
Figure 4.28. Load cell measurement profiles of BB150a and BB150b-1 for the same midpoint displacements



a) BB100b-1

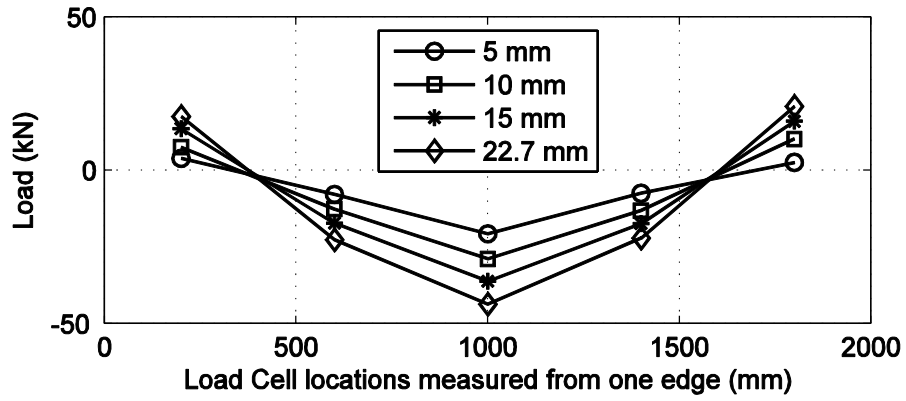


b) BB150b

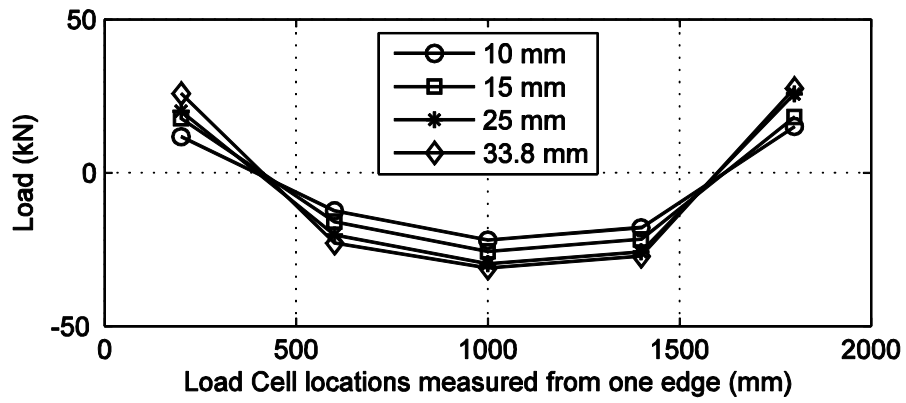


c) BB200b-1

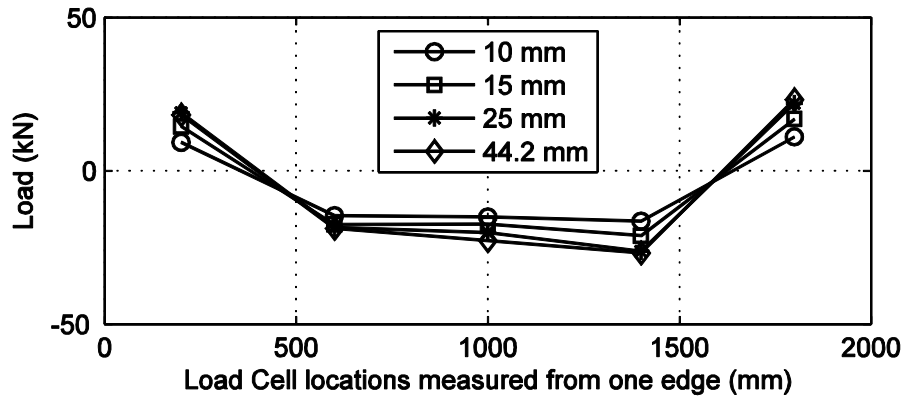
Figure 4.29. Load cell measurement profiles of impact test at different time steps



a) BB100a



b) BB150a



c) BB200a

Figure 4.30. Load cell measurement profiles of static test for different midpoint displacements

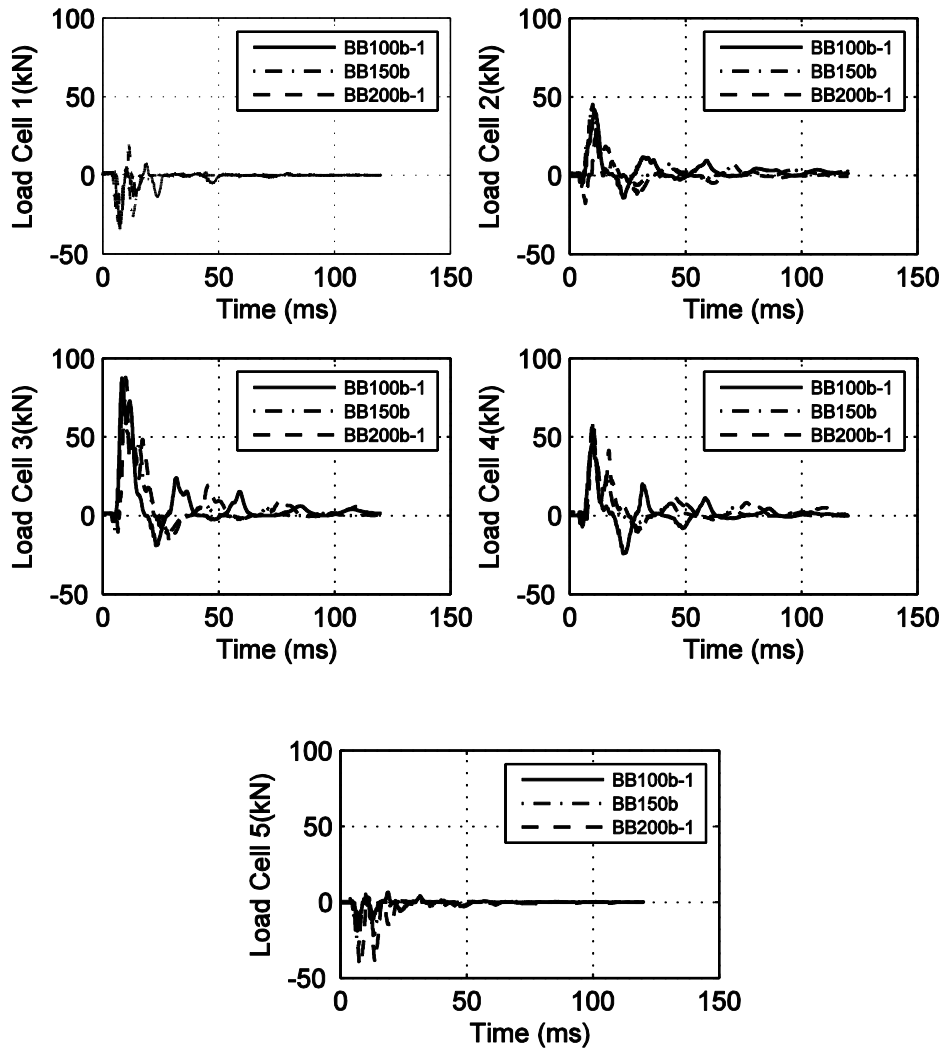


Figure 4.31. Reaction-time histories along the one edge for impact tests

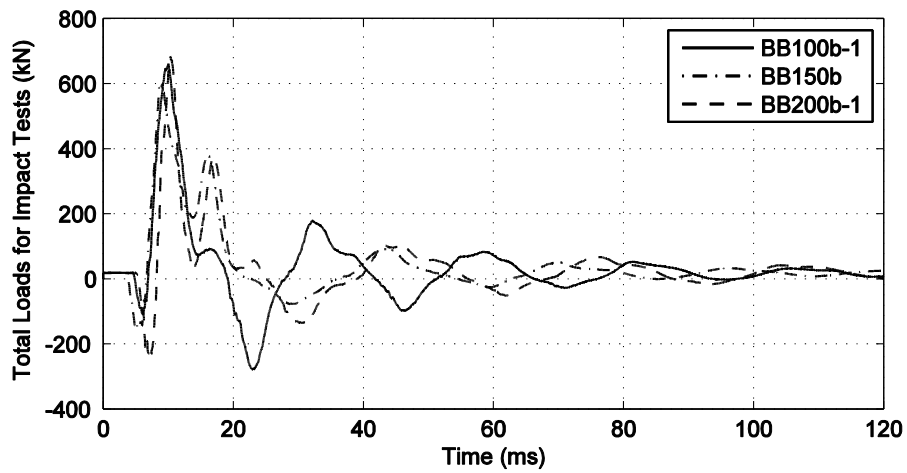


Figure 4.32. Total reaction force- time histories for impact tests

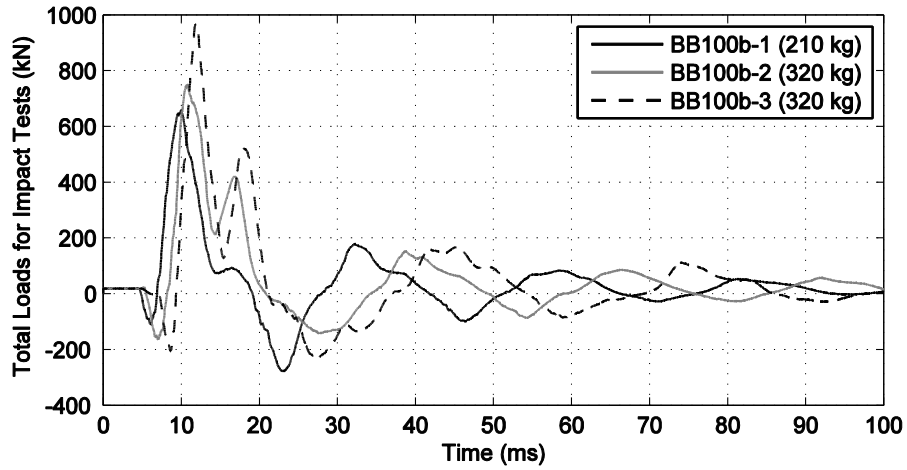


Figure 4.33. Total reaction force- time histories for specimen BB100b

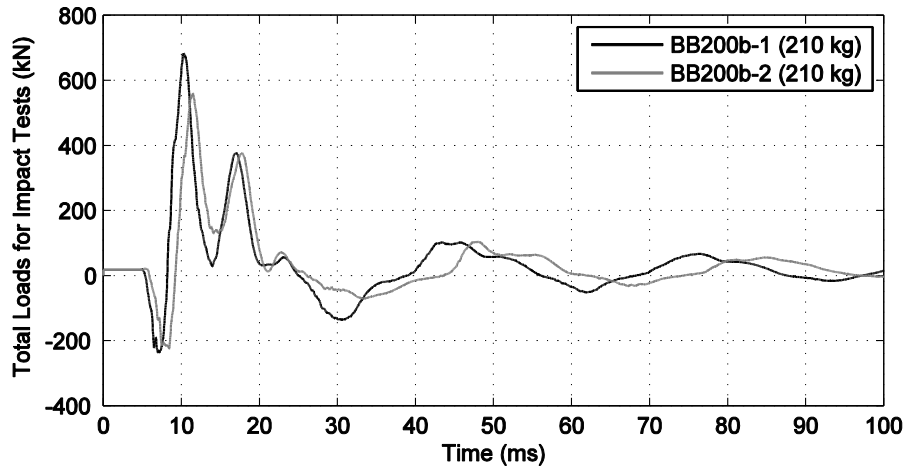


Figure 4.34. Total reaction forces- time histories for specimen BB200b

Table 4.2. Peak support reactions

	<i>BB100b</i>			<i>BB150b</i>	<i>BB200b</i>	
	<i>Impact #1</i> (210 kg)	<i>Impact#2</i> (320 kg)	<i>Impact#3</i> (320 kg)	<i>Impact #1</i> (320 kg)	<i>Impact #1</i> (210 kg)	<i>Impact #2</i> (210 kg)
<i>Total Peak Reaction (kN)</i>	661	750	971	599	683	561

Impact force-time histories were calculated from multiplying the accelerations on the drop weights with their masses. Throughout the impact tests, two accelerometers

were used to determine the accelerations of drop weights as mentioned before. In testing of BB150b, both measured accelerations were unreasonable as represented in Figure 4.35. Therefore, only impact forces for BB100b-1 and BB200b-1 tests can be displayed as in Figure 4.36. Deficiency in BB150b drop weight accelerations avoids the determination of impulses as well. Impulse-time histories of specimens with the exception of BB150b were presented in Figure 4.37. Note that impulses were determined for the first 10 milliseconds where the drop weight accelerations started to decay.

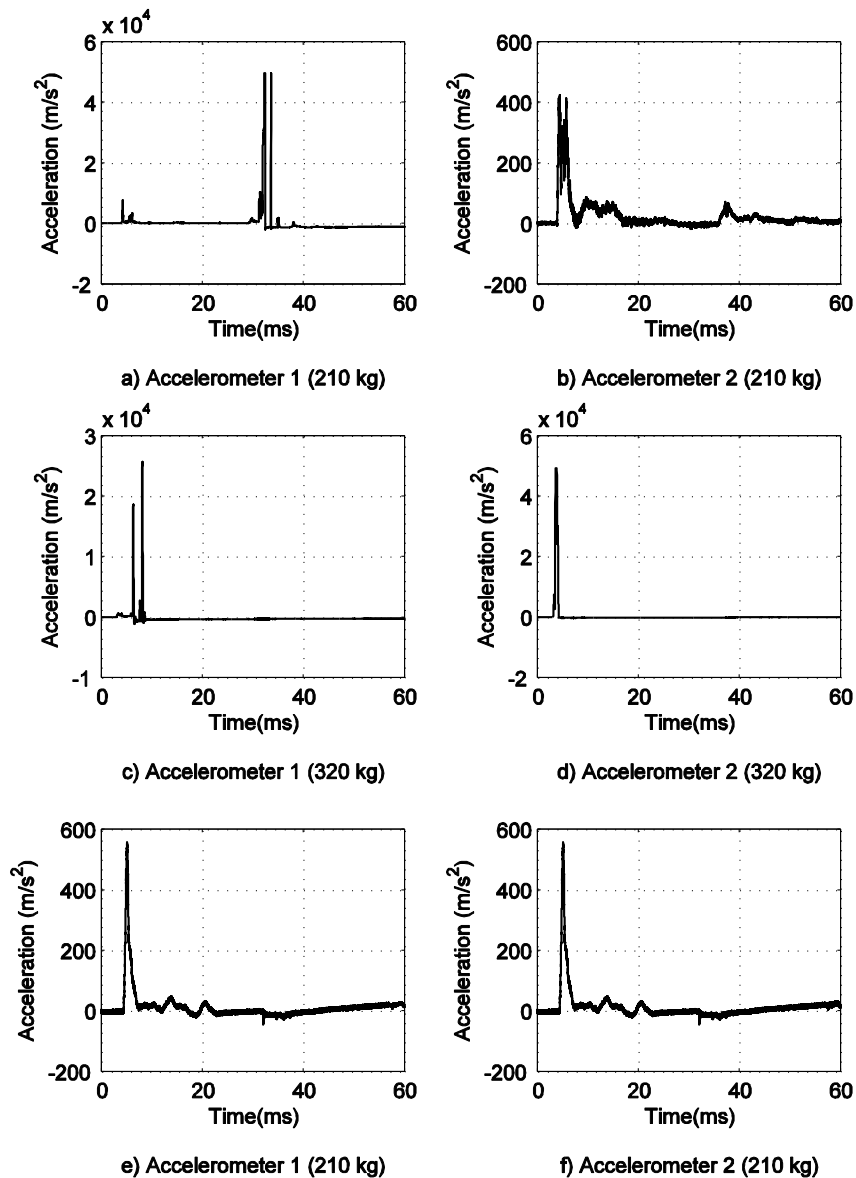
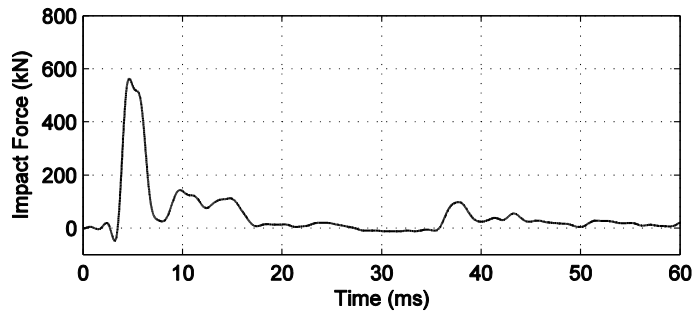
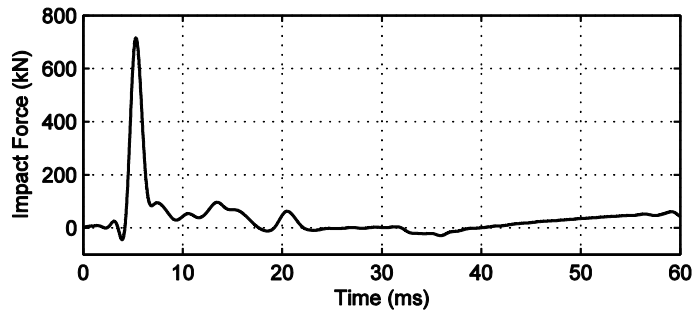


Figure 4.35. Drop-weight accelerometers for BB100b-1, BB150b and BB200b-1, respectively

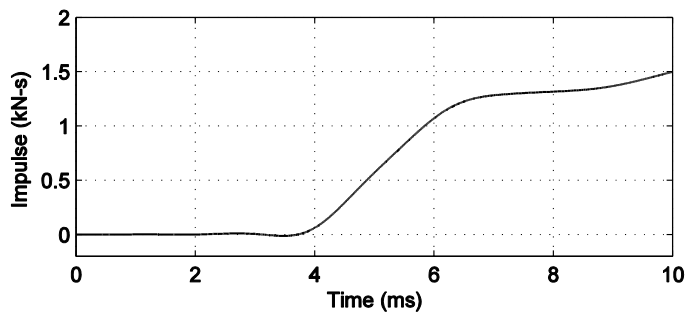


a) BB100b-1

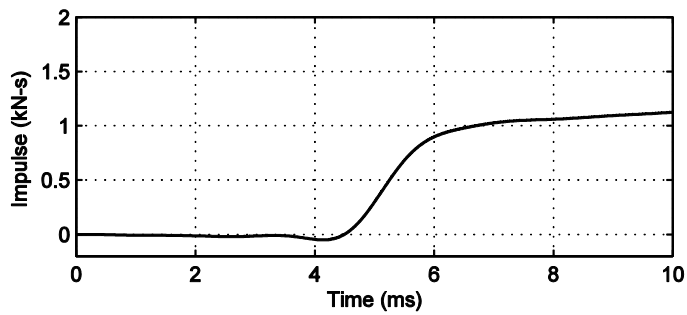


b) BB200b-1

Figure 4.36. Impact force- time histories for BB100b-1 and BB200b-1



a) BB100b-1



b) BB200b-1

Figure 4.37. Impulse- time histories for BB100b-1 and BB200b-1

4.4.4. Dynamic Equilibrium

When a time dependent force is applied to a mass, it is resisted by inertia forces, equal in magnitude to mass times acceleration, and support reactions, ignoring damping forces. With the purpose of determination of inertial forces for slabs, a quadrant of slabs were densely instrumented with 16 RLPTs (see Figure 4.22), which were used to derive accelerations from displacements. To calculate inertial forces, each slab was divided into 64 four-node quadrilateral elements. In these elements, each corner corresponded to an RLPT location. Accelerations for each corner node were calculated by taking the derivative of the displacements twice and linear variation of accelerations between the corners was assumed. Appropriate filters were applied to displacement data and its derivatives. Figure 4.38 shows calculated variation of accelerations at different time steps. Inertial forces were calculated by multiplying the accelerations by unit mass and integrating over the slab. Gauss integration method with 2x2 integration points was used to apply numerical integration.

As explained above, force generated by the impact is expected to be equal to the summation of the inertial and support reaction forces. Force –time histories of impact tests were presented in Figure 4.39 and Figure 4.40 with the exception of BB150b, from which unreasonable data were collected from the accelerometers on drop weight. According to force- time histories, computed inertial forces start to react before drop weight impact on slab. This error was due to the application of digital filters to the derived velocities from the displacements, which created a few artificial lumps in filtered signals at the earlier time steps. However, it can be seen in Figure 4.39b and Figure 4.40b that impact responses are equilibrated after the first cycles of the forces well.

When static and impact test results were compared for the identical specimens, it is clearly seen that measured peak support reactions from static tests were approximately half of the peak support reactions measured from impact tests. To investigate this difference in capacities, a quadrant of a slab was modeled in SAP2000 using finite element method. In this linear elastic model, moment and shear force distributions were calculated at the moment of impact when the entire impact force was resisted by the inertia forces only, i.e. support reactions were zero. Calculated inertia forces at this moment were fed into the model as static forces to calculate the force

distribution at the impact case, whereas same load was applied statically at the middle to calculate the force distribution at the static case. The result from the analyses show that same total load for impact and static conditions create approximately same maximum shear forces around the impact point (see Figure 4.41a and Figure 4.41b), but maximum moments created by impact forces are approximately half of the moments created in static loading condition (Figure 4.41c and Figure 4.41d). This can explain the higher capacity observed in impact case, as combination of shear forces and moments cause failure at lower load levels in static case. In other words, slabs may resist higher shear loads due to lower moments during the impact. Detailed numerical examinations should be carried out to investigate this phenomenon further.

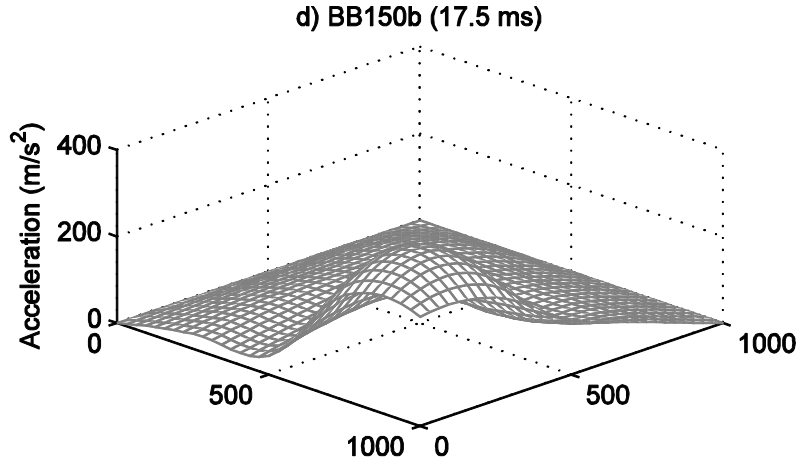
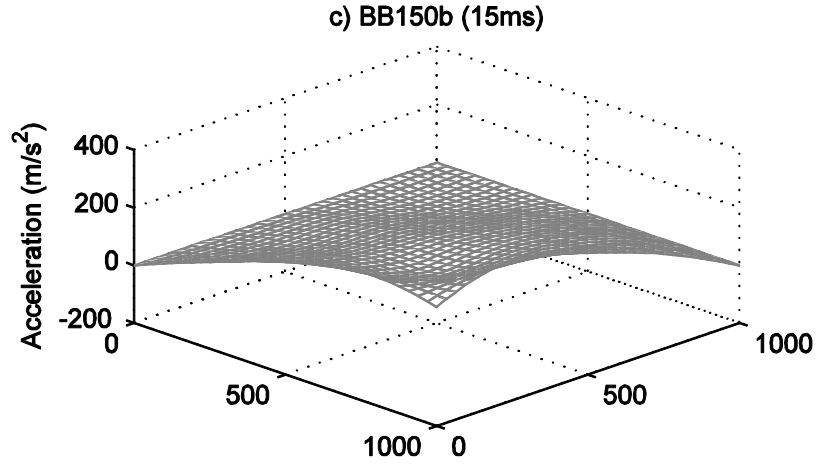
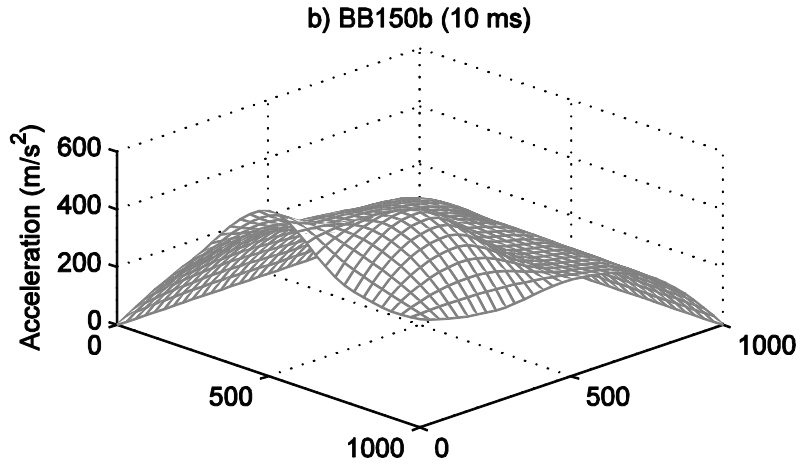
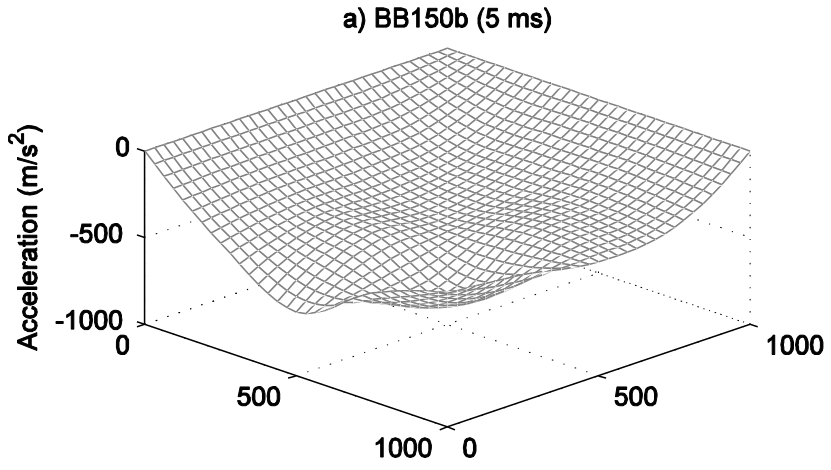


Figure 4.38. 3-D plots of derived acceleration profiles for quadrants of BB150b

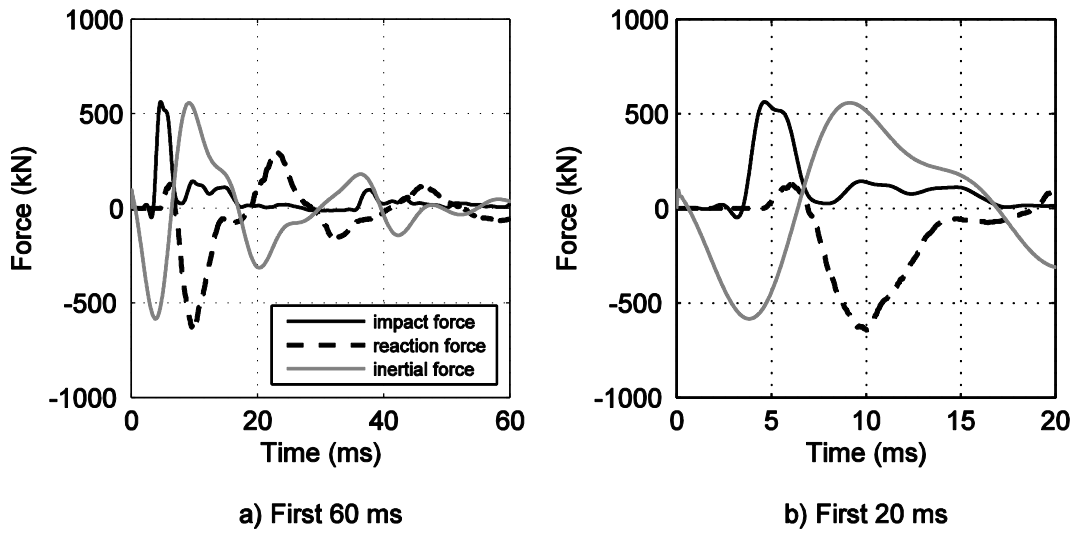


Figure 4.39. Dynamic equilibrium for BB100b-1

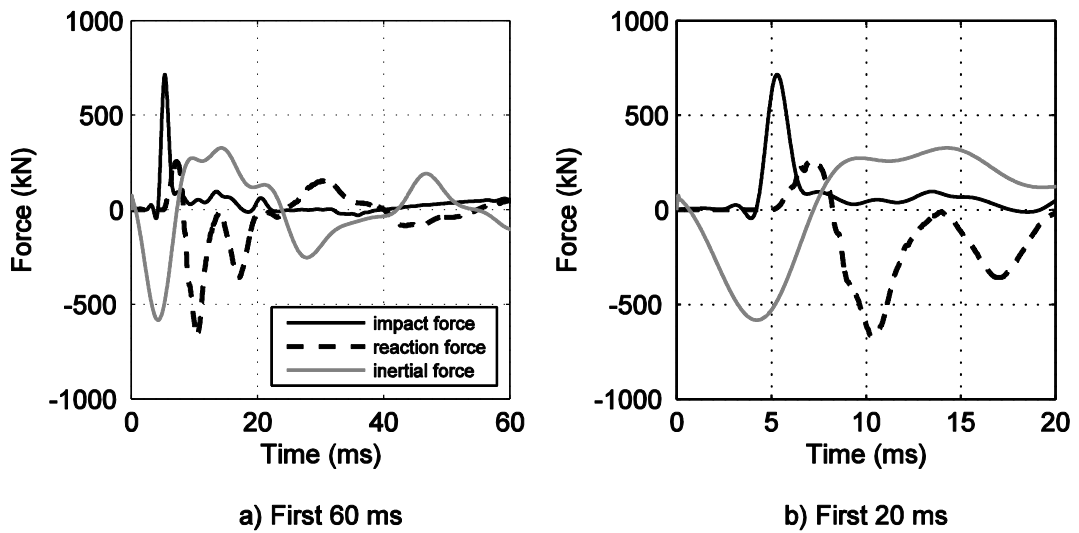
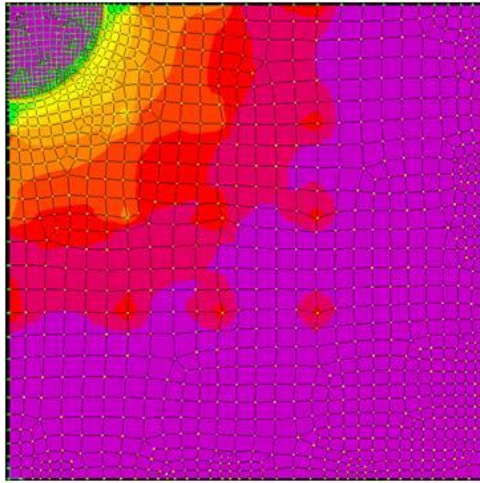




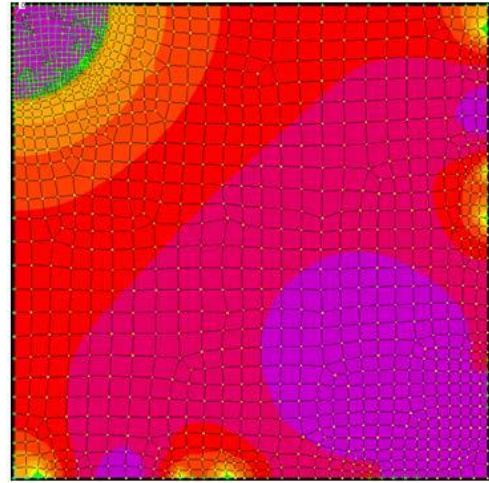






Figure 4.40. Dynamic equilibrium for BB200b-1



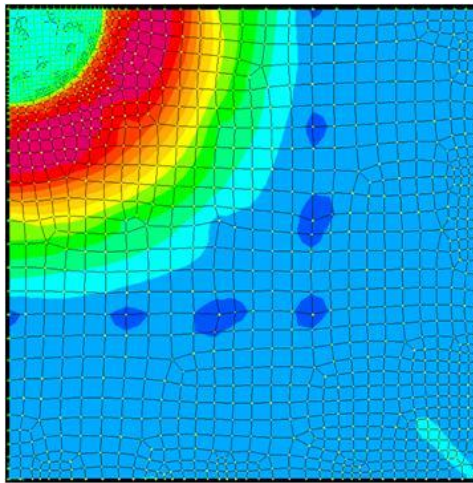
Vmax (N/mm ²)	
	40
	120
	320
	400






a) Maximum shear for impact



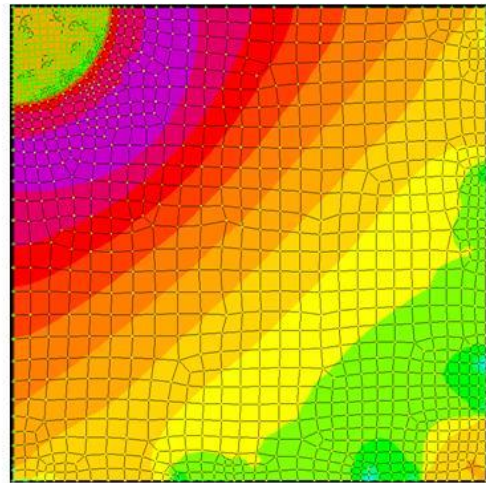
Vmax (N/mm ²)	
	60
	180
	360
	480






b) Maximum shear for static



Mmax (N.mm)	
	-24200
	-22000
	-11000
	0
	2200

c) Maximum moment for impact



Mmax (N.mm)	
	-42500
	-25500
	0
	17000
	34000

d) Maximum moments for static

Figure 4.41. Maximum moment and shear distributions for impact and static cases

CHAPTER 5

CONCLUSIONS

The study presented here is the investigation of the impact behavior of reinforced concrete slabs. In line with this purpose, six reinforced concrete slabs were tested. For better understanding, three identical pairs, varying longitudinal reinforcement ratios, were employed to facilitate comparison of the results for specimens under static and impact loads. All specimens were intensely instrumented to obtain displacements, support reactions and accelerations, and data were captured and recorded by the help of high speed data acquisition system. Observations of tests and interpretations of data for this study are summarized as follows:

- Under static loading conditions, all specimens showed flexural response with the formation of radial cracks extending from the loading point towards edges as sign of yield line theory, but failed under shear punching, creating the visible punching cone.
- Increasing amount of longitudinal reinforcement ratio influences ductility and static load capacity. The specimen with the highest amount of reinforcement ratio sustained the highest load, whereas it failed in brittle manner.
- Impact tests revealed the importance of the inertia forces. According to force-time histories of these tests, the impact forces are resisted by the inertial forces of the slabs at the initial phases. Forces developed at supports become prominent at the post-impact and equilibrium is observed at this stages. Additionally, all measured reaction forces were approximately same whereas impact forces, equal in magnitude to mass times acceleration, varies.
- When the comparison is made between forces developed at supports under impact and static loads, measured reaction forces developed under impact loading is higher than under static loading, no matter it fails or not. Additionally, direction of forces measured at supports is opposite to each other under static and impact loads.

- The displacement profiles are compatible with direction of forces under static loading, but in impact events change in force distribution on the specimen due to creation of very high accelerations which causing high inertial forces do not allow the portions of specimen to follow other portions. This lag in response can obviously be seen in comparison of displacement profiles under static and impact loads for the same midpoint deflections. As a consequence of this difference in displacement behaviors, measured support reactions are in opposite direction as well. In static cases, while supports in the middle along the edges measure compressive loads and supports at the corners measure tensile loads; this context is vice versa for impact events.
- Using the experiences gained from this study, amount of instrumentations should be increased such as accelerometers for more reliable data and data losses due to spalling of concrete may be prevented.
- For future works, this study provides the opportunity to understand behavior of RC slabs under impact loads and gives an idea for the testing parameters such as varied impact loads and velocities, and different types of concrete mixtures.

REFERENCES

- ACI Committee 318. (2011). Building Code Requirements for Structural Concrete and Commentary- ACI 318M-11, American Concrete Institute
- Bentz, E.C. (2000). Response-2000 Reinforced Concrete Sectional Analysis using the Modified Compression Field Theory, University of Toronto, Toronto, Canada
- Bhatti, A.,Q., Khatoon, S., Mehmood, A., Dastgir, A., & Kishi, N., (2011) Numerical Study for Impact Resistant Design of Full Scale Arch Type Reinforced Concrete Structures under Falling Weight Impact Test. *Journal of Vibration and Control* 18(9), 1275-1283.
- Buzzini, D., Dazio, A., & Trüb, M., (2006). Quasi-Static Cyclic Tests on Three Hybrid Fibre Concrete Structural Walls, IBK Report Nr. 297, Institute of Structural Engineering, Swiss Federal Institute of Technology Zurich, Zurich, Switzerland.
- CAN/CSA Standard A23.3-04. (2004). Design of Concrete Structures, Canadian Standards Association, Canada.
- Chen, Y., & May, I. M.,(2009). Reinforced Concrete Members under Drop-Weight Impacts. *Proceedings of Institution of Civil Engineers, Structure and Buildings* 162, 45-56
- EC2. (2004). Eurocode 2 Design of Concrete Structures, Part 1-1: General Rules and Rules for Buildings, European Committee for Standardization
- Hummeltenberg, A., Beckmann, B., Weber, T., & Curbach, M., (2011) Investigation of Concrete Slabs under Impact Load. *Applied Mechanics and Materials Vol.82*, 398-403
- Kishi, N., Kurihashi, Y., Ghadimi Khasraghy, S., & Mikami, H., (2011). Numerical Simulation of Impact Response Behavior of Rectangular Reinforced Concrete Slabs under Falling-Weight Impact Loading. *Applied Mechanics and Materials Vol.82*, 266-271
- LabView™ (2010). National Instruments, Austin, TX., U.S.A.

Marks II, R. J. (1991). *Introduction to Shannon Sampling and Interpolation Theory*, Springer-Verlag, New York.

MATLAB[®] (2009). The MathWorks, Natick, M.A., U.S.A.

Mougin, J.P., Perrotin, P., Mommessin, M., Tonnelo, J., Agbossou, A. (2005). Rock Fall Impact on Reinforced Concrete Slab: An Experimental Approach. *International Journal of Impact Engineering*, 31, 169-183

SAP2000 Structural Analysis Program. Computers and Structures, Inc., Berkeley, CA, U.S.A.

Schellenberg, K., (2009). On the Design of Rockfall Protection Galleries. Institute of Structural Engineering, Swiss Federal Institute of Technology Zurich, Zurich, Switzerland.

TS500 (2000). Requirements for Design and Construction of Reinforced Concrete Structures. Turkish Standards Institution, Ankara.

Zineddin, M., & Krauthammer, T., (2007). Dynamic Response and Behaviour of Reinforced Concrete Slabs under Impact Loading. *International Journal of Impact Engineering*, (34), 1517-1534

APPENDIX A

TECHNICAL DATA SHEETS FOR SENSORS

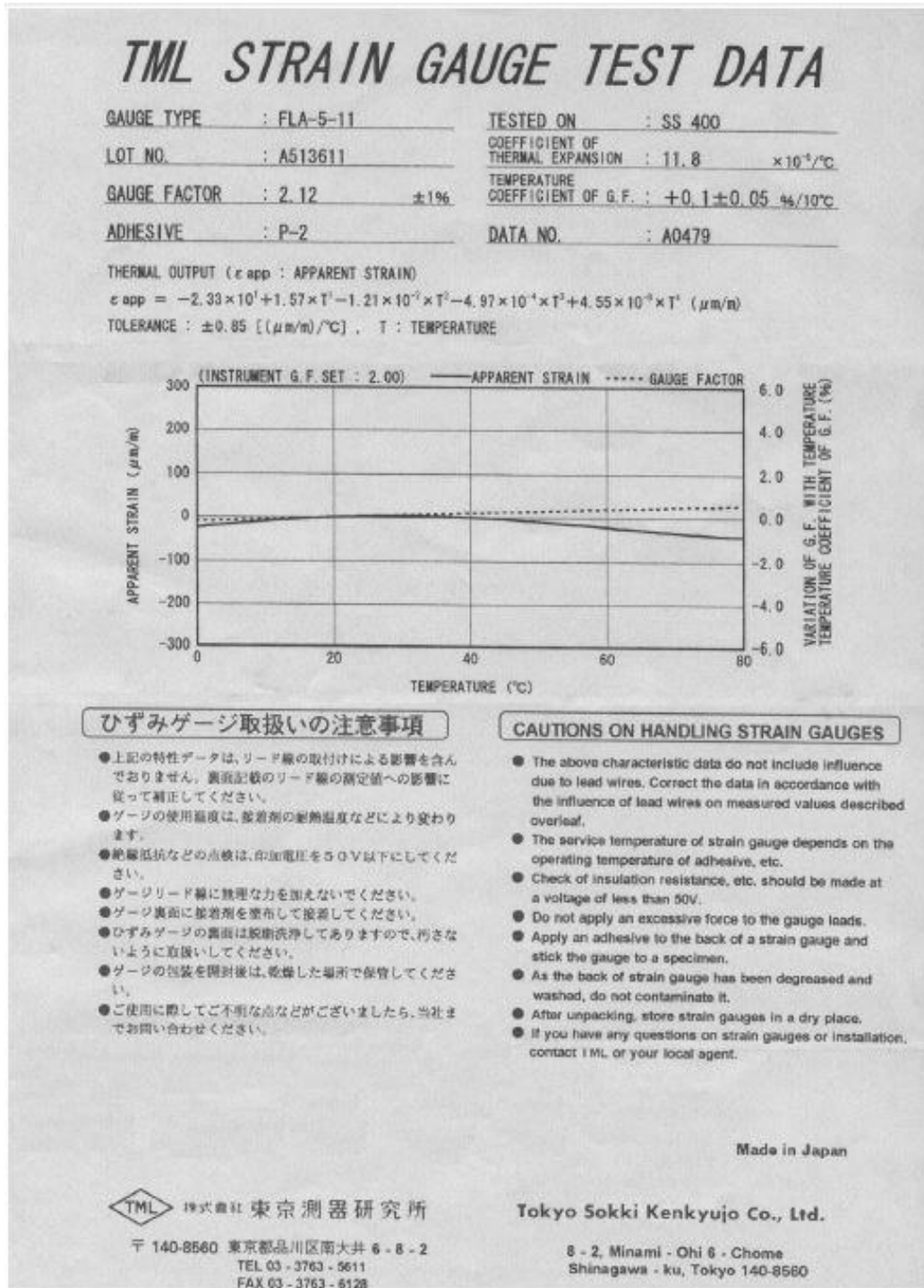


Figure A.1. Strain gauge data sheet

TML ひずみゲージの取扱い方法

基本的な接着手順

1. **接着剤の選択** 使用する条件に合った、ひずみゲージ用の接着剤を選びます。
2. **表面処理** 被接着面のさび・塗料などを除去し、120～180番(アルミ:240～320番)のサンドペーパーで軽く磨きアセトンなどで洗浄して、ゲージ接着位置をけがいでください。
3. **ゲージ接着** 接着剤の取扱説明書を参照してください。
4. **キュアリング** 接着剤の取扱説明書を参照してください。
5. **点検** ひずみゲージのゲージ抵抗値・絶縁抵抗値の点検を行ってください。
6. **結線** リード線はゲージ端子を使用して、はんだ付けで接続してください。
・必要に応じて防水処理を施してください。

リード線の測定値への影響

- リード線の温度変化による影響。
(3線式結線法では、温度影響はありません。)

$$\epsilon l = \frac{r \cdot L \cdot \alpha \cdot \Delta T}{K(R + r \cdot L)} \quad \text{<式1>}$$

ϵl = リード線の熱出力
 r = リード線 1m 当たりの往復の抵抗値 (Ω/m)
 L = リード線の長さ (m)
 α = リード線の抵抗温度係数
 (銅線 = $3.9 \times 10^{-3} / ^\circ C$)

ΔT = 温度変化量
 K = ゲージ率
 R = ゲージ抵抗

- リード線の結線によるゲージ率の補正。

・2線式の場合

$$K_0 = \frac{R}{R + r \cdot L} \cdot K \quad \text{<式2>}$$

・3線式の場合

$$K_0 = \frac{R}{R + \frac{r \cdot L}{2}} \cdot K \quad \text{<式3>}$$

K_0 = 補正したゲージ率

HANDLING METHOD OF TML STRAIN GAUGES

Basic Bonding Procedures

1. **Select adhesive**
Select an adhesive most suitable for test conditions.
2. **Surface treatment**
Remove grease, rust, paint, etc. from the bonding surface of a specimen, lightly polish with an abrasive paper of #120 ~ 180 (#240 ~ 320 for aluminium), wipe with acetone, etc. and mark gauge installation position.
3. **Gauge installation**
Refer to the operation manual of adhesive.
4. **Adhesive curing**
Refer to the operation manual of adhesive.
5. **Gauge installation check**
Check gauge resistance and insulation resistance.
6. **Lead wire attachment**
Solder lead wires to the strain gauges through connecting terminals.
・ If necessary, apply waterproof coating.

Influence of Lead Wires on Measured Values

- Influence of temperature variation of lead wires
(3-wire system is independent of temperature.)

$$\epsilon l = \frac{r \cdot L \cdot \alpha \cdot \Delta T}{K(R + r \cdot L)} \quad \text{<Equation 1>}$$

where ϵl = thermal output of lead wires
 r = total resistance per meter of lead wires (Ω/m)
 L = length of lead wires (m)
 α = temperature coefficient of resistance of lead wires
 (copper wire = $3.9 \times 10^{-3} / ^\circ C$)
 ΔT = temperature variation
 K = gauge factor
 R = gauge resistance

- Gauge Factor Correction due to Lead Wire Attachment

・ In case of 2-wire system

$$K_0 = \frac{R}{R + r \cdot L} \cdot K \quad \text{<Equation 2>}$$

・ In case of 3-wire system

$$K_0 = \frac{R}{R + \frac{r \cdot L}{2}} \cdot K \quad \text{<Equation 3>}$$

where K_0 = corrected gauge factor

リード線 1m 当たりの往復の抵抗値 Total Resistance per Meter of Lead Wires

構成 (心数/直径) Lead wires (number of cores / diameter)	ポリイミド線 polyimide	ポリイミド線 polyimide	7/0.12	10/0.12	12/0.18	20/0.18
リード線の直径または断面積 Diameter or cross sectional area of lead wires	φ 0.14mm	φ 0.18mm	0.08 mm ²	0.11 mm ²	0.3 mm ²	0.5 mm ²
1m 当たりの往復の抵抗値 Total resistance per meter	2.5 Ω/m	1.5 Ω/m	0.44 Ω/m	0.32 Ω/m	0.12 Ω/m	0.07 Ω/m

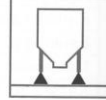
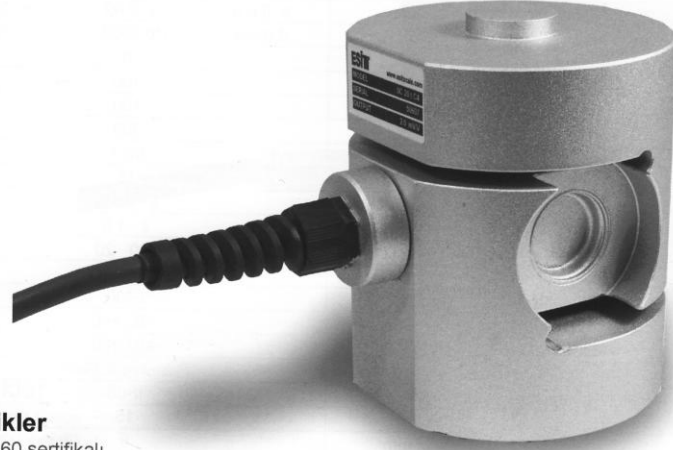
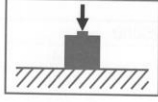
Figure A.2. Strain gauge data sheet

Model SC

10000kg-20000kg

Baskı Tipi Yük Hücresi

Çelik



Özellikler

- OIML R60 sertifikalı
- Kaynakla kapalı gövde
- Yan yüklerle dayanıklı
- Ağır hizmete dayanıklı
- IP68 endüstriyel koruma



SC yük hücreleri, kesme kuvveti prensibi ile baskıya çalışan yüksek kapasiteli elektronik ağırlık ve kuvvet ölçme uygulamalarında endüstriyel ortamlarda kullanılmak üzere geliştirilmiştir. Kusursuz ve sağlam yapısı ile yan yüklerle ve aşırı yüklerle karşı yüksek dayanıklılık gösterir.

Alaşım çeliğinden gövdesi korozyona uzun süreler dayanabilen özel boya ile kaplanmış, ölçüm bölgesi ise paslanmaz çelik kapakla kaynaklı olarak kapatılmış olan SC yük hücreleri IP68 sınıfında suya karşı tam korumalıdır. SC yük hücreleri, ağır endüstri koşullarına uygundur. Yüksek kapasitelerdeki taşıt kantarları, platform kantarları, tank tartı sistemleri, otomatik tartı aletleri ve proses ölçümlerinde kullanılır.

Model	Kapasite	Minimum taksimat	Aşırı yükleme kapasitesi
SC 10	10,000 kg	1.200 g	15,000 kg
SC 20	20,000 kg	2.400 g	30,000 kg

SC Montaj Kitleri

- SC-EL Kauçuk montaj kiti | sayfa 76
- SC-TM Tank montaj kiti | sayfa 77
- SC-ELT Kauçuk Tank montaj kiti | sayfa 78

Figure A.3. Model SC load cell technical sheet

Model SC



Teknik Özellikler

Maksimum kapasite (E_{max})	kg	10000, 20000
Hassasiyet sınıfı (OIML R 60 standartlarına göre)		C1 C3 C4
Maksimum bölüntü sayısı ($n_{l,c}$)		1000 3000 4000
Minimum ölçüm aralığı (V_{min})		$E_{max}/3500$ $E_{max}/5000$ $E_{max}/8500$
Toplam hata	%	≤ 0.05 ≤ 0.02 ≤ 0.015
Sıfıra dönüş hatası (DR)	$\%E_{max}$	0.0025
Minimum yük	$\%E_{max}$	0
Aşırı yükleme kapasitesi	$\%E_{max}$	150
Aşırı yan yükleme kapasitesi	$\%E_{max}$	100
Kırılma kapasitesi	$\%E_{max}$	300
Esneğe (E_{max} yükte)	mm	≤ 0.3
Maksimum uyarı gerilimi (U_{max})	V	15
Kazanç (C_n)	mV/V	2 0.1%
Yüksüz çıkış	$\%C_n$	≤ 1.0
Giriş direnci	Ω	385 20
Çıkış direnci	Ω	350 3
İzolasyon direnci	M Ω	≥ 500
Düzeltilmiş çalışma sıcaklığı aralığı	$^{\circ}C$	-10...+40
Çalışma sıcaklığı aralığı	$^{\circ}C$	-40...+80
Yük Hücresi malzemesi		Çelik
Koruma sınıfı (EN60529 standartlarına göre)		IP68
Kablo boyu	m	13
Kablo dış çapı	mm	8
Ağırlık	kg	10
Paket ebatları / ağırlığı	cm / kg	25x25x18 / 10.3

Ölçüler

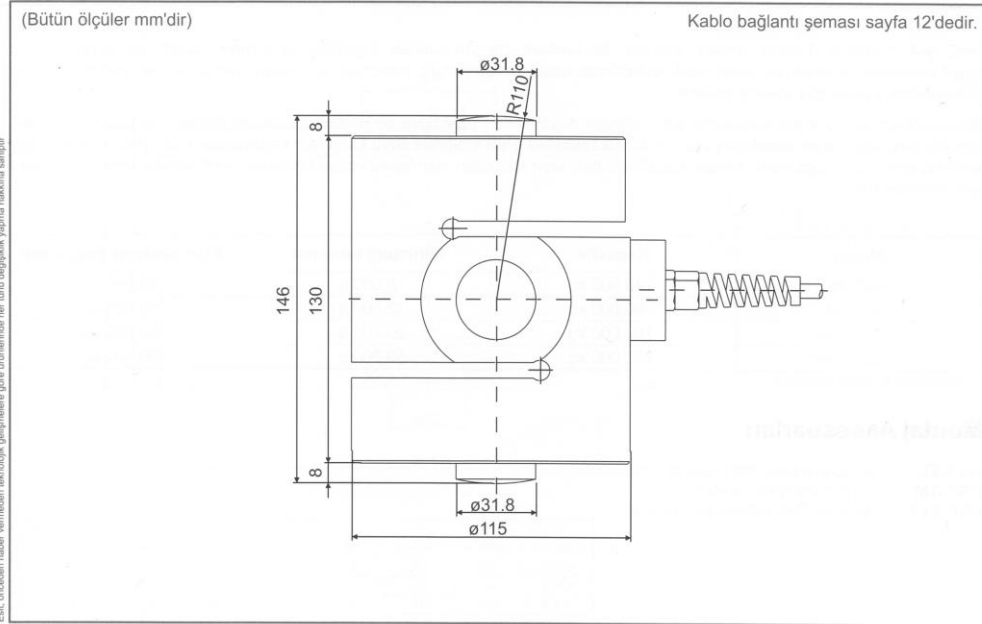


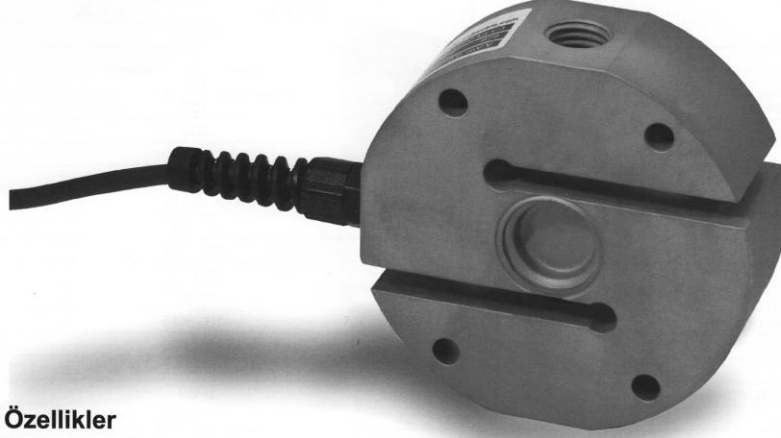
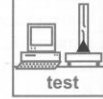
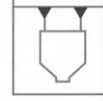
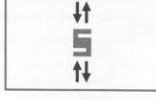
Figure A.4. Model SC load cell technical sheet

Model TB

500kg-1000kg-2000kg-5000kg

S Tipi Yük Hücresi

Paslanmaz Çelik



Özellikler

- Paslanmaz çelik
- Kolay montaj
- Kaynakla kapalı gövde
- OIML R60 normlarına uygun
- IP68 endüstriyel koruma

TB yük hücreleri, kesme kuvveti prensibi ile çalışan elektronik ağırlık ve kuvvet ölçme uygulamalarında kullanılmak üzere geliştirilmiştir. Çekiye çalışan ağırlık ve kuvvet ölçme uygulamaları için geliştirilmiş olup baskıya da çalışan sistemlere uyarlanabilir.

TB hücreleri; orta kapasiteli tank tartı, tumba kantarları, elektromekanik kantarlar, çekme-kopmaRM test cihazları, proses yük uygulamaları ve benzeri sistemlerde kullanılır. Alaşım çeliğinden gövdesi korozyona uzun süreler dayanabilen özel boya ile kaplanmış, ölçüm bölgesi ise paslanmaz çelik kapakla kaynaklı olarak kapatılmış olan TB yük hücreleri IP68 sınıfında suya karşı tam korumalıdır.

Model	Kapasite	Minimum taksimat	Aşırı yükleme kapasitesi
TB 500	500 kg	100 g	750 kg
TB 1000	1,000 kg	200 g	1,500 kg
TB 2000	2,000 kg	400 g	3,000 kg
TB 5000	5,000 kg	1,000 g	7,500 kg

TB Montaj Kitleri

TB-HA Mafsallı montaj kiti | sayfa 75

Figure A.5. Model TB load cell technical sheet

Model TB

ESİTİM

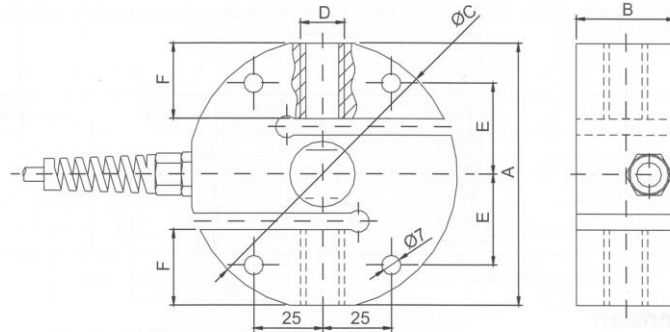
Teknik Özellikler

Maksimum kapasite (E_{max})	kg	500, 1000, 2000, 5000
Hassasiyet sınıfı (OIML R 60 standartlarına göre)		C1 C3
Maksimum bölüntü sayısı (n_{LC})		1000 3000
Minimum ölçüm aralığı (V_{min})		$E_{max}/5000$ $E_{max}/5000$
Toplam hata	%	≤ 0.03 ≤ 0.02
Sıfıra dönüş hatası (DR)	$\%E_{max}$	0.01
Minimum yük	$\%E_{max}$	0
Aşırı yükleme kapasitesi	$\%E_{max}$	150
Aşırı yan yükleme kapasitesi	$\%E_{max}$	100
Kırılma kapasitesi	$\%E_{max}$	200
Esneme (E_{max} yükte)	mm	≤ 0.4
Maksimum uyarım gerilimi (U_{max})	V	15
Kazanç (C_n)	mV/V	2 0.1%
Yüksüz çıkış	$\%C_n$	≤ 1.0
Giriş direnci	Ω	385 20
Çıkış direnci	Ω	350 3
İzolasyon direnci	M Ω	≥ 500
Düzeltilmiş çalışma sıcaklığı aralığı	$^{\circ}C$	-10...+40
Çalışma sıcaklığı aralığı	$^{\circ}C$	-40...+80
Yük Hücresi malzemesi		Çelik
Koruma sınıfı (EN60529 standartlarına göre)		IP68
Kablo boyu	m	5
Kablo dış çapı	mm	5
Ağırlık	kg	1.9 - 2.8
Paket ebatları / ağırlığı	cm / kg	11x34x9 / 1 - 3

Ölçüler

(Bütün ölçüler mm'dir)

Kablo bağlantı şeması sayfa 12'dedir.



Kapasite (kg)	A	B	C	D	E	F
500	95	36	Ø98	M16	33	28
1000	95	36	Ø98	M16	33	28
2000	95	36	Ø98	M16	33	28
5000	112	40	Ø115	M24x2	40	32

ESİTİM

Yük Hücreleri Ürün Kataloğu 2010

Sayfa 27

Figure A.6. Model TB load cell technical sheet

Resistive Linear Position Transducer



- Output 4-20 mA or 0-20 mA or 0-10 V
- Internal electronic circuit
- Stable output signal against supply voltage variations
- Best solution for automation systems

Main Applications

Metal Forming Machineries, Textile Machineries, Packing Machineries
Marble/ Stone Machineries, Printing Machineries and General Automation Applications

Specifications

Measuring Stroke	50mm to 600mm
Output	4-20 mA or 0-20 mA or 0-10 V
Linearity	± %0,05
Resolution	Infinite
Load resistance	Min. 10 Kohm
Repeatability	≤ %0,01
Mechanical life	100 * 10 ⁶ Cycles
Displacement speed	≤ 5 m/s
Permissible applied voltage	13-30 VDC
Electrical connections	4 Pole connector
Case dimensions	Ø 38mm
Case material	Anodized aluminium
Rod diameter	10mm
Rod material	Stainless steel
IP Degree	IP 65
Working temperature	- 20 / + 80 °C
Mechanical fixing	2 Ball joints

Dimensions

Model	LM	Mechanical stroke (MS)	Electrical measuring stroke (EMS)	Total lengt (L)
ELPC	50	52mm	50mm	272mm
ELPC	75	77mm	75mm	297mm
ELPC	100	102mm	100mm	322mm
ELPC	125	127mm	125mm	347mm
ELPC	130	132mm	130mm	352mm
ELPC	150	152mm	150mm	372mm
ELPC	175	177mm	175mm	397mm
ELPC	200	202mm	200mm	422mm
ELPC	225	227mm	225mm	447mm
ELPC	250	252mm	250mm	472mm
ELPC	275	277mm	275mm	497mm
ELPC	300	302mm	300mm	522mm
ELPC	325	327mm	325mm	547mm
ELPC	350	352mm	350mm	572mm
ELPC	375	377mm	375mm	597mm
ELPC	400	402mm	400mm	622mm
ELPC	450	452mm	450mm	672mm
ELPC	500	502mm	500mm	722mm
ELPC	550	552mm	550mm	772mm
ELPC	600	602mm	600mm	822mm

Ordering Procedure

ELPC	200	D	I4
<i>Model</i>	<i>Measurement Stroke</i>	<i>Linearity Class</i> D: 0,05 %	<i>Output: Voltage or Current</i> V10: 0-10V I4: 4-20mA I20: 0-20mA

Figure A.7. RLPTs' technical sheet

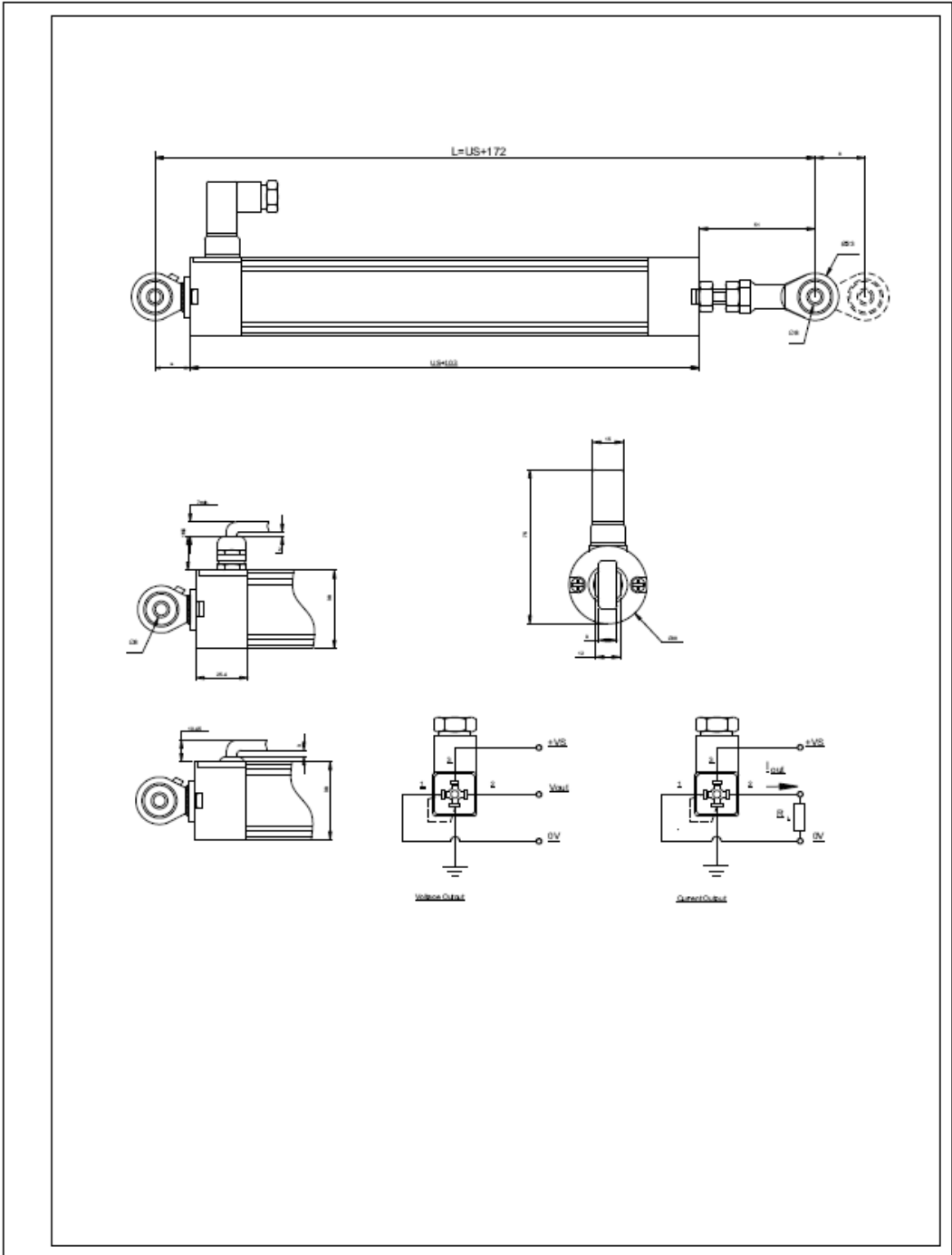


Figure A.8. RLPTs' technical sheet

Acceleration

KISTLER
measure. analyze. innovate.

K-Shear® Accelerometer

Type 8742A...

High Resonant Frequency, Shock Accelerometer, Optional Ground Isolation

Quartz shock accelerometer for measuring short duration impulse and impact shocks. Type 8742A... shock accelerometers have a rugged welded construction, integral stud and are available in four measuring ranges.

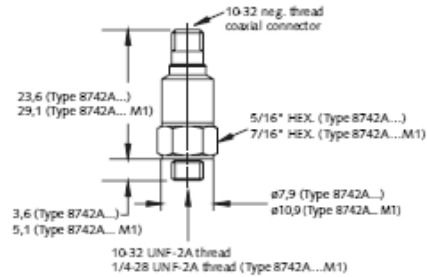
- Low impedance, voltage mode
- Unique quartz shear sensing element
- Ranges 5 000 g to 50 000 g
- Optional ground isolation
- Low transverse sensitivity
- Rugged connector for repeated connections
- Wide bandwidth, high resonant frequency
- Conforming to CE

Description

The sensing element contained within this shock accelerometer series features a unique, shear mode four quartz crystal configuration combined with an annular preload sleeve and seismic mass. The element design provides over 100 kHz resonance frequency ensuring accurate measurement of high speed events with zero shift and internal amplifier saturation virtually eliminated. These shock sensors exhibit insensitivity to thermal transients, and have extremely low transverse and base strain sensitivity. Using quartz as the sensing material adds another performance benefit in that quartz will not depolarize if exposed to high shock. The ground isolated option uses a patented technique that ensures high resonant frequency while providing electrical isolation.

Poor connector pin continuity resulting from an applied shock can momentarily interrupt a measured event. To ensure reliable shock measurements, Type 8742A... accelerometer contains an improved spring insert made of a gold plated Beryllium-Copper. Beryllium Copper provides the elastic physical properties that promote positive contact and resists aging.

An internal microelectronic Piezotron® signal conditioning circuit



converts the charge developed in the quartz element as a result of the accelerometer being subjected to shock, into a useable high level voltage output signal at a low impedance level. The low impedance output provides high immunity to noise and insensitivity to cable motion.

Application

Type 8742A... accelerometer is ideally suited for impact and impulse shock measurements where metal-to-metal impact occurs; where package and product survivability drop shock tests are of interest and where vehicle crash data is collected.

Mounting

The case isolated Type 8742A... is attached to the test structure by its integral 1/4-28 UNF stud and the non isolated Type 8742 version, uses an integral 10-32 UNF stud. Reliable and accurate measurements require that the mounting surface be clean and flat. The instruction manual for the shock accelerometer series provides detailed information regarding mounting surface preparation.

Technical Data

Specification	Unit	Type 8742A5	Type 8742A10	Type 8742A20	Type 8742A50
Acceleration range	g	±5 000	±10 000	±20 000	±50 000
Acceleration limit	gpk	±6 000	±12 000	±24 000	±60 000
Threshold (noise ≤130 μV _{out}), nom.	grms	0,13	0,25	0,5	1,3
Sensitivity, ±5 %	mV/g	1	0,5	0,25	0,1
Resonant frequency mounted, nom.	kHz	100	100	100	100
Frequency response, ±7 % (M1: ±10 %)	Hz	1 ... 10 000	1 ... 10 000	1 ... 10 000	1 ... 10 000
Amplitude non-linearity	%FSO	±1	±1	±1	±1
Time constant, nom.	s	≥0,5	≥0,5	≥0,5	≥0,5
Transverse sensitivity, nom. (max. 5)	%	1,5	1,5	1,5	1,5

Page 1/2

This information corresponds to the current state of knowledge. Kistler reserves the right to make technical changes. Liability for consequential damage resulting from the use of Kistler products is excluded.

©2008, Kistler Group, Eulachstrasse 22, 8408 Winterthur, Switzerland
Tel. +41 52 224 11 11, Fax +41 52 224 14 14, info@kistler.com, www.kistler.com

Figure A.9. Accelerometers' technical sheet

Environmental	Unit	Type 8742A5	Type 8742A10	Type 8742A20	Type 8742A50
Base strain sensitivity @ 250 µε	g/µε	0,005	0,005	0,005	0,005
Shock limit	gpk	50 000	50 000	50 000	100 000
Temperature coeff. of sensitivity	%/°C	-0,06	-0,06	-0,06	-0,06
Operating Temperature range	°C	-55 ... 120	-55 ... 120	-55 ... 120	-55 ... 120

Output	Unit	Type 8742A5	Type 8742A10	Type 8742A20	Type 8742A50
Bias, nom.	VDC	11	11	11	11
Impedance	Ω	<100	<100	<100	<100
Voltage full scale	V	±5	±5	±5	±5

Source	Unit	Type 8742A5	Type 8742A10	Type 8742A20	Type 8742A50
Voltage	VDC	18 ... 30	18 ... 30	18 ... 30	18 ... 30
Constant current	mA	2 ... 20	2 ... 20	2 ... 20	2 ... 20

Construction	Unit	Type 8742A5	Type 8742A10	Type 8742A20	Type 8742A50
Sensing element	Type	quartz-shear	quartz-shear	quartz-shear	quartz-shear
Housing/Base	material	Titan./St. Stl.	Titan./St. Stl.	Titan./St. Stl.	Titan./St. Stl.
Sealing Housing/Connector (EN 60529)		IP68	IP68	IP68	IP68
Connector	Type	10-32 neg.	10-32 neg.	10-32 neg.	10-32 neg.
Ground isolation		with pad	with pad	with pad	with pad
Type 8742A...M1		yes	yes	yes	yes
Mass	grams	4,5	4,5	4,5	4,5
Type 8742A...M1	grams	8,2	8,2	8,2	8,2
Mounting (10-32 x 3,6)	Type	stud	stud	stud	stud
Type 8742A...M1 (1/4-28 x 5,1)					
Mounting torque	N-m	2	2	2	2
Type 8742A...M1	N-m	3,4	3,4	3,4	3,4

1 g = 9,80665 m/s², 1 Inch = 25,4 mm, 1 gram = 0,03527 oz, 1 lbf-in = 0,1129 N-m

Measuring Chain

- 1 Low impedance sensor
- 2 Sensor cable, 10-32 pos. to BNC pos.
- 3 Power supply/signal conditioner
- 4 Output cable BNC pos. to BNC pos.



Type

- 8742A...
- 1761B...
- 51...
- 1511

Ordering Key

Range	
±5 000 g	5
±10 000 g	10
±20 000 g	20
±50 000 g	50

Variants

Standard	-
Ground isolated	M1

8742A □ □



Figure A.10. Accelerometers' technical sheet